Ab initio modelling of adiabatic polaron dynamics in transition metal oxides

Zi Wang
Materials Engineering
Department of Mining and Materials Engineering
McGill University
Montréal, Québec
Canada

A Thesis submitted to the
Faculty of Graduate Studies and Research
in partial fulfillment of the requirements for the degree of
Doctor of Philosophy

Contents

List of Figures

List of Tables

Abstract

Many novel materials considered for applications in renewable energy technologies are transition metal (TM) oxides and are known to exhibit polaronic behaviour. In many such TM oxides, the strong on-site correlation effects localize the *d* shell electrons and open an energy gap in the material, effecting a transition to semiconducting behaviour. Furthermore, the localization of *d* shell electrons to atomic-like orbitals leads to electrostatic interactions that distort the surrounding lattice, resulting in a self-trapped state which we call a polaron. In many cases, the self-trapped nature of polarons can dramatically lower the conductivity of the material. As TM oxides are found in many applications including lithium ion battery cathodes, photovoltaic materials, and catalysts, a low conductivity can have large impacts on their efficiencies as renewable energy materials. On the other hand, beneficial cases also exist where polarons can contribute to device functionality, for instance by creating a strong TM redox potential which increases operating voltage, or by providing a conduction pathway when the band gap is too wide for regular conduction to occur. It is therefore essential, in all of these cases, to study polaronic behaviour in such materials in order to accurately predict and engineer their properties.

In this thesis, I have conducted a comprehensive first principles study of polaronic behaviour in TM oxides through a combination of density functional theory (DFT) with a theoretical polaron hopping model. The selection of relevant TM oxides that I have investigated includes battery cathode materials ($LiMn_2O_4$ and $LiFePO_4$), photovoltaic materials (TiO_2 and Fe_2O_3), catalytic materials ($MgFe_2O_4$ and $LaCrO_3$), and other materials of importance ($LaMnO_3$ and $KCuF_3$). I use DFT to calculate the polaronic states and optimize the structures in these materials, and then use my hopping model to analyse the results in greater detail.

By considering the variety of different material compositions and crystal structures of TM oxides that exhibit polaronic behaviour, I have developed a set of guidelines that can qualitatively predict the polaronic properties in a TM oxide based on just the crystal structure and chemical composition of the material. My calculations on $LiMn_2O_4$, $LiFePO_4$, TiO_2, and Fe_2O_3 are more detailed in nature, and the results for TiO_2 and Fe_2O_3 in particular agree well with experimentally measured values. I have

included the other materials for their different structural properties, and the focus here was on finding qualitative trends for all the studied materials.

From a computational materials design perspective, my work provides several insights that will allow for more consistent predictions of polaronic properties in transition metal oxides. I have improved upon the quantitative calculations of polaron properties within existing ab initio methods, and I have achieved a better qualitative understanding of polaron dynamics from basic structural principles.

Résumé

Beaucoup de nouveaux matériaux considérés pour les applications dans les technologies d'énergie renouvelable sont des oxydes de métaux de transition (MT) et sont connus pour présenter un comportement polaronique. Dans de nombreux oxydes de MT, les forts effets de corrélation sur chaque site localisent les électrons de couche d et créent une bande interdite dans le matériau, ce qui entraîne une transition vers un comportement semiconducteur. En outre, la localisation des électrons de couche d en orbitales atomiques conduit à des interactions électrostatiques qui déforment le réseau environnant, ce qui entraîne un état auto-piégé que nous appelons un polaron. Dans de nombreux cas, la nature auto-piégée des polarons réduit considérablement la conductivité du matériau. Comme les oxydes de MT sont utilisés dans de nombreuses applications, y compris les cathodes de batteries au lithium-ion, les matériaux photovoltaïques et les catalyseurs, une faible conductivité peut avoir un grand impact sur leur efficacité en tant que matériaux d'énergie renouvelable. Par contre, il y a aussi des cas bénéfiques dans lesquels les polarons peuvent contribuer à la fonctionnalité du dispositif, par exemple la création d'un fort potentiel d'oxydo-réduction de MT pour augmenter la tension de fonctionnement, ou l'ouverture d'une voie de conduction lorsque la bande interdite est trop large pour avoir lieu la conduction régulière. Dans tous les cas, il est donc essentiel d'étudier le comportement polaronique de tels matériaux afin de prédire et de modifier leurs propriétés avec précision.

Dans cette thèse, j'ai mené une étude exhaustive des premiers principes du comportement polaronique dans les oxydes de MT en utilisant une combinaison de la théorie fonctionnelle de la densité (DFT) et d'un modèle théorique de sauts tunnel des polarons. La sélection d'oxydes de MT pertinents que j'ai étudiés comprend les matériaux de cathode de batterie ($LiMn_2O_4$ et $LiFePO_4$), les matériaux photovoltaïques (TiO_2 et Fe_2O_3), les matériaux catalytiques ($MgFe_2O_4$ et $LaCrO_3$), et d'autres matériaux d'importance ($LaMnO_3$ et $KCuF_3$). J'utilise la DFT pour calculer les états polaroniques et optimiser la structure de ces matériaux, et j'utilise ensuite mon modèle de sauts tunnel pour analyser les résultats plus en détail.

En considérant la variété des différentes compositions de matériaux et des structures cristallines des oxydes de MT qui présentent un comportement polaronique, j'ai

développé un ensemble de lignes directrices qui permettent de prédire qualitativement les propriétés polaroniques dans un oxyde de MT basé uniquement sur la structure cristalline et la composition chimique du matériau. Mes calculs sur $LiMn_2O_4$, $LiFePO_4$, TiO_2 et Fe_2O_3 sont les plus détaillés, et les résultats pour TiO_2 et Fe_2O_3 en particulier correspondent bien aux valeurs mesurées expérimentalement. J'ai inclus les autres matériaux pour leurs différentes propriétés structurelles, et l'accent a été mis sur la découverte de tendances qualitatives pour tous les matériaux étudiés.

Du point de vue de la conception numérique des matériaux, mon travail fournit plusieurs idées qui permettront des prédictions plus cohérentes des propriétés polaroniques dans les oxydes de métaux de transition. J'ai amélioré les calculs quantitatifs des propriétés polaroniques dans les méthodes ab initio existantes, et j'ai obtenu une meilleure compréhension qualitative de la dynamique des polarons à partir de principes structurels de base.

Statement of Originality

In this thesis I report a comprehensive study on polaron properties in a wide variety of transition metal (TM) oxides. The theoretical framework is based on existing theory, combining density functional theory (DFT) with an existing two-site hopping model which has been adapted to the situation of polarons in TM oxides. I have applied and adapted these models and techniques to the situation of polarons in TM oxides, improved existing relaxation techniques specific to polarons, and I have investigated the particular effect of DFT+U projection on these polaronic properties. My original contributions to this work include:

Chapter 3 Investigation of DFT+U projection and semicore electron effects on polaronic properties.

Chapter 4 Application of the NEB method to polaronic transition states (TS). NEB is widely used to calculate ionic pathways and barriers, but is not systematically applied to calculating polaronic TS. Using NEB, we typically improve the barriers by 20 - 100 meV compared to calculations done using unrelaxed linearly interpolated structures.

Chapter 4 Application of ab inito molecular dynamics (AIMD) to studying polaron hopping in $FePO_4$. While molecular dynamics is another widely used tool to study dynamics, here I use it explicitly to quantitatively analyse temperature-dependent polaron hopping.

Chapter 5 Combining elements of exchange theory and crystal symmetry to predict general trends in polaronic properties in spinel and perovskite structures, and comparing the predicted trends with calculated properties in these structures.

The work in Chapter 3 was done in collaboration with Casey Brock and Amina Matt, and is published in a peer-reviewed journal [1]. Casey Brock has performed all supporting Abinit calculations, and Amina Matt has performed the initial relaxation work in Fe_2O_3. I have performed all other work in this thesis. The work in Chapter 4 is also published in a peer-reviewed journal [2]. Chapter 5 is currently under preparation as a manuscript for submission to a peer-reviewed journal.

Acknowledgements

I would like to express my deepest gratitude to my supervisor, Prof. Kirk H. Bevan, for your exceptional supervision, patience, and kindness throughout the course of my PhD career at McGill University. I have greatly enjoyed working with you for the past five years, and our weekly discussions have been of tremendous benefit to my skills as a researcher. I have come to realize how much I have grown as an academic over the past five years, something that would not have happened without your supervision.

I would also like to express my gratitude to Vladimir Timoshevskii for sharing your deep insights on solid state theory and DFT+U theory in the early stages of my studies. Without our discussions, I would not have come up with ideas crucial to this work.

I express my thanks to our group members for insightful discussions, pleasant personal interactions, and having the patience to listen to my presentations at the group meetings. Thank you, Sazzad, Asif, Julien, Salvador, Shuaishuai, Botong, and Yee Wei! I would also like to thank my excellent summer students and colleagues Amina and Casey for our pleasant collaborations.

Mauro, Stephan, Gary, Wilfred, bedankt voor alle herinneringen, in Amsterdam maar vooral ook na mijn vertrek uit Amsterdam tot op heden aan toe. Het feit dat wanneer ik terug op bezoek ben (of jullie mij komen opzoeken) en we kunnen chillen en de draad weer oppakken alsof er geen tijd voorbij is gegaan waardeer ik enorm en ik ben jullie hier meer dan dankbaar voor.

谢谢我家，舅舅，爷爷，婆婆，谢谢你们对我的支持！

最后，最感谢我妈，对我无限耐心，风雨同舟，永远支持我所有的事业。最钦佩的一直以来都是妈妈。

I acknowledge financial support from Mitacs, Hydro-Québec, NSERC, and FQRNT, and computational support from Compute Canada and Calcul Québec.

Physical Constants and Units

1 Å = 10^{-10} m
a_0 (Bohr radius) = 0.5292 Å
m_e (electron mass) = 9.1096×10^{-31} kg
m_p (proton mass) = 1.6726×10^{-27} kg
e (electron charge) = 1.6×10^{-19} C
h (Planck's constant) = 6.626×10^{-34} J s
k_B (Boltzmann's constant) = 1.38×10^{-23} K
k_BT (at 1 K) = 8.616×10^{-5} eV
c (speed of light) = 2.9979×10^{8} m/s
G_0 (quantum unit of conductance) = $7.75 \times 10^{-5}\Omega^{-1} = \frac{1}{12.9\text{k}\Omega}$

Atomic units are used throughout this thesis unless otherwise indicated. In this system of units, $e = m_e = \hbar = 1$.

1 unit of Length = a_0 = 0.5292 Å
1 unit of Mass = m_e = 9.1096×10^{-31} kg
1 unit of Charge = e = 1.6×10^{-19} C
1 unit of Angular momentum = $\hbar$ = 1.0546×10^{-34} J s
1 unit of Energy = 1 Hartree = 27.2 eV
1 unit of Time = $\frac{\hbar}{1\text{ Hartree}}$ = 2.4189×10^{-17} s

List of Abbreviations

SE	Schrödinger's Equation
TISE	Time Independent Schrödinger's Equation
DFT	Density Functional Theory
DFT+U	Density Functional Theory with Hubbard U-corrections
BO	Born-Oppenheimer
LDA	Local Density Approximation
GGA	Generalized Gradient Approximation
TM	Transition Metal
DOS	Density Of States
NEB	Nudged Elastic Band
MD	Molecular Dynamics
POL	Polaron Ground State
TS	Polaron Transition State
JT	Jahn-Teller
PAW	Projector Augmented Wave
MH	Mott-Hubbard
CT	Charge Transfer

1

Introduction

In the rapidly evolving field of renewable energy technology, many of the novel materials considered for applications in energy generation [3, 4, 5, 6], storage [7, 8, 9], and catalysis [10] are transition metal oxides (TM oxides). The strong on-site electron correlation effects in many TM oxides [11, 12, 13] tend to localize d or f shell electrons into atomic-like orbitals and result in the opening of an energy gap, and the localized spatial distribution of these electrons leads to further self trapping through interaction with the surrounding lattice, turning them into polaronic states.

A polaron is the term for a localized charge carrier together with its induced distorted surroundings. Quantum mechanically, a polaron can be described as a quasiparticle consisting of an electron surrounded by a cloud of optical phonons [14] described by electron-phonon interactions [15, 16]. If this interaction is stronger than the average lattice thermal energy, the electron becomes self-trapped in its own potential well. Other effects aside from electron-phonon interaction could also lead to self-trapping of electrons. In particular, strong electron correlation effects [11, 12] can localize charge carriers to atomic sites, and the additional charge will then impart its effects on the surrounding lattice, causing a local distortion [13, 17, 18]. Fig. 1.1 illustrates the concept of structural distortion induced by a localized electron. In an ionic crystal, it pushes the nearby anions away and pulls the nearby cations closer. Similarly in a metal-oxygen coordination complex, it localizes on the metal d shell and pushes away the negatively charged oxygen anions, increasing the M-O bond lengths as a result.

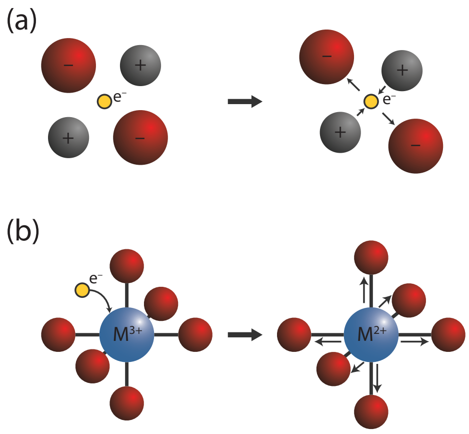

Figure 1.1: Schematic of lattice distortion due to electrostatic effects from a localized electron in (a) an ionic lattice, and (b) a metal-O_6 octahedral complex.

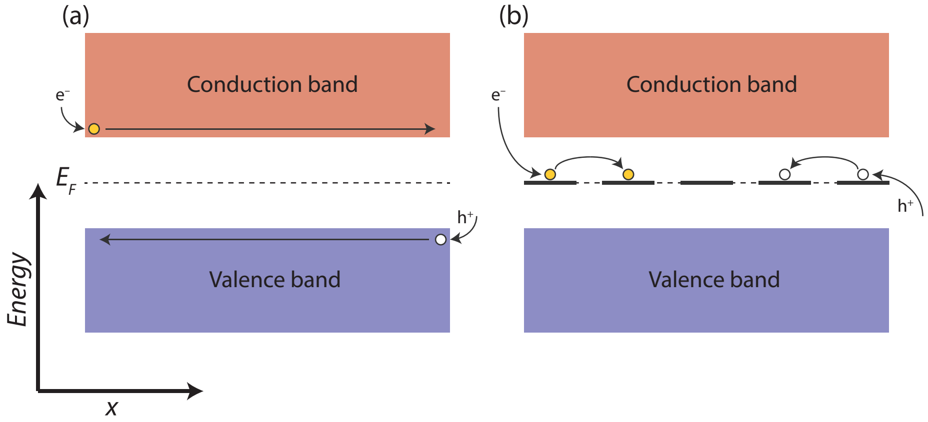

Figure 1.2: (a) Band conduction versus (b) hopping conduction. In (a), electrons in the conduction band (holes in the valence band) are delocalized and free to contribute to conductivity, spatial localization of charge carriers in (b) prevent them from moving around unobstructed.

Apart from polarons in TM oxides, there are many other materials that exhibit polaronic behaviour including ionic systems, π-conjugated polymers [19, 20, 21], as well as electron transfer processes in ion-aqueous solutions [22]. Moreover, polaron theory is closely related to electron transfer (ET) theory [23, 24] in electrochemistry. We can establish links between the concept of reorganization energy λ with the local structural distortions in the polaronic case, and adiabaticity and the electronic coupling parameter J plays a large role in both fields.

Electronically, the effects of self-trapping are depicted schematically in Fig. 1.2.

In typical semiconductors (Fig. 1.2a), injected charge carriers are inserted either in the conduction band (electrons) or the valence band (holes). These charge carriers are delocalized and contribute to the conductivity of the material. In contrast, a self-trapped state (Fig. 1.2b) cannot move out of its potential well unless it overcomes an activation energy E_a required to do so. As a result, hopping conduction is the main mechanism for polarons to move around in the material, and this drastically changes the conduction behaviour of polaronic materials. Hopping conductivity is an Arrhenius type activated process, and is typically many orders of magnitude lower than regular band-like conductivity. The picture that we have presented so far is valid for *small* polarons (also called Holstein polarons [16]), where the extent of the localization and structural distortion is limited to one lattice site or unit. On the other hand, it is also possible for the localization to spread out among many lattice sites, in which case the particle is called a *large* polaron (or Fröhlich polaron [25]).

The concept and theory of polaronic self-trapping has been extensively studied in literature [15, 16, 25]. A concept developed in the 1960s, it has seen a resurgence of interest due to the search for novel materials with applications in clean renewable technologies [5, 9, 10], and many of these materials have been found to exhibit polaronic behaviour. Additionally, the rapid increase in computational power and simultaneous development of more powerful computational methodologies [26, 27, 28, 29] over the past twenty years has provided us with the tools to accurately and efficiently study polaronic properties from first principles.

There are many examples of TM oxides in battery materials [30, 31, 32, 33, 34, 35, 36], photovoltaics [6, 37, 38], and catalysts [10, 39]. What separates TM oxides from regular semiconductors is the strongly correlated behaviour arising from the localized TM d (or f) shells. This leads to a split between the occupied and unoccupied levels of the d electrons and the opening of a gap. If this gap is purely d-like (i.e. both the valence and conduction band consist of d-level states), the material is called a Mott-Hubbard insulator [11, 12] as the gap arises purely from on-site electron correlation.

If the valence band consists of oxygen $2p$ states and the conduction band is of d character, the material is called a charge transfer (CT) insulator. The existence of polarons in TM oxides has been evident in many cases [9, 20, 40, 41, 42, 43], and many such materials have been extensively studied from first principles [30, 31, 44, 45, 46, 47].

The purpose of this thesis is to achieve a systematic understanding of adiabatic small polaron dynamics in transition metal oxides, using the powerful first principles method of density functional theory (DFT). As such, my contributions to existing literature are in the application of existing first principles methodologies to polaronic systems to improve the quantitative consistency of polaron calculations on one hand, and on the other hand through improving our fundamental and qualitative understanding of adiabatic polaron dynamics by combining elements from different theories. From a computational materials design perspective, my work provides several insights that will allow for more consistent predictions of polaronic properties in transition metal oxides using existing ab initio methods.

The main quantity determining polaron dynamics is the activation energy, or hopping barrier, E_a. By calculating the system in two states, the polaronic ground state ("POL") and the adiabatic transition state ("TS"), a state that is defined as the highest energy point on the polaron migration pathway between two ground states (and lies on the halfway point in symmetric pathways), we can extract the activation energy from the total energy difference of the two states ($E_a = E_{\text{TS}} - E_{\text{POL}}$). It is crucial to accurately calculate the TS, as any inconsistencies will lead to an exponential error in the dynamics. Aside from E_a, the polaron formation energy E_{form}, the position of the gap state inside the band gap E_p, and the adiabatic coupling parameter J are also key quantities determining the polaron characteristics of the system, and can also be calculated from the POL and TS configurations. In most materials we can compare the calculated band gap E_g with existing measurements, whereas measurements for E_p [40, 48] and E_a [48] are available for a smaller selection of materials. As such, I will study these other quantities as well, providing a more comprehensive overview of polaron properties for several materials in Chapter 3.

My improvements in methodology include the successful application of the nudged elastic band (NEB) method [49] to calculating polaronic transition states. Typically, using NEB to relax the TS will result in a 20 - 100 meV improvement of the calculated energy compared to the more commonly used approximation of linearly interpolating the coordinates. This is significant as dynamics depend exponentially on E_a. Additionally, I will employ ab initio molecular dynamics to study the hopping dynamics of polarons, and show that they are largely consistent with our predictions from NEB, demonstrating that ab initio MD could be used to study other dynamic polaron properties as well. Furthermore, I investigate the effect of DFT+U projection [50] on the calculated polaron properties, and find that one must be careful not only to provide a U-value which is chosen either through a self-consistent calculation [50, 51, 52, 53, 54, 55] or by fitting to experimentally measured properties [44, 56] with valid arguments for both choices, but must also ascertain the consistency of the projection scheme.

Using elements from a two-site hopping model (Chapter 2), we will establish a fundamental link between the adiabatic TS and the coupling term J, which is a measure of the degree of adiabaticity. We show that a nonzero J is required to accurately calculate an adiabatic TS in DFT, as DFT is inherently an adiabatic, ground state theory. We then combine this observation with elements from crystal field theory, taking into account the structural properties of typical TM oxide structures, and find that we can make qualitative predictions of polaron behaviour and adiabaticity using just the crystal structure and the electron configuration on the TM atoms as inputs.

My work focuses on TM-centered electron polarons, noting that TM-centered hole polarons are conceptually the same but with an electron removed, and hopping of hole polarons involves the transfer of an electron travelling the opposite direction. Polaron hopping on other sites, in particular hole polarons centered on O sites [42, 47, 57] is another important conduction mechanism but beyond the scope of this thesis.

This thesis is organized as follows. In Chapter 2, I review the theoretical framework used to study polaronic behaviour in transition metal oxides, combining the ab initio tool of DFT with a two-site hopping model which provides a good starting basis to quantify the properties specific to polaron hopping. I also review important elements of crystal field theory, taking into account the structural properties and symmetries common to TM oxides. Following this, I discuss the practical implementation of this theory, describing the techniques used to calculate polarons in TM oxides in DFT, and how to analyse and calculate polaronic properties from the results.

Chapter 3 investigates the effects of DFT+U projection on a selection of novel materials with applications in renewable energy generation, calculating all the aforementioned polaronic properties in these materials for a comprehensive study. This chapter has been published and is presented in modified form [1].

Chapter 4 applies my methodology to a particular system: the battery cathode material $LiFePO_4$. This chapter has also been published [2] and is presented in modified form. In this chapter, I study the hopping characteristics in the delithiated form, $FePO_4$, using both static relaxation methods as well as first principles molecular dynamics.

In Chapter 5, I combine elements of electron exchange theory with crystal structure properties of typical TM oxides and explain qualitatively the conditions required to calculate adiabatic polaron transition states.

Finally, I summarize my findings in Chapter 6, and provide an outlook and conclusion.

2

Theory

2.1 The solid state Hamiltonian

At the heart of any quantum mechanical problem lies the Schrödinger equation (SE), for which the Hamiltonian is given, in atomic units and for N electrons and M nuclei, as:

$$\begin{aligned}\hat{\mathcal{H}} = \frac{1}{2}\sum_{i}^{N}\nabla_i^2 - \sum_{i,j}^{N,M}\frac{Z_j}{|\mathbf{r}_i - \mathbf{R}_j|} + \frac{1}{2}\sum_{i\neq j}\frac{1}{|\mathbf{r}_i - \mathbf{r}_j|}& \\ + \frac{1}{2}\sum_{i}^{M}\frac{\nabla_i^2}{M_i} + \frac{1}{2}\sum_{i\neq j}\frac{Z_iZ_j}{|\mathbf{R}_i - \mathbf{R}_j|}& \qquad (2.1.1)\\ = \hat{\mathcal{T}}_e + \hat{\mathcal{V}}_{\text{ext}} + \hat{\mathcal{V}}_{\text{ee}} + \hat{\mathcal{T}}_n + \hat{\mathcal{V}}_{\text{nn}},& \qquad (2.1.2)\end{aligned}$$

where $\hat{\mathcal{T}}_e$ and $\hat{\mathcal{T}}_n$ are kinetic energy operators for the electrons and nuclei, $\hat{\mathcal{V}}_{\text{ext}}$ is the electron-nuclear potential operator, also known as the external potential operator, $\hat{\mathcal{V}}_{\text{ee}}$ is the electron-electron potential operator, and $\hat{\mathcal{V}}_{\text{nn}}$ is the nuclear-nuclear potential operator. ∇_i^2 is the Laplacian acting on the i-th particle, and M_i and Z_i are the atomic masses and charges, respectively. The full wavefunction for this Hamiltonian is of the form

$$\Psi = \Psi\left(\mathbf{r}_1, \mathbf{r}_2, \ldots, \mathbf{r}_N; \mathbf{R}_1, \mathbf{R}_2, \ldots, \mathbf{R}_M\right), \qquad (2.1.3)$$

a quantity that depends on $3N + 3M$ spatial variables excluding spin. In a solid state system, the number of variables will be on the order of 10^{23} and becomes intractable to handle directly.

The first approximation we can do is to assume that the nuclei move slowly compared to the electrons due to their much higher mass, separate the ionic and electronic variables and solve the SE in two steps. In the electronic step we keep the ionic positions fixed and solve for the electronic wavefunction, and in the ionic step we use the electronic wavefunction to calculate the interatomic forces and evolve the ionic positions. In other words,

$$\Psi = \Psi_e \times \Psi_n = \Psi\left(\mathbf{r}_1, \mathbf{r}_2, \ldots, \mathbf{r}_N\right) \times \Psi\left(\mathbf{R}_1, \mathbf{R}_2, \ldots, \mathbf{R}_M\right). \tag{2.1.4}$$

This is called the Born-Oppenheimer (BO) approximation, an adiabatic approximation. We have already decoupled the electronic and ionic motions at this level of approximation, and as a result we cannot explicitly calculate electron-phonon terms anymore. Therefore, all of this work is based on an approach where we do not consider electron-phonon interactions explicitly but treat it indirectly as an effect from structural distortions induced by the electronic configuration (e.g. when calculating polaronic ground states). Conversely, we can also alter the electronic configuration by changing the structural distortions (e.g. when calculating polaronic transition states and aligning the electronic levels according to the Franck-Condon principles).

Within the BO approximation, the electronic part of the Hamiltonian remains as the starting point for electronic structure calculations:

$$\begin{aligned}\hat{\mathcal{H}} &= \frac{1}{2}\sum_{i}^{N} \nabla_i^2 - \sum_{i,j}^{N,M} \frac{Z_j}{|\mathbf{r}_i - \mathbf{R}_j|} + \frac{1}{2}\sum_{i\neq j} \frac{1}{|\mathbf{r}_i - \mathbf{r}_j|} && (2.1.5)\\ &= \hat{\mathcal{T}}_e + \hat{\mathcal{V}}_{\text{ext}} + \hat{\mathcal{V}}_{\text{ee}}. && (2.1.6)\end{aligned}$$

2.2 Density Functional Theory

The main accomplishment of Kohn-Sham (KS) density functional theory (DFT) [58, 59, 60] is that it maps the complicated many-body interacting problem to a simpler system of non-interacting electrons moving in an effective KS-potential $V_{\mathrm{KS}}(\mathbf{r})$. The general idea is thus to reformulate the wavefunction problem, a quantity depending on $3N$ spatial variables, as an electron density problem, a quantity with only three spatial variables:

$$n(\mathbf{r}) = N \int \left|\Psi\left(\mathbf{r}, \mathbf{r}_2, \ldots, \mathbf{r}_N\right)\right|^2 \mathrm{d}\mathbf{r}_2 \ldots \mathrm{d}\mathbf{r}_N. \tag{2.2.1}$$

The goal is to express quantities in terms of the electron density and operators in terms of density functionals as follows:

$$E[n] = \langle\, \Psi[n]\, |\hat{\mathcal{T}} + \hat{\mathcal{V}}_{\mathrm{ee}} + \hat{\mathcal{V}}_{\mathrm{ext}}|\, \Psi[n]\, \rangle \tag{2.2.2}$$

$$\equiv T[n] + V_{\mathrm{ee}}[n] + \int V_{\mathrm{ext}}(\mathbf{r})n(\mathbf{r})\mathrm{d}\mathbf{r}. \tag{2.2.3}$$

The Hohenberg-Kohn (HK) theorems [58] state that it is possible to uniquely determine all ground state properties of a system with the electron density as input, and that the correct ground state density minimizes the total energy functional of Eq. (2.2.3). In principle this is an exact map of the wavefunction problem with $3N$ variables to a density problem with only 3 variables, but in practice the analytical expressions for $T[n] \equiv \langle\, \Psi[n]\, |\hat{\mathcal{T}}|\, \Psi[n]\, \rangle$ and $V_{\mathrm{ee}}[n] \equiv \langle\, \Psi[n]\, |\hat{\mathcal{V}}_{\mathrm{ee}}|\, \Psi[n]\, \rangle$ are not known.

Kohn and Sham [59] (KS) replaced the full system of Eq. (2.2.3) with an auxiliary system of non-interacting quasiparticles $\psi_i(\mathbf{r})$ that sum up to the same density as the original system:

$$n(\mathbf{r}) = \sum_i^N \left|\psi_i(\mathbf{r})\right|^2. \tag{2.2.4}$$

This leads to an exact expression for the non-interacting kinetic energy functional, $T_{\mathrm{KS}}[n]$. Additionally, we can pull out the Hartree energy from $V_{\mathrm{ee}}[n]$ and obtain the

KS energy functional:

$$E_{\mathrm{KS}}[n] = T_{\mathrm{KS}}[n] + \int V_{\mathrm{ext}}(\mathbf{r})n(\mathbf{r})\mathrm{d}\mathbf{r} + \frac{1}{2}\int \frac{n(\mathbf{r})n(\mathbf{r}')}{|\mathbf{r}-\mathbf{r}'|}\mathrm{d}\mathbf{r}\mathrm{d}\mathbf{r}' + E_{\mathrm{XC}}[n]. \tag{2.2.5}$$

We have now replaced all the unknown terms within $E_{\mathrm{XC}}[n]$, the energy functional that describes the complicated quantum mechanical exchange and correlation effects of the system. The resulting KS equations for the one-electron KS wavefunctions are given as

$$\hat{\mathcal{H}}_{\mathrm{KS}}\psi_i(\mathbf{r}) = \left[-\frac{1}{2}\nabla^2 + V_{\mathrm{KS}}(\mathbf{r})\right]\psi_i(\mathbf{r}) = \epsilon_i\psi_i(\mathbf{r}). \tag{2.2.6}$$

where

$$V_{\mathrm{KS}}(\mathbf{r}) = V_{\mathrm{ext}}(\mathbf{r}) + V_{\mathrm{H}}(\mathbf{r}) + V_{\mathrm{XC}}(\mathbf{r}), \tag{2.2.7}$$

$$V_{\mathrm{XC}}(\mathbf{r}) \equiv \frac{\delta E_{\mathrm{XC}}[n]}{\delta n(\mathbf{r})}, \qquad V_{\mathrm{H}}(\mathbf{r}) \equiv \frac{\delta E_{\mathrm{H}}[n]}{\delta n(\mathbf{r})} = \int \frac{n(\mathbf{r}')}{|\mathbf{r}-\mathbf{r}'|}\mathrm{d}\mathbf{r}'. \tag{2.2.8}$$

The mapping of Eq. (2.2.3) to Eq. (2.2.5) is exact provided we know the exact form of $E_{\mathrm{XC}}[n]$, so in principle no approximations have been made so far. The limitations of DFT is firstly that it is a ground state theory, i.e. higher energy states calculated in DFT have no physical meaning. Additionally, the KS wavefunctions do not represent true interacting many-body electrons, and the corresponding KS eigenvalues therefore do not have a formal physical meaning [61]. In practice, we treat this as an approximation and possible source of error.

To solve the KS equations in practice, we note that this is a self-consistent problem. More specifically, the density $n(\mathbf{r})$ depends on the KS orbitals $\psi_i(\mathbf{r})$ (Eq. 2.2.4), which are obtained by solving the KS Hamiltonian (Eq. 2.2.6). However, the KS potential $V_{\mathrm{KS}}(\mathbf{r})$ is calculated from the density $n(\mathbf{r})$ (Eq. 2.2.7), resulting in a self-consistent cycle. Typically, we start with an initial guess for $n(\mathbf{r})$ and iteratively improve our solutions until self-consistency is reached, i.e., $n_{\mathrm{new}}(\mathbf{r}) \approx n_{\mathrm{old}}(\mathbf{r})$.

2.2.1 Exchange and correlation

Although unknown in exact form, the exchange-correlation (XC) energy E_{XC} includes all the quantum mechanical effects that are crucial for describing the correct physics of a system. Technically, we can further separate this term into its exchange and correlation energies

$$E_{\mathrm{XC}} = E_{\mathrm{X}} + E_{\mathrm{C}}, \tag{2.2.9}$$

where the exchange term E_{X} describes the exchange interactions arising from the Pauli exclusion principle and the correlation term E_{C} represents the complicated many-body electron-electron Coulomb interactions not included in the Hartree term. The development of accurate XC functionals is an active field of research but is beyond the scope of this work. Instead, we shall briefly outline a few examples of common XC functionals and state how these approaches fail to predict the correct behaviour in materials with band gaps and strongly correlated materials.

The local density approximation (LDA) uses only the density as input and uses the properties of the analytically solvable homogeneous electron gas (HEG) to approximate the actual, inhomogeneous system:

$$E_{\mathrm{XC}}^{\mathrm{LDA}}[n] = \int \epsilon_{\mathrm{XC}}^{\mathrm{HEG}}[n(\mathbf{r})]\mathrm{d}\mathbf{r}. \tag{2.2.10}$$

The functionals created by von Barth and Hedin (VBH) [62] and Ceperley and Alder (CA) [63] are examples of LDA functionals.

Generalized gradient approximations (GGA) seem to be more sophisticated by including the gradient of the density as input:

$$E_{\mathrm{XC}}^{\mathrm{GGA}}[n] = \int F\left[n(\mathbf{r}), \nabla n(\mathbf{r})\right] \mathrm{d}\mathbf{r}, \tag{2.2.11}$$

although it is not a guarantee that they will do better than LDA functionals as both are still approximations to the true XC energy. Examples of GGA functionals include the Perdew-Wang 91 (PW91) [64] and Perdew-Burke-Ernzerhof (PBE) [65] functionals. The PBE functional is currently the most widely used functional in DFT calculations. These functionals work remarkably well for most "well-behaved" materials whose properties do not deviate much from the HEG, and LDA/GGA DFT has been highly successful in predicting bulk properties of most materials.

However, standard LDA/GGA suffers from a number of deficiencies, and it systematically underestimates band gaps of strongly correlated systems such as transition metal oxides. We will not elaborate on the exact mechanisms behind these phenomena but we will briefly outline two popular methods that we have applied in this work and have seen successes in handling such strongly correlated materials.

2.2.2 DFT+U

In strongly correlated systems, in particular the d and f transition metal oxides, the strong on-site Coulomb interaction leads to localization of the d (or f) electrons onto atomic-like orbitals centered on the transition metals. The DFT+U method [28, 66, 67, 68, 69] attempts to capture this interaction by separating the electrons into a set of delocalized electrons (typically the s and p electrons) on which standard LDA/GGA is applied, and a separate set of electrons considered localized (typically the d or f electrons) treated in a Hubbard-like fashion. Originally coined LDA+U, it has since been extended to other semilocal functionals such as GGA and we therefore group these together under the general term DFT+U.

Our focus is on d electrons, although the process is similar for other orbitals considered to be localized (f orbitals, and in some cases, p orbitals). The energy contributions of these localized d electrons are, in the rotationally invariant scheme, of the form

$$E_{\mathrm{U}} = \frac{1}{2} U \sum_{i \neq j} n_i n_j, \tag{2.2.12}$$

where n_i denotes the d orbital occupancies. U is the on-site screened Coulomb energy, the main parameter that enters in this theory. We now include this energy term in the total energy and subtract from it the so-called double counting term E_{dc} which represents the contributions of the same d electrons that already exist in LDA/GGA:

$$E_{\mathrm{dc}} = \frac{1}{2} U N_d (N_d - 1), \tag{2.2.13}$$

where $N_d = \sum_i n_i$ is the total number of d electrons. Summed together, the LDA+U energy becomes

$$E_{\mathrm{LDA+U}} = E_{\mathrm{LDA}} - \frac{1}{2} U N_d (N_d - 1) + \frac{1}{2} U \sum_{i \neq j} n_i n_j. \tag{2.2.14}$$

This expression for the general DFT+U energy implies a quadratic relation of the DFT+U energy with respect to orbital occupation n_i, and the implications will be discussed in more detail in Chapter 3. The eigenenergies ϵ_i can be expressed as

$$\epsilon_i = \frac{\partial E}{\partial n_i} = \epsilon_{\mathrm{LDA}} + U \left(\frac{1}{2} - n_i \right), \tag{2.2.15}$$

and result in a downward shift in energy for occupied orbitals by $U/2$ and an upward shift by the same energy for empty orbitals. In Mott-Hubbard insulators, this results in the opening of a gap in cases where standard LDA/GGA fails to predict a gap between TM d states. Similarly, the on-site orbital dependent potential $V_i(r)$ is given as

$$V_i(r) = \frac{\delta E}{\delta n_i} = V_{\mathrm{LDA}}(r) + U \left(\frac{1}{2} - n_i \right), \tag{2.2.16}$$

which implies a repulsive Hubbard potential for $n_i < 1/2$, and an attractive potential otherwise. The physical interpretation is that the system is driven towards integer occupation of the n_i sites, thereby favouring localization of the d electrons.

Implementing the DFT+U method requires a more concrete definition of n_i as we need to identify the localized states that the orbital-dependent potential is to act upon. This can be done most consistently for d and f electrons as they tend to retain their atomic character when localized to their respective TM sites. In the projector augmented wave (PAW) method [26, 27] as well as in the augmented plane wave (APW) method [70], two widely used methods in DFT, the on-site occupancy is defined as a projected orbital density matrix:

$$n^{t,\sigma}_{m,m'} = \sum_{n,\mathbf{k}} f^{\sigma}_{n,\mathbf{k}} \left\langle \Psi^{\sigma}_{n,\mathbf{k}} | P^{t}_{m,m'} | \Psi^{\sigma}_{n,\mathbf{k}} \right\rangle , \tag{2.2.17}$$

where $\Psi^{\sigma}_{n,\mathbf{k}}$ is the crystal wavefunction, $f^{\sigma}_{n,\mathbf{k}}$ is the Fermi distribution, t is the site index, σ is the spin, and m and m' are the orbital magnetic quantum numbers. The operator $P^{t}_{m,m'}(\mathbf{r},\mathbf{r}')$ projects the crystal wavefunction onto spherical harmonics $Y_{l,m}(\hat{\mathbf{r}})$:

$$P^{t}_{m,m'}(\mathbf{r},\mathbf{r}') = \theta_{\Omega_t}(\mathbf{r}) \delta \left(|\mathbf{r}' - \mathbf{R}_t| - |\mathbf{r} - \mathbf{R}_t| \right) Y_{l,m}(\hat{\mathbf{r}}) Y^{*}_{l,m'}(\hat{\mathbf{r}}'). \tag{2.2.18}$$

Importantly, $\theta_{\Omega_t}(\mathbf{r})$ is a step function and equals 1 for $r < r_c$ and zero everywhere else. The implications of this hard cutoff are discussed in Chapter 3. In general, any basis set requires a definition for the projection operator as the local atomic orbitals need to be defined, although this definition is more straightforward for local basis sets compared to plane wave basis sets. Additionally, the projection method is ambiguous as other definitions are also available [71].

To summarize, DFT+U is a local method that requires only a projection to on-site orbitals and therefore has no computational penalty compared to standard LDA/GGA. As such it is a computationally efficient method to treat strong on-site Coulomb correlations. The disadvantage is that it is orbital dependent, and therefore projection dependent, which could potentially lead to unpredictable results if the projection is inconsistent or if the electrons prefer to localize on orbitals less atomic in character, e.g. if they hybridize with the neighbouring ligands while remaining localized within the MO$_6$ complex. Chapter 3 will discuss the implications of different projections as well as the quadratic dependence of E_{U} on the orbital occupation n_i.

2.2.3 Hybrid functionals

Hartree-Fock (HF) theory describes the electronic exchange through a four-point exchange integral over individual orbitals in a Slater determinant. This allows us to calculate the exact electron exchange by construction. In the absence of any electron correlations, this leads to large errors and overestimation of band gaps [72]. Hybrid functionals [29, 73] include a fraction of the exact exchange in the energy calculated by GGA as a compromise between the overbinding in HF and underbinding of GGA.

The HF wavefunction is defined as a Slater determinant,

$$\Psi(\mathbf{r}_1, \mathbf{r}_2, \ldots, \mathbf{r}_N) \equiv \frac{1}{\sqrt{N!}} \begin{vmatrix} \phi_1(\mathbf{r}_1) & \phi_2(\mathbf{r}_1) & \cdots & \phi_N(\mathbf{r}_1) \\ \phi_1(\mathbf{r}_2) & \phi_2(\mathbf{r}_2) & \cdots & \phi_N(\mathbf{r}_2) \\ \vdots & \vdots & \ddots & \vdots \\ \phi_1(\mathbf{r}_N) & \phi_2(\mathbf{r}_N) & \cdots & \phi_N(\mathbf{r}_N) \end{vmatrix}, \tag{2.2.19}$$

which is antisymmetric by construction and therefore always satisfies the Pauli exclusion principle. The Fock exchange energy is given by

$$E_{\mathrm{X}} = -\frac{1}{2} \sum_{i,j} f_i f_j \int \frac{\phi_i^*(\mathbf{r}) \phi_j^*(\mathbf{r}') \phi_i(\mathbf{r}') \phi_j(\mathbf{r})}{|\mathbf{r} - \mathbf{r}'|} \mathrm{d}\mathbf{r} \mathrm{d}\mathbf{r}', \tag{2.2.20}$$

which is a four point integral over the orbitals ϕ_i. The corresponding Fock exchange potential is given by

$$V_{\mathrm{X}}(\mathbf{r}, \mathbf{r}') = -\frac{1}{2} \sum_{i} f_i \frac{\phi_i^*(\mathbf{r}') \phi_i(\mathbf{r})}{|\mathbf{r} - \mathbf{r}'|} \tag{2.2.21}$$

Pure HF includes only the Fock exchange energy without any electron correlation. Therefore, a sensible compromise is found within the hybrid functionals which combine a fraction of exact exchange E_{X} with the exchange and correlation energies calculated in LDA/GGA. An example of a hybrid functional typically used in solid state problems is PBE0 [29] which sets the fraction of exact exchange to $\alpha = 0.25$:

$$E_{\mathrm{PBE0,XC}} = \frac{1}{4} E_{\mathrm{HF,X}} + \frac{3}{4} E_{\mathrm{PBE,X}} + E_{\mathrm{PBE,C}}. \tag{2.2.22}$$

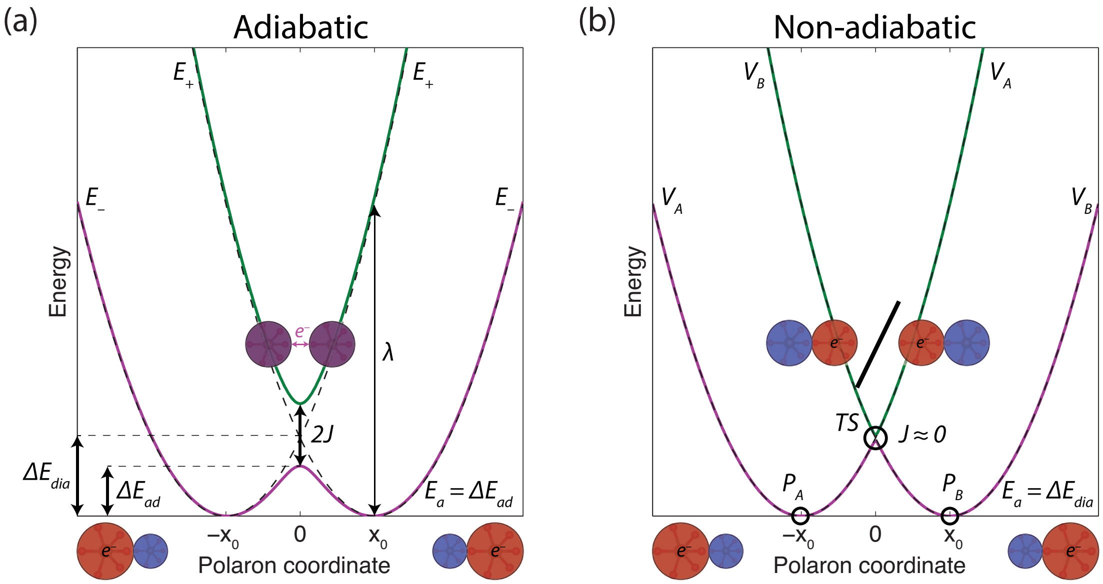

Figure 2.1: Energy levels calculated from the two site hopping model in the (a) adiabatic and (b) diabatic (non-adiabatic) case.

This fraction $\alpha \approx 1/4$ was shown [29, 74] to best reproduce the atomization energies of most molecular systems. The screened variant, called the Heyd-Scuseria-Ernzerhof (HSE) [73] functional, replaces the $1/r$ long range Coulomb interaction with a more rapidly decaying error function to improve computational efficiency, and has seen widespread success in many systems. Additionally, it can be shown [75] that hybrid functionals and DFT+U can have similar effects on localized orbitals within the on-site regions.

In summary, the advantage of hybrid functionals is that exact exchange is non-local and acts on all orbitals independent of projection. Therefore, the method is seen to be more robust compared to DFT+U in treating strong correlation effects. The disadvantage is that we require calculation of the non-local Fock exchange energy E_{X}, and this is computationally expensive. In practice, hybrid functional calculations are one to two orders of magnitude slower than comparable DFT/DFT+U calculations.

2.3 The two-site polaronic transfer model

In second quantization formalism, the model Hamiltonian for a two site hopping system may be written as [76, 77]

$$\begin{aligned}\mathcal{H} = \frac{M}{2}\left(v_A^2 + v_B^2\right) + \frac{M}{2}\omega^2\left(x_A^2 + x_B^2\right) \\ + A\left(x_A - x_B\right)\left(\hat{a}_A^\dagger \hat{a}_A - \hat{a}_B^\dagger \hat{a}_B\right) + J\left(\hat{a}_A^\dagger \hat{a}_B + \hat{a}_B^\dagger \hat{a}_A\right),\end{aligned} \tag{2.3.1}$$

where M is the polaron effective mass, A is an electron-phonon coupling parameter, and J denotes the inter-site exchange coupling parameter. The annihilation and creation operators are given as $\hat{a}_{1,2}/\hat{a}_{1,2}^\dagger$. In the original model [76, 77], $x_{\mathrm{A/B}}$ and $v_{\mathrm{A/B}}$ represent the coordinates and velocities of the two ions near their respective sites. In this work, we define $x_{\mathrm{A/B}}$ as the "polaron coordinate", which is taken to be a single, averaged description for the distortion of local bonds around the polaronic site. We will further elucidate this definition in Section 2.5. The harmonic oscillation frequency in each polaronic well as sketched in Fig. 2.1 is defined as ω and is typically approximated as a single characteristic optical phonon frequency ω_{op} [77].

We now introduce a further simplification of the polaron coordinates $x_{\mathrm{A/B}}$ and only look at their difference $x = x_A - x_B$. Ignoring center of mass $(x_A + x_B)/2$ terms, we can simplify Eq. (2.3.1) to

$$\mathcal{H} = \frac{M}{2}v^2 + \frac{M}{2}\omega^2 x^2 + Ax\left(\hat{a}_A^\dagger \hat{a}_A - \hat{a}_B^\dagger \hat{a}_B\right) + J\left(\hat{a}_A^\dagger \hat{a}_B + \hat{a}_B^\dagger \hat{a}_A\right), \tag{2.3.2}$$

where we now have a single coordinate and velocity $v = dx/dt$ for the system. To find the energies of this Hamiltonian, we apply the Heisenberg equation of motion, $\frac{\mathrm{d}}{\mathrm{d}t}\hat{a}_i(t) = \frac{i}{\hbar}[\mathcal{H}, \hat{a}_i]$, and note the time evolution of $\hat{a}_i$ as $\hat{a}_i(t) = \hat{a}_i \exp iEt/\hbar$. We also approximate x to vary slowly over time ($dx/dt = v = 0$). Solving for the energies, we then obtain

$$E_\pm(x) = \frac{\omega^2 M}{4}x^2 \pm \sqrt{A^2x^2 + J^2}, \tag{2.3.3}$$

with lower E_- and upper E_+ energy branches as shown in Fig. 2.1. We now further rewrite this expression by introducing the following substitutions, $\lambda = A^2/M\omega^2$ and $y = (M\omega^2/4A)x$:

$$E_\pm(y) = \lambda y^2 \pm \sqrt{\lambda^2 y^2 + J^2}. \tag{2.3.4}$$

As shown in Fig. 2.1, this substitution introduces the reorganization energy λ in terms of the other parameters of the model. This is advantageous as λ is a well defined concept in electron transfer theory [23] and a more tractable quantity compared to the other parameters A, M, and ω.

Analyzing this function in greater depth, we first shift the energies so that the two minima are at zero energy by adding a constant to Eq. (2.3.4) (as is done in Fig. 2.1):

$$E'_\pm(y) = \lambda y^2 \pm \sqrt{\lambda^2 y^2 + J^2} + C \equiv E_\pm(y) + \Delta E_{\text{dia}}, \tag{2.3.5}$$

where we define the constant ΔE_{dia} as the diabatic (non-adiabatic) crossover energy. Solving for this constant, we obtain $\Delta E_{\text{dia}} = \frac{\lambda}{4} + \frac{J^2}{\lambda}$. The two minima of E_- are given by $y_0 = \pm\sqrt{\frac{1}{4} - \frac{J^2}{\lambda^2}}$. We can define the adiabatic crossover energy, ΔE_{ad}, as the value of the lower energy branch E'_- at the crossover point $y = 0$: $\Delta E_{\text{ad}} \equiv E'_-(0) = \Delta E_{\text{dia}} - J$. Further simplifying these quantities by neglecting the higher order terms in J, we then obtain:

$$\Delta E_{\text{dia}} \approx \frac{\lambda}{4}, \tag{2.3.6}$$

$$\Delta E_{\text{ad}} \approx \frac{\lambda}{4} - J, \tag{2.3.7}$$

$$y_0 \approx \pm\frac{1}{2} \Longrightarrow x_0 \approx \pm\frac{2A}{M\omega^2}. \tag{2.3.8}$$

From this, we can see that this model reproduces Marcus ET theory [23], expressing the diabatic (non-adiabatic) crossover energy ΔE_{dia} as a quarter of the reorganization energy λ. We can also see the effect of the coupling parameter J, which acts to split the energy levels of the lower and upper branches at the crossover point ($x = 0$)

by $2J$ and relates the adiabatic crossover energy through $\Delta E_{\mathrm{ad}} = \Delta E_{\mathrm{dia}} - J$. The importance of J is such that a significant part of this work revolves around it, and I will discuss this in more detail in the following section.

2.3.1 Adiabaticity and the exchange parameter J

The original adiabatic theorem states [24, 78] that a system undergoing a perturbation will remain in its eigenstate as long as the perturbation happens gradually. An adiabatic process thus describes a system whose external conditions vary slowly over time, so that we can solve for its state while keeping the external conditions fixed. A particular example of an adiabatic approximation is the Born-Oppenheimer approximation, which assumes the ions to be at rest initially, solves for the electronic structure of this system, and then uses this solution to derive the properties of the system. In other words, it decouples the ionic and electronic wavefunctions by virtue of the ions having much higher mass compared to the electrons. In contrast, a diabatic or non-adiabatic process is a process where the external conditions change so fast that the system has had no time yet to relax to its new ground state.

The concept of adiabaticity is inherently coupled to the exchange term J, which describes the splitting due to inter-site exchange interaction. If ϕ_A and ϕ_B describe the state of an electron located at site A and B respectively, a generic expression for J is given as follows [79]:

$$J = \int \phi_A^* \left(\mathcal{H} - \epsilon_0\right) \phi_B \mathrm{d}\tau, \tag{2.3.9}$$

where $\mathcal{H}$ is the Hamiltonian of the system, ϵ_0 is the energy of ϕ_A and ϕ_B, and the integral extends over all relevant coordinates (and spins). When the two degenerate states ϕ_A and ϕ_B are brought together, their interaction will lift the degeneracy and, due to symmetry, combine the two states together in “bonding” ($\phi_+ = \phi_A + \phi_B$) and “antibonding” states ($\phi_- = \phi_A - \phi_B$) in much the same way as in a molecular two-site system (see Fig. 2.2a). The energy difference between these two states is equal to $2J$.

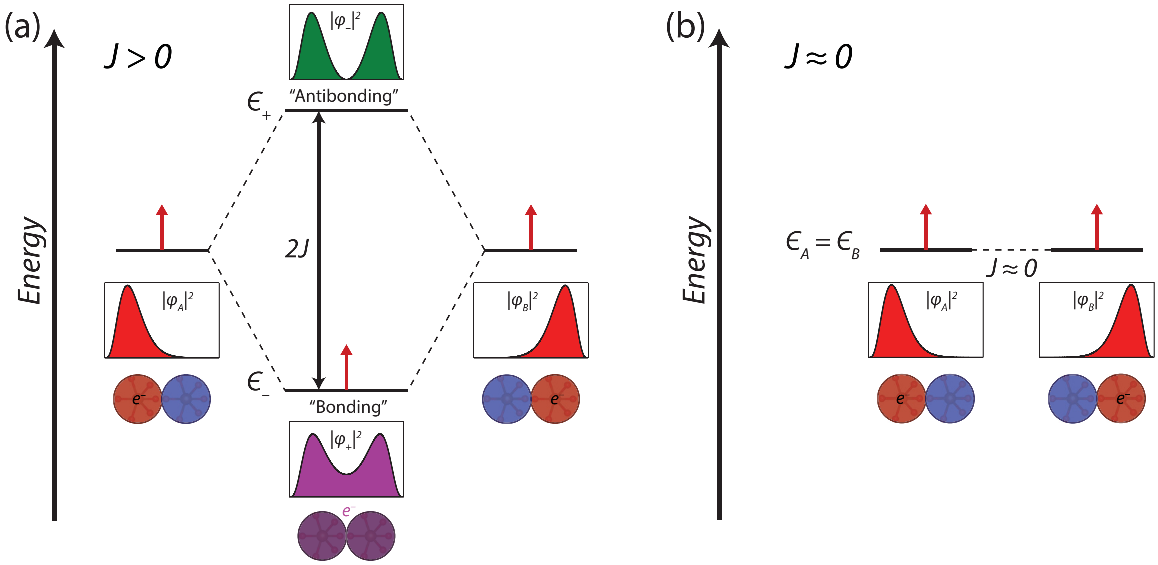

Figure 2.2: Energy diagrams for a two-site system in the (a) adiabatic and (b) non-adiabatic cases. In the presence of an interaction J, the two initially degenerate states (ϕ_A and ϕ_B) combine into bonding (ϕ_+) and antibonding (ϕ_-) states, while they remain degenerate in the non-adiabatic case. Note that the energies corresponding to $\phi_\pm$ are defined as $\epsilon_\mp$.

The electronic oscillation frequency between these two states can be given as

$$\omega_{\mathrm{el}} \approx \frac{2J}{\hbar}. \tag{2.3.10}$$

This is not valid for the polaronic case where we also need to consider phonon interactions, but it can still give us an order of magnitude estimate. We can directly relate the situation depicted in Fig. 2.2a with the crossover point in Fig. 2.1a, also called the adiabatic transition state (TS).

We can now establish a connection between adiabaticity and J by comparing the situation for $J > 0$ in Figs. 2.2a and 2.1a with the situation for $J \approx 0$ in Figs. 2.2b and 2.1b. If $J > 0$, there is a clearly defined lower energy branch (E_-) in Fig. 2.1a that the system can follow adiabatically when transitioning from site A to site B. If $J \approx 0$ however (Fig. 2.2b), there is almost no interaction between ϕ_A and ϕ_B and the two sites remain degenerate in energy. The energy curves V_A and V_B in Fig. 2.1b also remain separate with one curve for each site, and there is no mechanism for the system to transition adiabatically from one curve (V_A) to another (V_B). Hence, if $J \approx 0$, the only possible transition mechanisms are diabatic (e.g. tunneling vertically from V_A to V_B without changing the x-coordinate in Fig. 2.2b), leading to the connection between adiabaticity and J. A more specific criterion for adiabaticity in the two-site model is given in the next section.

The $J > 0$ and $J \approx 0$ cases have particular implications on DFT calculations on the TS. Again, if J is nonzero then the coupling combines the two separate states ϕ_A and ϕ_B into "bonding" (ϕ_+) and "antibonding" (ϕ_-) states (Fig. 2.2a), with their energetic difference $E_+ - E_-$ equal to $2J$. As the lowest state ϕ_+ is a single state that encompasses both sites, the density configuration of this state will be $\left(\frac{1}{2}, \frac{1}{2}\right)$, a notation depicting both sites as having half of the electron density. This configuration is stable against small perturbations, as even if ϕ_A and ϕ_B differ slightly in energy, their coupling remains intact and the single bonding state will persist. However, in the nonadiabatic case when $J \approx 0$ (Fig. 2.2b), there is no coupling and the two states ϕ_A and ϕ_B remain spatially separate and degenerate in energy. If they are perfectly symmetric, a DFT calculation will still result in a $\left(\frac{1}{2}, \frac{1}{2}\right)$ distribution of the density. However, in this case any perturbation will break the symmetry and change the energy of ϕ_A with respect to ϕ_B. This will result in the complete filling of one site over the other $(1, 0)$ or $(0, 1)$. In any DFT calculation, the result will be a $(1, 0)$ or $(0, 1)$ configuration, as ϕ_A and ϕ_B are never identical due to numerical inaccuracies (typically, one POL state is 1-5 meV higher or lower in energy compared to another POL state).

2.3.2 Polaron characteristic scales and hopping rates

From the derivations shown in more detail in Ref. [77], there are three resulting characteristic polaron parameters which can be utilized to understand how hopping should be treated in a given system:

$$\eta_1 = J/E_a \qquad \text{(Polaron size)} \qquad (2.3.11)$$

$$\eta_2 = \frac{J^2}{\hbar\omega\sqrt{E_a kT}} \qquad \text{(Adiabaticity)} \qquad (2.3.12)$$

$$\eta_3 = J^2/E_a kT \qquad \text{(Nearest-neighbour)}, \qquad (2.3.13)$$

where η_1, η_2, and η_3 describe, respectively, the polaron size, adiabaticity, and the validity of the nearest-neighbour approximation. If $\eta_1 \ll 1$, the polaron size is small, giving us a rough guideline on the relative magnitude of J compared to the activation energy E_a. η_3 determines the validity of the two-site model. If $\eta_3 \ll 1$, then only nearest-neighbour hopping needs to be considered, in which case the usage of a two-site model is justified.

The hopping rate Γ derived from this two-site model is divided into adiabatic and diabatic regimes depending on the value of the adiabaticity parameter η_2 [77]:

$$\Gamma = \frac{\omega}{2\pi} e^{-E_a/kT} \times \begin{cases} 1 & (\eta_2 > 1) \\ \pi^{3/2}\eta_2 & (\eta_2 \ll 1). \end{cases} \qquad (2.3.14)$$

Importantly, this parameter allows one to determine the applicability of ground-state adiabatic DFT to a problem that is inherently diabatic. For $\eta_2 > 1$, we are in the adiabatic regime. If however $\eta_2 \ll 1$, the adiabatic approximation will no longer be valid. Either case of the resulting expression in Eq. (2.3.14) gives an exponential relationship between the hopping rate and the activation energy E_a. This energy E_a is the difference in total energy between the transition state and the ground states $E_a = E_{\mathrm{TS}} - E_{\mathrm{GS}}$. Such total energies can be extracted from ab initio calculations – where E_{TS} is the total energy at the transition state and E_{GS} is the total energy at the ground state. I shall discuss the adiabatic and diabatic (nonadiabatic) cases separately.

The adiabatic case

If $\eta_2 > 1$, Eq. (2.3.14) reduces to

$$\Gamma = \frac{\omega}{2\pi} e^{-E_a/kT}, \tag{2.3.15}$$

where $E_a \equiv E_{\text{ad}} \approx E_{\text{dia}} - J$. This is a typical Arrhenius-like behaviour where the hopping rate, conductivity, and mobility all depend exponentially on the activation energy and the temperature.

The diabatic (non-adiabatic) case

If $\eta_2 \ll 1$, Eq. (2.3.14) becomes

$$\Gamma = \frac{2\pi}{\hbar} J^2 \frac{1}{\sqrt{4\pi\lambda kT}} e^{-E_{\text{dia}}/kT}, \tag{2.3.16}$$

where the activation energy is now $E_a \equiv E_{\text{dia}}$. Importantly, the hopping prefactor now has an explicit dependence on J^2. As J is small for diabatic cases, we can expect non-adiabatic hopping to be far less frequent compared to the adiabatic case. We note that Eq. (2.3.16) is the same as the relation derived from electron transfer theory [23, 24], indicating a relation between diabatic hopping in this model and electron transfer reactions in, for example, molecular systems.

2.4 Crystal Field Theory

I briefly review the main elements of crystal field theory [80, 81], a basic model describing the behaviour of localized transition metal d (or f) states surrounded by a regular configuration of anions (typically O atoms) as is the case in TM oxides. We can extend the same view to TM-centered polarons as they can be treated as adding one more electron (or hole) to the TM with a distortion and possible reduction of the local symmetry. Crystal field theory, as its name implies, describes the symmetry breaking due to the crystal field or ligand field of the anions surrounding the metal cation. In TM oxides, the metal ion typically either has four (tetrahedral coordination) or six (octahedral coordination) neighbouring anions, the latter being the most common. This work is focused on octahedral MO_6 configurations.

A freestanding metal cation (such as Fe^{3+}) has perfect spherical symmetry, and its five (half-filled) $3d$ orbitals therefore have the same energy as shown on the left side of Fig. 2.3. However, when the atom is surrounded by six anions ($[O^{2-}]_6$) with octahedral symmetry, the degeneracy of the $3d$ orbitals is lifted by the resulting octahedral ligand field (see Fig. 2.3). A qualitative explanation is that the O^{2-} anions are negatively charged and therefore tend to repel the nearby $3d$ electrons. This increases the energy of the $3d$ orbitals pointing towards the anions (i.e. the d_{z^2} and $d_{x^2-y^2}$ orbitals) with respect to the $3d$ orbitals that are pointing towards directions in between the anions (i.e. the d_{xy}, d_{yz}, and d_{xz} orbitals). In the octahedral case, the three orbitals with lower energy are called t_{2g} orbitals, and the two orbitals higher in energy are called e_g orbitals. The splitting energy, which is the energy difference between the two, is called Δ_O. The magnitude of Δ_O depends on the configuration of the metal ion (oxidation state and position in the periodic table) and the ligands around it and will be greater when the oxidation state is higher and when the surrounding ligand field is stronger, as well as when the metal ion is further down the periodic table (Δ_O is typically higher in $4d$ transition metals compared to their $3d$ predecessors).

2.4.1 High and low spin complexes

The common occurrence of octahedral complexes combined with this splitting has large implications on the spin state of such complexes. When all d (or f) orbitals have the same energy, filling of these orbitals is straightforward and goes according to Hund's rule. However, when the orbital degeneracy is lifted and the t_{2g} orbitals are filled with three electrons, the next e_g orbital will be Δ_O higher in energy. If Δ_O is lower than the energy required to place the electron into one of the other singly

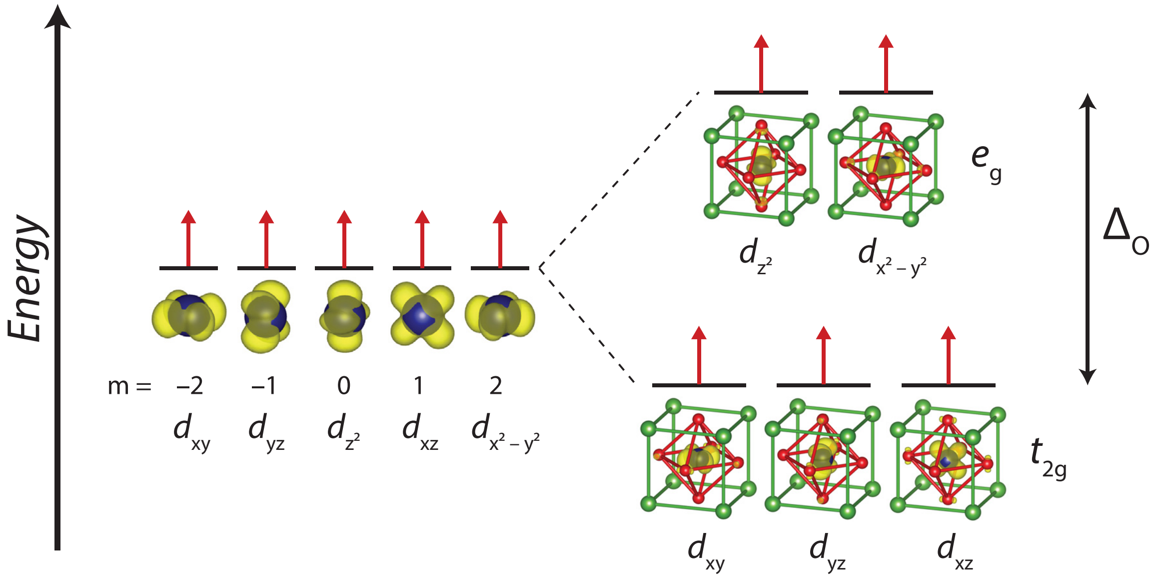

Figure 2.3: Splitting of the d orbitals by an octahedral crystal field. Initially, on the left, all d orbitals are degenerate due to spherical symmetry, but when the metal atom is placed inside an octahedral MO_6 complex, the orbitals split into a set of lower energy (t_{2g}) and higher energy (e_g) orbitals, with Δ_O the difference between the energy levels. Note: these orbitals are taken from a DFT+U calculation in an example perovskite material. As such, the orbitals are similar, but not identical, to pure atomic orbitals.

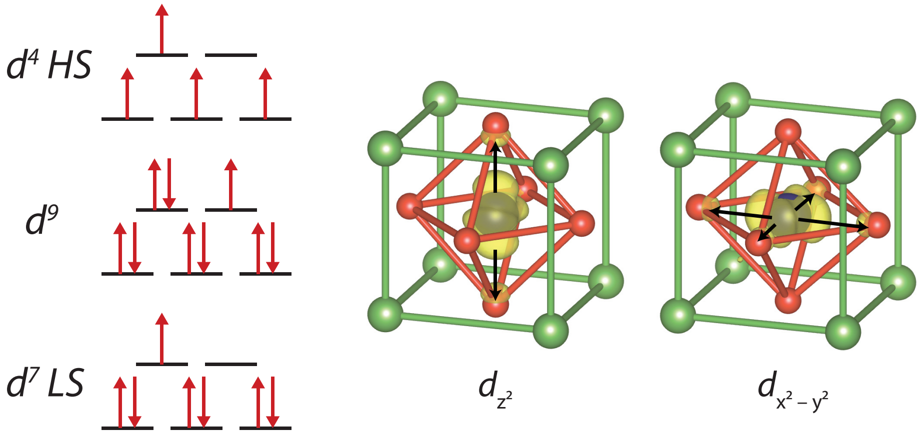

Figure 2.4: The Jahn-Teller effect most visible to odd e_g occupancies. The degeneracy of the d_{z^2} and $d_{x^2-y^2}$ orbitals is lifted once a geometric distortion acts to either compress or elongate the MO_6 octahedron, lowering the energy level of one orbital compared to the other.

occupied t_{2g} orbitals (Δ_H) then the e_g orbitals will be filled next as shown in Fig. 2.3 where all five $3d$ electrons of the example Fe^{3+} ion are unpaired. This configuration is also called high spin (HS) as it maximizes the total spin based on the number of electrons in the d shell. If however Δ_O is higher than the intraorbital repulsion energy Δ_H, the system will favour completely filling the t_{2g} orbitals first before placing electrons into the e_g orbitals. This configuration is also called low spin (LS). A few examples of such HS and LS configurations are shown on the left in Fig. 2.4.

2.4.2 *The Jahn-Teller effect*

An additional corollary to crystal symmetry breaking is the so-called Jahn-Teller (JT) effect [82, 83], whose eponymous theorem states that a system with spatially degenerate ground states will distort and break its symmetry and lower the energy of one of these states [82, 83]. This effect is illustrated in Fig. 2.4 where all three electronic configurations displayed have a degeneracy in the e_g orbitals. These orbitals (d_{z^2} and $d_{x^2-y^2}$) have the same energy, although from their different spatial configurations (as shown on the right in Fig. 2.4) we can see that electrostatic interactions arising from the charge distribution prefer either pushing the opposing z-ligands outwards (d_{z^2} configuration), or pushing the x- and y- ligands outwards ($d_{x^2-y^2}$ configuration). In both cases this will lower the total energy and thereby lift the degeneracy. Thus, JT distorted octahedral complexes are either elongated or compressed depending on which e_g orbital is singly occupied. JT effects are particularly strong in the e_g orbitals (for octahedral complexes), as they both point toward the ligands. The effect also exists in t_{2g} orbitals but is much smaller as the t_{2g} orbitals do not point toward the ligands.

2.5 Computational details

2.5.1 *Definition of the reaction coordinate*

The reaction coordinates x_A and x_B discussed in the two-site model in Chapter 2 are of special importance. Originally, this model was devised for a one dimensional chain of ions [76, 77] in which the meaning of $x_{A/B}$ is straightforward, as is the harmonic potential dependence based on deviations of this coordinate from equilibrium. I have translated this to my case of MO_6 octahedron-centered polarons by noting that this harmonic behaviour is approximately similar if we take x_A to be the average of the six M_A-O_6 bond lengths:

$$x_A \equiv \langle d\left(M_A, O\right)_6 \rangle \,. \tag{2.5.1}$$

Our "reaction coordinate" can thus be seen as a measure for the local structural distortion. This approximation loses information on the individual bond lengths, however it retains the general picture. The harmonic potential is then expressed as a function of the "breathing mode" of the MO_6 octahedron. The difference $x = x_A - x_B$ is calculated in a similar fashion:

$$x = x_A - x_B \equiv \langle d\left(M_A, O\right)_6 \rangle - \langle d\left(M_B, O\right)_6 \rangle \,. \tag{2.5.2}$$

2.5.2 Calculating the polaronic states ("POL" and "TS")

A polaron can be seen as a form of crystalline defect, and the typical way of treating defects in a periodic calculation is to include more unit cells to contain the defect, creating a supercell calculation. The size of the supercell must be chosen to minimize the amount of interaction between the defect and its images located on adjacent supercells. The procedure to localize an electron into a polaronic state is as follows. First, we take a fully relaxed intrinsic structure. Then we create the supercell and introduce an additional electron, compensated by a homogeneous positive background charge. As the initial perfect symmetry does not allow the system to localize the electron, we manually apply a small distortion on one of the TM sites before relaxing the supercell. This is done by elongating all six M-O bonds by a certain fraction, usually by 5%. This procedure is similar for hole polarons, where we instead remove an electron from the supercell and compress the bonds.

The procedure of introducing an extra charge together with a homogeneous background charge to maintain charge neutrality is a simple approximation while ensuring that the net charge does not diverge (as the system is periodic). The addition of this background charge results in a small shift in the potential, and the calculated eigenvalues are therefore also slightly shifted. This should be of no concern, as the shift is small for a single charge smeared out over a large supercell, and relative energies remain unchanged.

An issue frequently encountered in systems with localized charge is the existence of many local minima arising from the many different possible configurations. Different local orbitals (e.g. the five d orbitals) can have slightly different energies due to subtle symmetry distortions from the lattice. Inclusion of the Hubbard U parameter can further exacerbate this issue, giving rise to configurations that are separated in energy on the order of hundreds of meV. This leads to self-consistent solutions that are highly sensitive to small variations in geometry, volume, and even numerical algorithms and mixing parameters [84]. Furthermore, these solutions are not guaranteed to have the lowest possible energy of that particular system [84]. There are a few methods to systematically improve convergence to the true polaronic ground state in calculations such as those shown in Fig. 4.4 in Ch. 4. One of which is to slowly turn up the U-parameter instead of immediately applying the full U-correction, starting from a ground state calculation at $U = 0$ eV and then gradually increasing U until the desired value for U has been reached [84]. At that point, it is more likely that the self-consistent solution has been nudged to the true ground state. I found that ramping up U by 1 eV per iteration enabled us to consistently obtain accurate energies, especially for images near the transition state. For JT-distorted polarons, this might still not give us the lowest energy orbital occupancy, and in these cases we can add an additional elongation or compression of two opposite O atoms to lift the JT orbital degeneracy. In some cases it is necessary to apply this elongation or compression along all three octahedral ligand-metal-ligand axes and compare the calculated ground state energies of all the configurations to find the one that is lowest in energy.

The polaronic transition state (TS) lies in the middle of the polaronic reaction pathway between two sites. As the exact path is not known beforehand, we typically approximate this state by linearly interpolating all ionic positions, i.e. $\{q_{\mathrm{TS,linear}}\} = (\{q_{\mathrm{A}}\} + \{q_{\mathrm{B}}\})/2$ where $\{q\}$ is the set of all ionic coordinates. Most studies typically take this as their approximation to the TS, although I have found that relaxing the TS using a nudged elastic band method (NEB) [49] can improve the results by 20 - 100 meV compared to using an unrelaxed configuration that is linearly interpolated between the two end points. While NEB is typically used for ionic diffusion and chemical reactions, I find that it can also be used to calculate the transition state for an adiabatic electron transfer process. As long as we can find an adiabatic TS (if $J > 0$) that consists of a $\left(\frac{1}{2}, \frac{1}{2}\right)$ electron configuration, a force-based relaxation will remain electronically in this configuration allowing the system to structurally relax. If the TS is not adiabatic then the electronic configuration will be either $(1, 0)$ or $(0, 1)$, and an NEB force-based relaxation will quickly fall to whichever POL ground state the electron density is localized on.

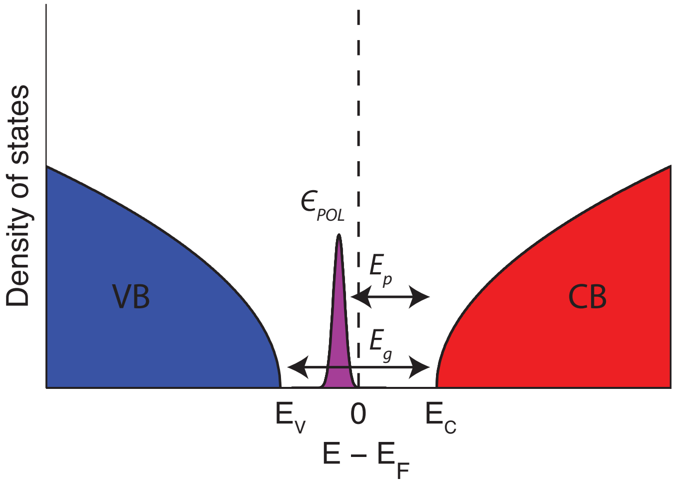

Figure 2.5: Schematic of the projected DOS for a polaronic ground state (POL). The polaron eigenstate ϵ_{POL} is projected to atomic d orbitals on the TM site it is localized on.

2.5.3 Calculating dynamics: ab initio molecular dynamics

Born-Oppenheimer molecular dynamics (AIMD) is a straightforward extension from DFT, using the Hellmann-Feynman theorem to calculate interatomic forces from the electron density. We can evolve the system over time using these forces, recalculating the electron density after each ionic step. Additionally, we can include a thermostat, i.e. connect the system to an external heat bath to apply a temperature to the system [85] and study temperature-based dynamics. In the case of polarons, we can thus study the exponential relation between hopping rate and temperature. Analysis of the MD results takes into account both properties of the polaron: a change in bond lengths Δr (see Eq. 2.5.1) together with a change in local charge $\Delta\rho$. Plotting the product of these two $(\Delta r(t) \times \Delta\rho(t))$ for each TM site over time allows us to identify the location of the polaron based on the TM site with the largest $\Delta r(t) \times \Delta\rho(t)$ value, as well as track the movement of this polaron over time. More details are shown in Section 4.3.2 of Chapter 4.

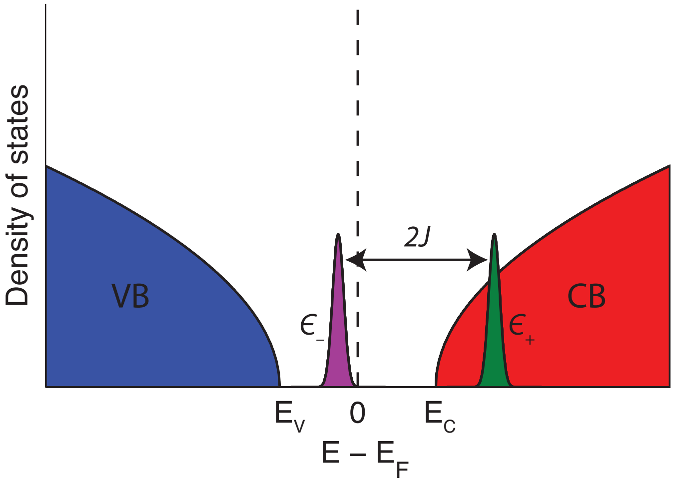

Figure 2.6: Schematic of the projected DOS for a polaronic transition state (TS). The polaron eigenstates $\epsilon_\pm$ are projected to atomic d orbitals on the two TM sites sharing the transition state.

2.5.4 *Density of states*

In this section, I briefly discuss how to calculate the relevant polaron properties from the density of states (DOS) and total energies of the POL and TS configurations. As mentioned in the introduction, the activation energy E_a follows from the total energy difference ($E_a = E_{\mathrm{TS}} - E_{\mathrm{POL}}$). The polaron formation energy, E_{form} is calculated from the total energy difference of a polaronic ground state with an intrinsic configuration where the electron is placed in an undistorted supercell to prevent it from localizing ($E_{\mathrm{form}} = E_{\mathrm{POL}} - E_{\mathrm{INT}}$). The other quantities are all obtained from the projected DOS as shown in Figs. 2.5 and 2.6, with the band gap $E_g = E_C - E_V$, the polaron state $E_p = E_C - \epsilon_{\mathrm{POL}}$, and the coupling term $2J = \epsilon_+ - \epsilon_-$. The polaronic states are projected both orbitally (onto atomic d states) and spatially (on the polaronic sites) and works best if these states are sufficiently atomic in character. If the states are more hybridized, the peaks will be less pronounced and it might be less straightforward to extract these quantities from the DOS plots.

2.6 Summary

In this Chapter, I have outlined the theoretical framework with which I will study adiabatic polaron transport with a focus on transition metal oxides in the context of novel energy materials. As polarons arise inherently from quantum mechanical interactions, we require the versatility of DFT to handle such interactions atomistically with high computational efficiency. I have also reviewed the general techniques used to calculate the desired polaronic quantities in DFT. I have developed my own interpretation for the reaction coordinate in the two-site model that is applicable to M-O_6 polarons, a rough approximation which retains the harmonic principle of the model, and included this definition in my combined charge-bond length metric to enable analysis of the MD hopping results. Additionally, I have developed a specialized toolset to induce an approximate initial polaronic ground state in a controlled fashion, improving computational efficiency of the subsequent DFT calculation.

I will now use these techniques to set up a comprehensive study of the limitations set by the DFT+U method (Chapter 3) on polaronic properties, and use the framework of the two-site hopping model to analyse the results of my calculations of polaron dynamics in $FePO_4$ (Chapter 4). As many transition metal oxides share common properties and symmetries from a structural perspective, I use elements from crystal field theory to deepen my analysis and combine these approaches to provide qualitative assessments on the properties of adiabatic polaron transport based on the specific crystal structure (Chapter 5).

3

Implications of the DFT+U method on polaron properties

3.1 Introduction

Many novel materials used in clean energy applications such as lithium ion batteries [8], photovoltaics [6], and catalysts [10] are transition metal oxides (TMO) and are known to exhibit polaronic behavior [15]. In many such TMOs, the strongly correlated interactions of the d shell electrons open a gap and localize d state conduction electrons into atomic-like orbitals. The localized spatial distribution of these electrons leads to further self trapping through interaction with the surrounding lattice, turning them into polaronic states. Typical local density approximations and generalized gradient approximations (LDA and GGA) calculations greatly underestimate these correlation effects [28, 29] leading not only to incorrect predictions for the band gap [56], but also an inability to form polarons on transition metal (TM) sites that arise from these strongly correlated interactions [30]. As such, we require additional corrections to account for these deficiencies in standard LDA/GGA to accurately study polaronic behavior in TMOs. Therefore, in order to further our understanding of such materials for existing and future energy applications, we should strive to accurately model this polaronic behavior.

Density functional theory with on-site Hubbard corrections (DFT+U) [66, 67, 68] is widely used to calculate the electronic properties of, amongst other materials, transition metal oxides where correlation plays a large role in its electronic structure.

The missing correlation effects in standard LDA/GGA are accounted for by adding an on-site Coulomb repulsion term to specific projected atomic orbitals. Typically, the value of U is either chosen to match an experimental property such as the band gap [56], or obtained from constrained LDA/GGA calculations [51, 86]. Coupled with plane wave pseudopotential formalisms, most notably the highly popular projector augmented wave (PAW) [26, 27] method, DFT+U has been highly successful in reproducing many properties of such correlated materials at minimal added computational cost. While in principle, DFT+U may add a single parameter to an otherwise *ab initio* calculation in much the same spirit as the fraction α of exact exchange in hybrid functionals [87], its local orbital dependent functional necessitates further parameters, most notably the projection radius, when transforming to on-site atomic orbitals. It has been shown before that this projection radius can significantly affect the system, especially in self-consistent calculations of U [50, 51, 52, 53, 54, 55]. Effects on localized electronic properties such as polaronic properties are less well studied.

In the PAW formalism, the DFT+U projection radius is conveniently equated to the augmentation radius (r_{PAW}) [50]. Typically, there are multiple ways to construct a PAW potential depending on how many semicore electrons to include in the valence, and it is physically justified for the PAW core radius to also vary based on the valency (more electrons in the core lead to a larger core radius). In principle, one would always use a small core PAW potential with semicore electrons included in the valence for higher precision, although this incurs a computational cost from the additional electrons and larger basis set. However, the DFT+U projection radius changes as well, impacting electronic properties that are dependent on the U-term. This makes the choice of U more ambiguous [50, 51, 52, 53, 54, 55].

In this work, we investigate the effects of DFT+U projection radius and semicore electrons in a set of energy materials that are known to exhibit polaronic behavior and focus on polaronic properties in these materials as illustrated in Fig. 3.1. The

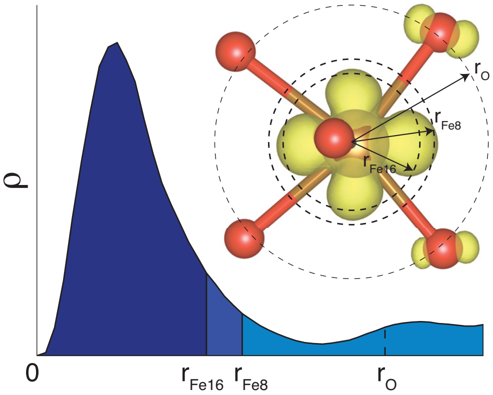

Figure 3.1: Schematic of the radial charge density distribution (ρ) of a polaronic state taken from Fe_2O_3, centered at the TM site on which the polaron is localized at. r_O is the average metal-oxygen bond length, while in this example, r_{Fe8} and r_{Fe16} correspond to two different cutoff radii (r_{PAW}) of a large core Fe potential ($r_{\mathrm{PAW}} = 2.3\ a_0$) with 8 valence electrons, and a small core Fe potential ($r_{\mathrm{PAW}} = 1.9\ a_0$) with 16 valence electrons, respectively. These are also drawn approximately on the MO_6 octahedral complex, which is cut out from the Fe_2O_3 solid. Other materials show similar behavior.

materials studied are rutile TiO_2, Fe_2O_3 (hematite), $LiFePO_4$ and its delithiated form $FePO_4$, and spinel MnO_2. TiO_2 and Fe_2O_3 are materials considered for photocatalytic applications [6, 38], while Li_xFePO_4 and $Li_xMn_2O_4$ are amongst the current and next generations of lithium ion batteries [8, 88].

My DFT+U work on $FePO_4$ in Chapter 4 will show that the choice of PAW potential significantly affects the calculated polaron activation energy [2]. In this chapter, we expand on this work by not only studying additional materials, but also by including additional comparative HSE06 calculations [29, 73, 87]. We can separate the contributions from the projection radius and semicore electrons by comparing the results of both DFT+U and HSE06 methods, as the exact exchange is calculated everywhere in HSE06 calculations as opposed to the local U-term which acts only within the projection radius in DFT+U calculations. By conducting such a comprehensive study, we hope to establish a precedent on how to approach polaronic calculations in such a way that consistent results and predictions become more attainable.

3.2 Theory

Naturally, the main question of any DFT+U implementation is determining a value of U that is appropriate for the particular system being studied. In theory, this is a single parameter (two if the screened exchange term J is included in higher order implementations [66, 67, 68]); but as shown previously, the implementation of a local orbital dependent functional necessitates further parameters that are mostly numerical in nature. In our case, this additional parameter would be the projection radius r_{PAW}. As shown before in previous studies [50, 51, 52, 53, 54, 55], the dependence on other parameters leads to ambiguities when utilizing constrained DFT techniques [51, 86] to self-consistently calculate a value for U, as the resulting value was shown to vary greatly depending on both the projection radius and the basis set used. These ambiguities therefore lend more credence to the contrasting viewpoint of U as an empirical parameter that we can use to fit experimentally measured properties [44, 52, 53, 56], most commonly the band gap. Apart from the band gap, there are of course many other quantities that we can fit U on, with examples being unit cell volumes/bulk moduli, reaction enthalpies, and polaronic properties such as the location of the polaronic gap state within the band gap.

Hybrid functionals [73, 87] could be seen as more versatile and consistent as the fraction of exact exchange α is less system dependent and applies to all orbitals as opposed to DFT+U which only treats a selected on-site orbital. This allows for treatment of correlation effects in orbitals that are more hybridized and do not project adequately onto pure atomic states [89] as well as an "occupancy agnostic" treatment for systems that are more CT-like such as TiO_2 [90]. This is in contrast to DFT+U, where the effect of the functional and hence the value for U depends on the occupancy of the on-site orbital [51]. These advantages are at the expense of a one to two orders of magnitude increase in computational effort required.

Analogous to the DFT+U method, hybrid functionals rely on a single parameter α

which is the fraction of exact exchange that is mixed together with the LSDA/GGA semilocal exchange energy. The effect on strongly correlated materials can be seen as an effective "U-term" acting indiscriminately on all orbitals, both local and non-local [87]. On one hand this can be seen as more elegant and closer to the spirit of *ab initio* calculations, requiring a single parameter that is typically set at a system independent value (typically 25% for the PBE0 functional [29] and its screened variant HSE06 [73]), but on the other hand it is not a perfect functional, and there are systems where the higher tunability of DFT+U leads to results that are in better agreement with experiments [45, 91], an example of which (hematite) will be further investigated in this study. A link between DFT+U and hybrid functionals, as the projected on-site part of the exact exchange has been shown earlier [75]. In this work, we mainly utilize the HSE06 functional as a means to circumvent the dependence on r_{PAW} as both local and non-local exact exchange are treated equally, so we can study the influence of semicore electrons as an independent variable. Assuming that these effects are comparable in DFT+U and subtracting them from our DFT+U results, we can then in turn study solely the effects of changing r_{PAW} in DFT+U.

3.3 Method

All calculations were done in the Vienna Ab-initio Software Package (VASP) [92, 93, 94, 95] using the PBE-GGA semilocal functional [96, 97] within the PAW formalism [26, 27]. We utilized this package for our study because its PAW potentials are generally the most utilized by the *ab initio* strongly correlated electronic structure community. However, the general trends explored should be applicable to all DFT+U implementations. Correlations were treated with both DFT+U [50, 67, 98] and HSE06 [73, 87] methods. The set of PAW potentials [27] studied was provided and included within VASP. All ionic positions were relaxed until interatomic forces were smaller than 0.005 eV / Å for volume and intrinsic structure calculations, and 0.01 eV / Å for polaron supercell calculations. For structural relaxations, the PAW potential with the smallest radius was used except for $LiFePO_4$ (see Table 3.1), in which case the large core Fe potential was used due to issues described in the $LiFePO_4$ results section. We calculated separate sets of structures for both DFT+U and HSE06. Typically, an HSE06 relaxation leads to approximately 5% smaller volumes and therefore $2-3\%$ shorter bond lengths compared to a DFT+U relaxation, and these structural discrepancies lead to errors in the calculated properties of around 50-100 meV when using a DFT+U structure in an HSE06 calculation and vice versa.

We performed polaron calculations in supercells deemed large enough to contain the defect, and all polaron hopping barriers were calculated by relaxing the transition state with the CI-NEB method [49]. A Gaussian smearing of 0.02 eV was used in all cases, but increased to 0.05 eV for displaying density of states (DOS) results. For rutile TiO_2, a $2 \times 2 \times 3$ supercell (24 formula units) was used for the polaron calculations with a $2 \times 2 \times 2$ Monkhorst-Pack k-point scheme. For Fe_2O_3, we used a supercell consisting of $2 \times 2 \times 1$ hexagonal unit cells (24 formula units), with only Γ-point sampling in the reciprocal space. A $1 \times 2 \times 2$ supercell (16 formula units) with Γ-point sampling was used for $FePO_4$ and $LiFePO_4$, and for spinel MnO_2 the cubic cell with 16 formula units was used with a $2 \times 2 \times 2$ Monkhorst-Pack k-point scheme. Values used for U_{eff} are 4.2 eV for TiO_2 [44], 4.3 eV for FP/LFP [30] and Fe_2O_3 [45], and 4.5 eV for MnO_2 [46]. These values were calculated self-consistently for FP/LFP, Fe_2O_3, and MnO_2 [56], whereas the value for TiO_2 was fitted to reproduce the experimental band gap [44].

After relaxing all the required structures, we then calculated the properties with a set of PAW potentials supplied by VASP [27], of which the valencies and augmentation radii are listed in Table 3.1. These include the standard potentials without semicore electrons (labeled "X"), potentials with $3p$ electrons (labeled "X_pv"), and potentials with $3s$ and $3p$ electrons (labeled "X_sv"). For Ti, we included an additional hard potential ("Ti_h") with an even smaller core radius. We also included the latest (2015) PAW potentials that are optimized for GW calculations (labeled "X_sv_GW") but are also seen as generally more accurate [99]. Results with these potentials might deviate slightly from the expected trends due to their different construction as they have more projectors and empty valence states [99].

The properties that we have studied are the band gap E_g, the polaron gap state E_p, the polaron formation energy E_{form}, and the bulk polaron hopping barrier (activation energy) E_a. We define the band gap $E_g = E_C - E_V$ as the difference between the conduction band minimum (CBM) and valence band maximum (VBM). We take the polaron gap state energy E_p relative to the CBM. The formation energy is calculated as the difference between the localized polaronic ground state and the initial, undistorted state $E_{\text{form}} = E_{\text{POL}} - E_{\text{INT}}$, and the activation energy E_a is the hopping barrier which is the difference between the transition state (TS) and ground state total energies $E_a = E_{\text{TS}} - E_{\text{POL}}$.

For additional comparison, we also performed polaron hopping barrier E_a calculations with the plane-wave DFT code Abinit [100, 101], using the same structures and parameters as in the VASP calculations. The DFT+U projection scheme in Abinit [71] differs slightly from the one used in VASP [50], leading to different calculated trends. For further details we refer to the appendix in Sec. A.

3.4 Results

In this section we list our computed properties for each material (rutile TiO_2, Fe_2O_3, (Li)$FePO_4$, and spinel MnO_2) in its own subsection, comparing them to earlier calculations and experimental measurements if available. We also provide extensive analysis on the calculated trends in these materials, followed by a more in-depth analysis of the projection radius in Sec. 3.5. We then recap our analysis and provide a general assessment of these trends in Sec. 3.6. Full datasets of our calculations are included in the appendix in Sec. A.

	Z_{val}	r_{PAW} (a.u.)
Ti	4	2.8
Ti_pv	10	2.5
Ti_sv	12	2.3
Ti_sv_GW	12	2.0
Ti_h	12	1.9
Mn	7	2.3
Mn_pv	13	2.3
Mn_sv_GW	15	2.0
Mn_sv	15	1.95
Fe	8	2.3
Fe_pv	14	2.2
Fe_sv_GW	16	2.0
Fe_sv	16	1.9

Table 3.1: List of the potentials used in this study with their different valencies and PAW augmentation radii r_{PAW}. Other differences in PAW construction which are most notably between GW and non-GW potentials are not shown here.

3.4.1 TiO_2

Titanium dioxide in its rutile form (Fig. 3.2) has a measured band gap of 3 eV [102]. Further experimental results [40] indicate a polaronic surface state in the band gap that is approximately 0.7 ± 0.1 eV below the CBM. While we cannot directly relate a surface state to one calculated in the bulk material, they still arise from the same physical origin of strong d-orbital correlations and we should be able to connect the two qualitatively.

From a chemical point of view, the Ti atoms are stripped of all their valence electrons leaving them in a d^0 state. This leads to TiO_2 being a strong CT insulator, with the valence band dominated by completely filled O $2p$ states, and the conduction band having Ti $3d$ character as shown in the projected DOS plot in Fig. 3.3. From this alone we can already argue that the DFT+U formalism should be insufficient as the U-term acts upon localized electrons with atomic-like d-character, of which there are formally none in this material. Its resulting effect on the band gap should therefore be small, as has been calculated in previous DFT+U works [90, 103]. As the

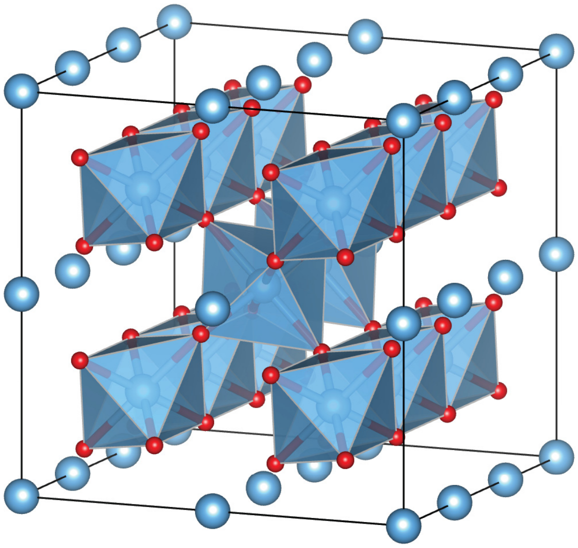

Figure 3.2: Structure of rutile TiO_2.

projected $3d$ occupations inside the Ti spheres are still non-zero due to hybridization and non-orthogonality of other states entering the sphere (and can even be larger than 2 for large spheres [103]), the orbital dependent U-term will still act on these unphysical non-zero occupations, and this could lead to uncontrollable results [53]. We therefore expect that a hybrid functional such as HSE06 would fare better here as it is independent of both orbitals and their occupancies.

Fig. 3.3 shows the projected DOS of TiO_2, with one additional electron localized in a polaronic state. Calculations with DFT+U and HSE06 are qualitatively very similar, so we only show the DFT+U calculations here. The valence band consists entirely of p states, while the conduction band is fully d-like. The band gap E_g is defined as the energy difference between the lowest unoccupied state (CBM) and the highest occupied state (VBM), and the polaronic state E_p is defined relative to the CBM. According to the PDOS, this polaronic state is almost entirely of d-orbital character, which is also confirmed by the radial charge density plot in the inset of Fig. 3.3, showing behavior that is similar to an atomic $3d$ orbital.

Fig. 3.4 shows the band gap and polaron properties calculated with both DFT+U

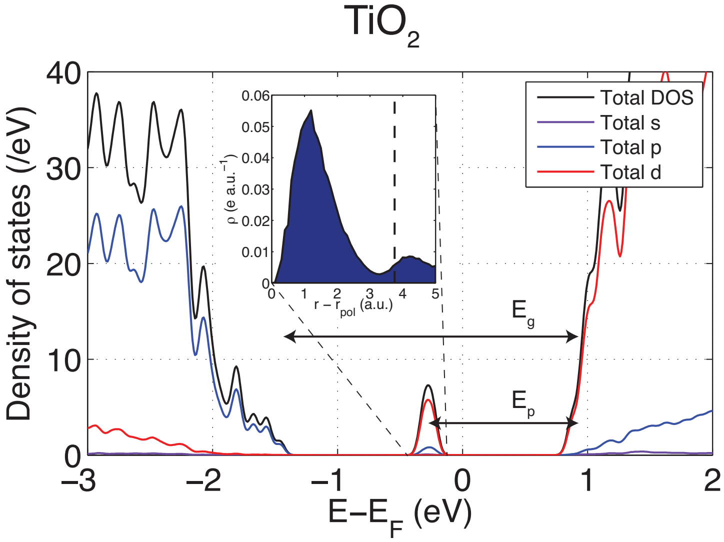

Figure 3.3: TiO_2 orbital projected DOS of the polaronic ground state. Inset: real space radial charge distribution of the polaronic state. This particular example was calculated with DFT+U and the "Ti_sv" potential.

($U = 4.2$ eV [44]) and HSE06 ($\alpha = 0.25$) methods while varying the Ti PAW potential. From the HSE06 plot in Fig. 3.4a which does not depend on projection radius, we see that the band gap incurs a slight increase with an increase in valence electrons (4 for $r_{PAW} = 2.8$, 10 for $r_{PAW} = 2.5$, and 12 for 4 for $r_{PAW} \leq 2.3$). The different r_{PAW} of the three 12 electron potentials do not seem to affect the HSE06 results in any significant way. In comparison, the DFT+U plot in Fig. 3.4a shows a smaller increase of the gap with an increase in valence electrons, peaking at $r_{PAW} = 2.3$ and then decreasing as we further decrease r_{PAW}. We can see that increasing the number of valence electrons has an effect similar to the HSE06 results, while there is an additional superimposed contribution from the different DFT+U projections, however it is not as drastic as the theory would suggest. We attribute this to the valence band being entirely of O $2p$ character, where the splitting from the DFT+U $3d$ projection has little effect. Furthermore, the increase in the number of semicore electrons leads to a slight increase of the gap, and the two effects somewhat cancel each other out. However, the position of the polaron state is influenced dramatically as seen in Fig. 3.4b. As r_{PAW} decreases, the distance between the polaron state and the CBM becomes smaller and smaller

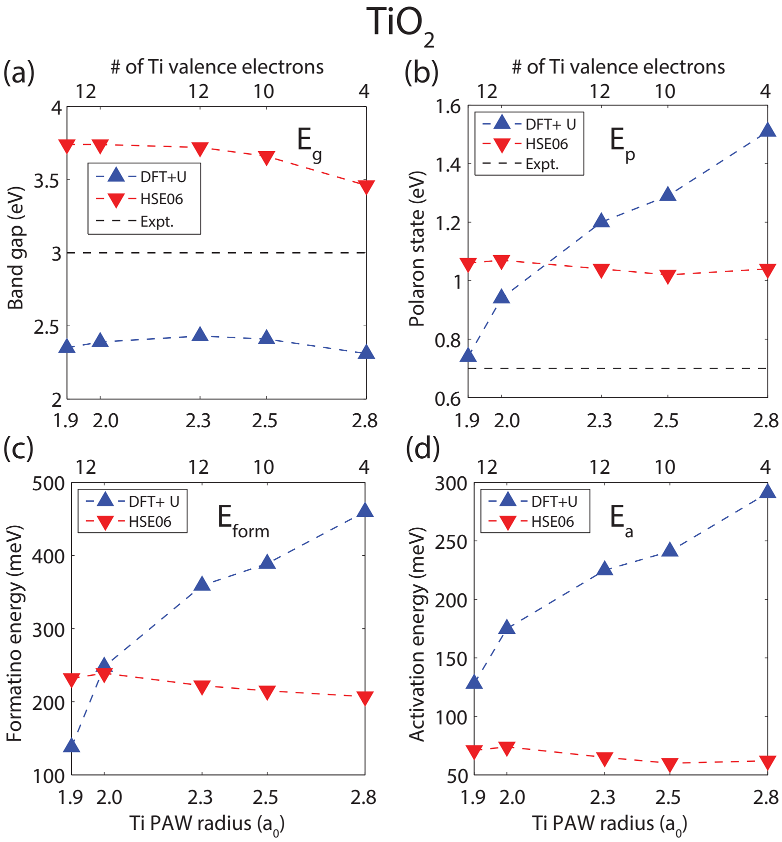

Figure 3.4: Calculated electronic properties of TiO_2 with DFT+U and HSE06 as function of different PAW potentials. (a) band gap E_g, (b) polaronic gap state E_p, (c) formation energy E_{form}, (d) polaronic hopping barrier E_a.

for DFT+U, while the HSE06 results are insensitive to the choice of r_{PAW}. This can be attributed to the DFT+U projection of the polaron state which is almost entirely of Ti 3d character and therefore is highly sensitive to the projection radius. Similar trends can be seen from the formation and activation energies in Fig. 3.4c and 3.4d, with the DFT+U results being highly sensitive to r_{PAW} and the HSE06 results being affected mostly by the difference in valence electrons, but relatively less so. From the DFT+U results in Fig. 3.4, we can see a relationship between the polaronic properties (formation and activation energies) and the position of the polaron within the band gap (vs. CBM). Qualitatively this makes sense, as the distance to the conduction band will determine how strong the self-trapping and hopping energies are.

For TiO_2, it seems that HSE06 results are much more consistent as function of varying PAW potential, and that there is a wide variance in our DFT+U results depending mainly on which projection radius is used. Combined with the unphysical behavior of DFT+U in d^0 materials, we conclude that HSE06 obtains more consistent results for TiO_2. Finally, comparing to experimental measurements, the HSE06 results for the band gap (expt. 3 eV) and polaron state (expt. 0.7 eV from CBM) seem to be about 0.6 eV and 0.3 eV off, respectively. In order to obtain a better quantitative prediction of the polaron hopping barrier, it seems plausible to slightly reduce the mixing factor α to better match the band gap and polaron state with experimental results for TiO_2, as the value of α was originally tuned to reproduce the energies of molecular systems [74], and might not be universally applicable to all solids.

3.4.2 Fe_2O_3 (Hematite)

For hematite (Fig. 3.5), experimental data is available for three relevant characteristics, with the band gap measured at 2 eV [104], the polaron state with respect to the CBM at 0.7 eV [48], and the polaronic activation energy at 120 meV [48]. Additionally, the activation energy has been calculated at 130-150 meV in a previous DFT+U study [45], showing close correspondence to the experimental value. This

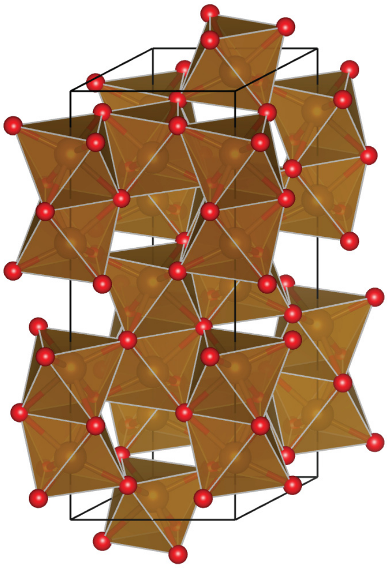

Figure 3.5: Structure of Fe_2O_3, also known as hematite.

makes hematite an ideal case to focus our computational study on.

Fig. 3.6 shows the projected DOS as well as the real space radial charge density plot of the polaronic state. As Fe^{3+} is in a high spin d^5 state, adding an extra electron will send it to the minority spin channel turning it into d^6 Fe^{2+}. The electronic properties in Fig. 3.7 show that DFT+U calculations with all potentials reproduce the band gap quite well, although the polaronic properties vary wildly per potential. These trends are quite comparable to the situation in TiO_2. The potential that achieves the best comparison of the activation barrier to experiment is the large core potential (r_{PAW} = 2.3 a_0) with 8 valence electrons largely due to its larger projection radius, although the $r_{\mathrm{PAW}} = 2.0$ a_0 potential with 16 valence electrons comes closest to reproducing the polaron gap state.

In contrast to our TiO_2 results, the HSE06 method does not reproduce experimental values as well as DFT+U. While the results are more consistent between different potentials and show expected trends with respect to semicore electrons, the standard mixing fraction of 25% overestimates the band gap to 3.5 eV in all cases as shown in Fig. 3.7a. When setting α to 12% to obtain a better band gap compared

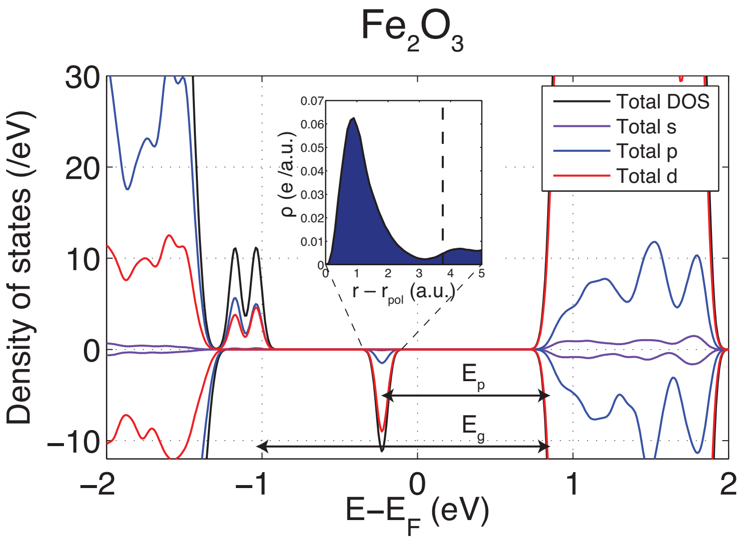

Figure 3.6: Fe_2O_3 orbital projected DOS of the polaronic ground state. Inset: real space radial charge distribution of the polaronic state. This particular example was calculated with DFT+U and the “Fe” potential.

with experiment [91], we were unable to localize a polaron in Fe_2O_3, contrary to experimental evidence. Using the standard $\alpha = 25\%$ for polaron calculations which does allow polaron formation, we then obtained very low activation energies of 15 meV at $r_{\text{PAW}} = 1.9\ a_0$, going down to almost 0 meV for the $r_{\text{PAW}} = 2.3\ a_0$ potential. Therefore, it seems that for this material, DFT+U reproduces experimental results better, although careful attention is required concerning the projection radius.

3.4.3 *$FePO_4$ and $LiFePO_4$ (LFP)*

As it is challenging to synthesize a fully delithiated sample of $LiFePO_4$ (Fig. 3.8), we will compare our results to a previous computational study [30, 89], reproducing their results with the large core Fe potential ($r_{\text{PAW}} = 2.3\ a_0$) while adding more insight by including the other potentials as well as the HSE06 method. Fig. 3.10 shows the results of this study, with all results following the trends as noted before; HSE06 results being dependent on mostly the number of electrons and DFT+U results showing a mostly downward trend with decreasing radius. The two main differences are that HSE06 calculations lead to a much larger band gap and a smaller polaron formation energy.

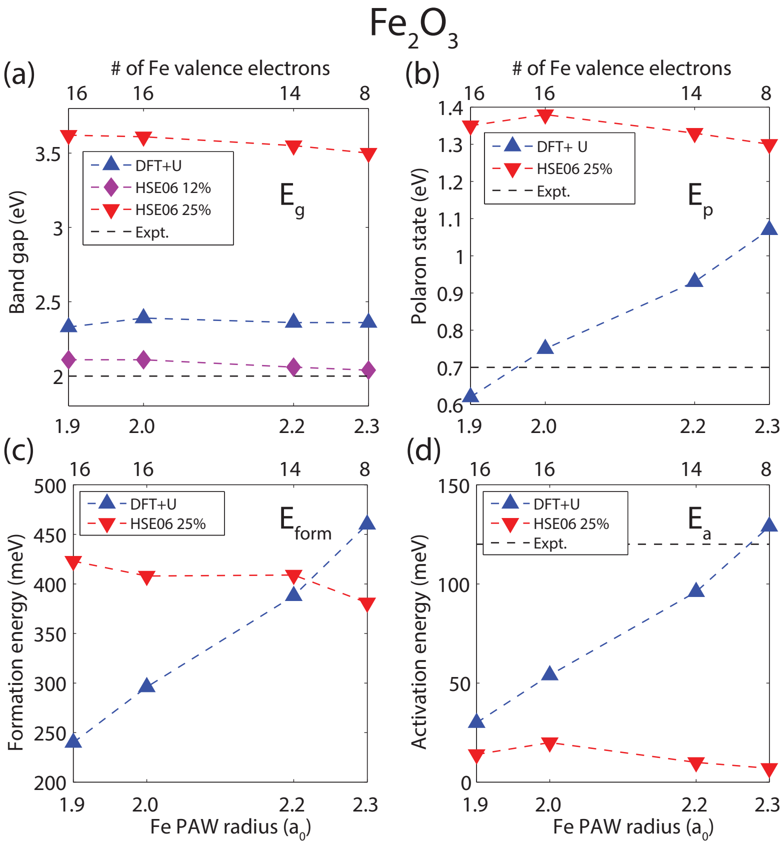

Figure 3.7: Calculated electronic properties of Fe_2O_3 with DFT+U and HSE06 using different PAW potentials. (a) band gap E_g, (b) polaronic gap state E_p, (c) formation energy E_{form}, (d) polaronic hopping barrier E_a.

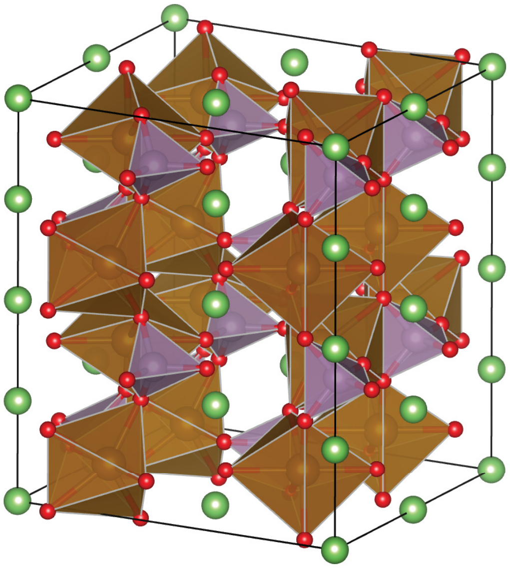

Figure 3.8: Structure of $LiFePO_4$. $FePO_4$ has the same structure without the intercalated Li atoms.

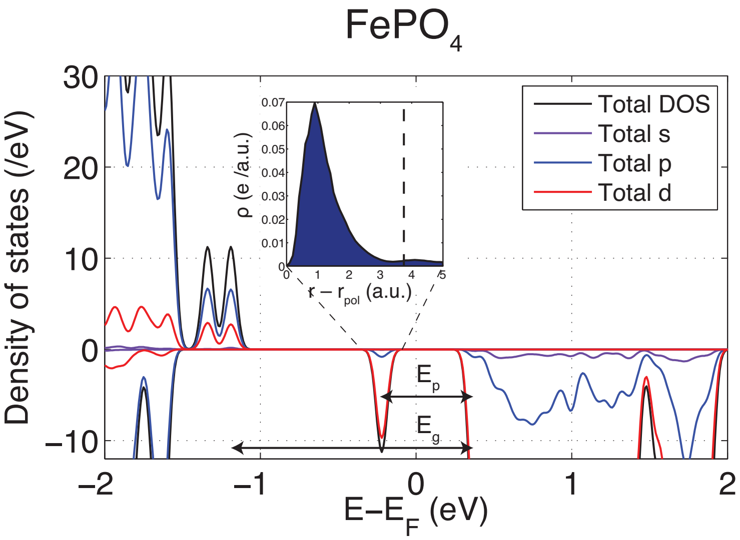

Figure 3.9: $FePO_4$ orbital projected DOS of the polaronic ground state. Inset: real space radial charge distribution of the polaronic state. This particular example was calculated with DFT+U and the "Fe" potential.

For $LiFePO_4$ in its fully lithiated phase, the experimental band gap has been measured at ~ 4 eV [56], while not much polaron information is available as the mobile Li^+ ions seem to form the rate limiting factor for conductivity measurements with their significantly higher diffusion barriers [30, 105, 106]. From the projected DOS in Fig. 3.11 we can see a significant qualitative difference between this material and the other materials studied. The Fe^{2+} peak is the highest occupied state, but it is localized and separated from the usual delocalized O 2p / Fe 3d hybridized valence band present in $FePO_4$ as shown in Fig. 3.9, making this material a true Mott-Hubbard insulator. From a $FePO_4$ perspective, $LiFePO_4$ could also be described as being fully saturated with polarons that are charge transferred from the Li^+ ions. We therefore have two definitions of a band gap in this material, depending on how we define this Fe^{2+} state. One definition is the delocalized CBM - delocalized VBM (labeled "CB - VB" in Fig. 3.12a), and the second one will be the traditional CBM - zero temperature E_F definition (labeled as "C - 2+" in Fig. 3.12a). We can see how the DFT+U projection comes into play for these two definitions in Fig. 3.12, with the "CB - VB" gap near constant and the traditional "CB - 2+" gap being strongly

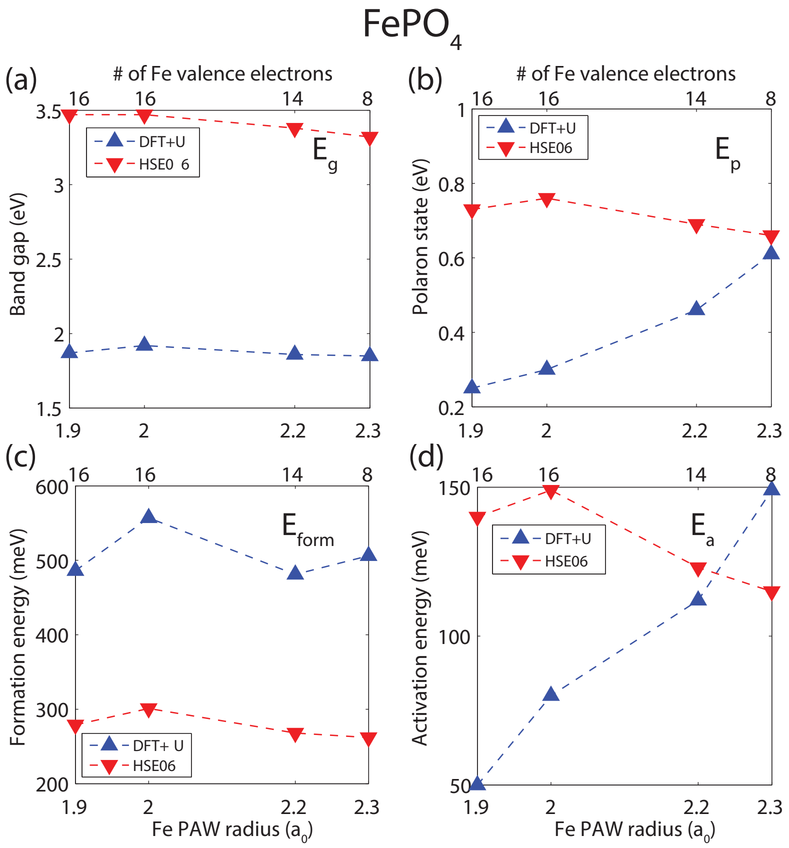

Figure 3.10: Calculated electronic properties of $FePO_4$ with DFT+U and HSE06 using different PAW potentials. (a) band gap E_g, (b) polaronic gap state E_p, (c) formation energy E_{form}, (d) polaronic hopping barrier E_a.

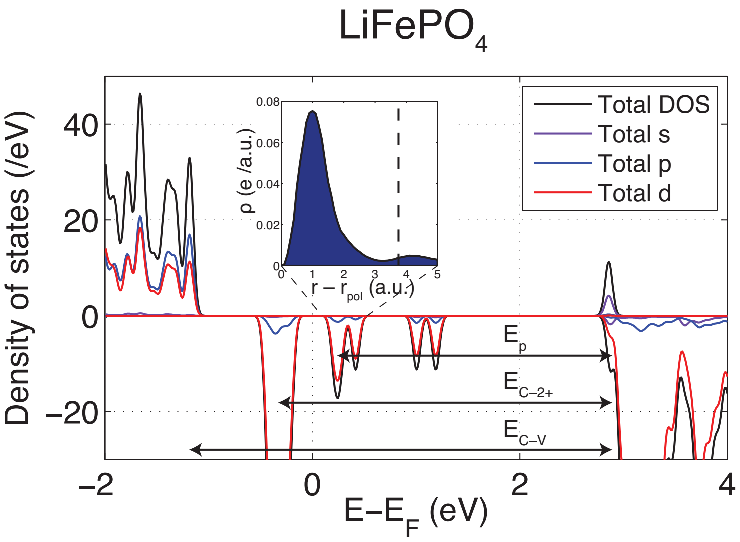

Figure 3.11: $LiFePO_4$ orbital projected DOS of the polaronic ground state. Inset: real space radial charge distribution of the polaronic state. This particular example was calculated with DFT+U and the "Fe" potential.

dependent on the potential used. This further clarifies our definition of the "2+" state as being polaron-like, as it is a pure Mott-Hubbard state and therefore highly sensitive to the projection radius. Furthermore, the empty hole polaron state above the Fermi energy retains the same position from both the CBM and the delocalized VBM. Thus, the only state that moves when changing the DFT+U projection radius is the 2+ state. For HSE06, both gaps remain unchanged which again shows that the polaron state is preserved in HSE regardless of which PAW radius we choose as shown in Fig. 3.12a. Here once again, HSE produces much more consistent gap states and barriers solely due to the fact that it is not dependent on a projection radius, although it again consistently calculates much higher band gaps.

The $FePO_4$ results are quite in line with the other materials. While $LiFePO_4$ is strongly Mott-Hubbard like, subsequently leading to stronger r_{PAW} effects in even the DFT+U calculated band gap. Also uniquely for $LiFePO_4$, we were unable to localize a hole polaron in DFT+U with the 16-electron small core potential ($r_{\mathrm{PAW}} = 1.9\ a_0$), and as such all structural calculations were done with the 8-electron, $r_{\mathrm{PAW}} = 2.3\ a_0$ potential. This can be clearly explained from the formation energy in Fig. 3.12, which

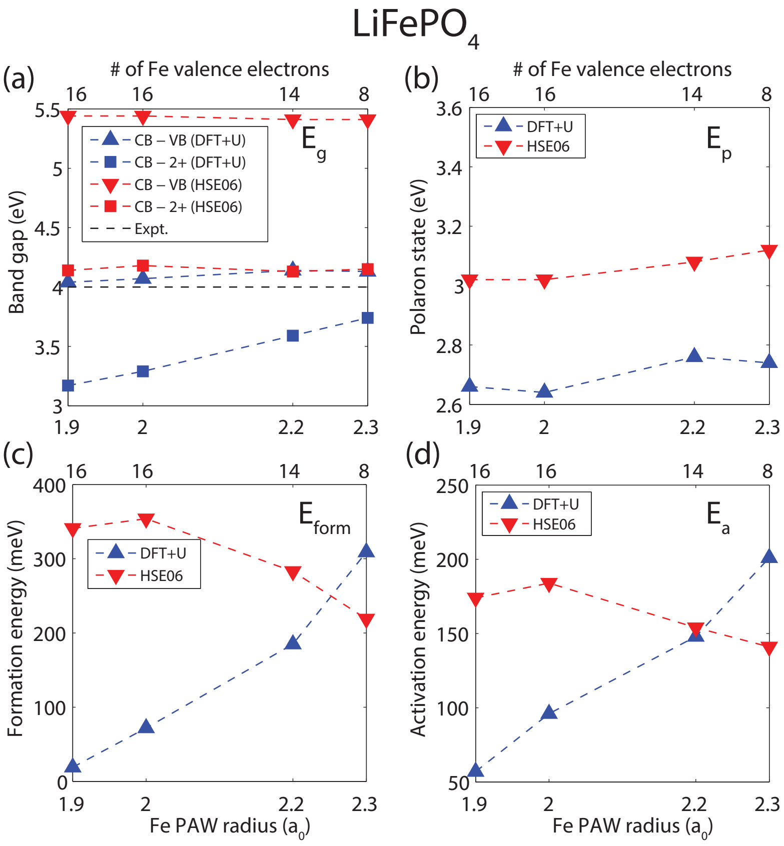

Figure 3.12: Calculated electronic properties of $LiFePO_4$ with DFT+U and HSE06 using different PAW potentials. (a) band gap E_g, (b) polaronic gap state E_p, (c) formation energy E_{form}, (d) polaronic hopping barrier E_a.

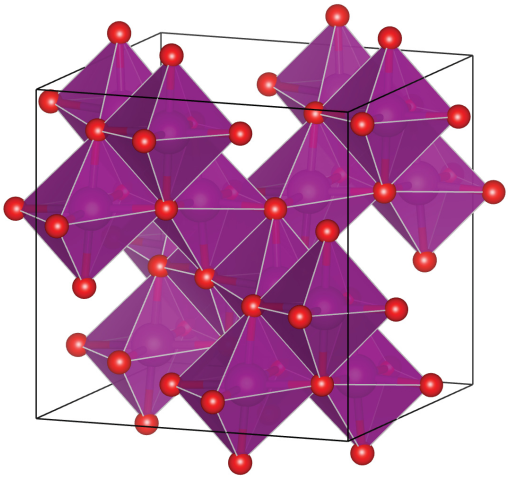

Figure 3.13: Structure of spinel MnO_2.

becomes nearly zero (20 meV) as well as lower than the activation barrier as r_{PAW} is lowered. This 20 meV formation energy would lead to thermal excitations being able to easily delocalize the state, as well as band conduction being favored over hopping conduction as it would cost less energy to excite the electron into the conduction band. This shows once more the importance of setting a realistic projection radius, especially for calculations of polaron properties.

3.4.4 MnO_2

Band gap measurements have been done on $LiMn_2O_4$, which has half a Li for each formula unit of MnO_2 (Fig. 3.13). These additional Li atoms add electrons which relax further into polaronic states. Therefore, the measured *d*-*d* band gap of 1.2 eV [107] would correspond to the polaron gap state E_p as opposed to the Mn 3*d* - O 2*p* gap, which was measured to be around 3 eV [108] – this study also measured additional *d*-*d* transition energies of 1.63 eV and 2.00 eV. DFT+U calculations have been performed earlier [46] and have resulted in a calculated barrier of 0.22 eV for free polarons.

Fig. 3.14 shows the projected DOS for MnO_2 and its polaron real space radial

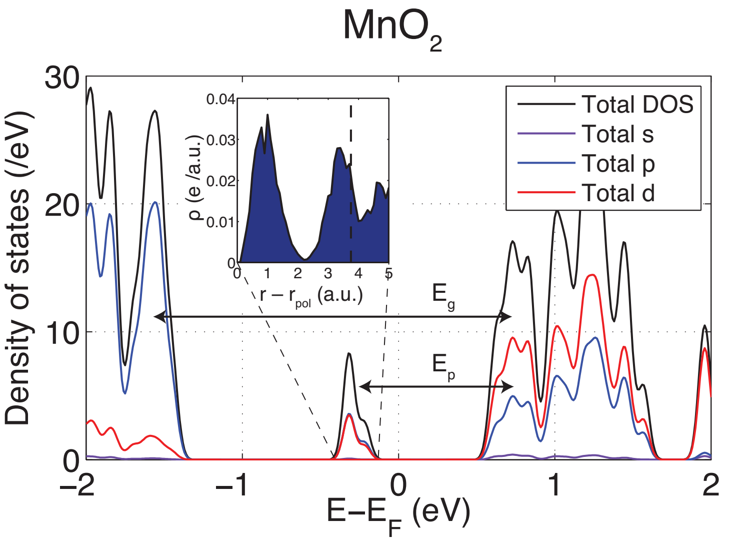

Figure 3.14: MnO$_2$ orbital projected DOS of the polaronic ground state. Inset: real space radial charge distribution of the polaronic state. This particular example was calculated with DFT+U and the "Mn_pv" potential.

density calculated in DFT+U. In contrast to the other materials studied, the MnO$_2$ projected DOS shows significant hybridization of the polaronic state, which is of approximately half p and half d character. This can also be clearly inferred from the inset, which shows a real space density that is shared between the Mn site and the O atoms, with a minimum at around 2.2 a_0. The physical implications of a more hybridized polaron state is that it is less sensitive to DFT+U parameters as it projects far less onto purely atomic d states. Additionally, the increased hybridization could be more general to other Mn-O compounds, where for example in MnPO$_4$ it was shown that DFT+U could not localize a polaron at all due to the increased hybridization [89].

The electronic properties of MnO$_2$ are shown in Fig. 3.15. At first glance, there are only quantitative differences between DFT+U and HSE06 here, with HSE06 calculations resulting in higher energies over all projection radii. Both the 7-electron ($3d^5 4s^2$) and 13-electron ($3p^6 3d^5 4s^2$) potential of Mn have the same radius of 2.3 au, allowing us to do a direct study of $3p$ semicore effects in Mn while keeping r_{PAW} the same. Those results are similar to the other materials, with more electrons leading

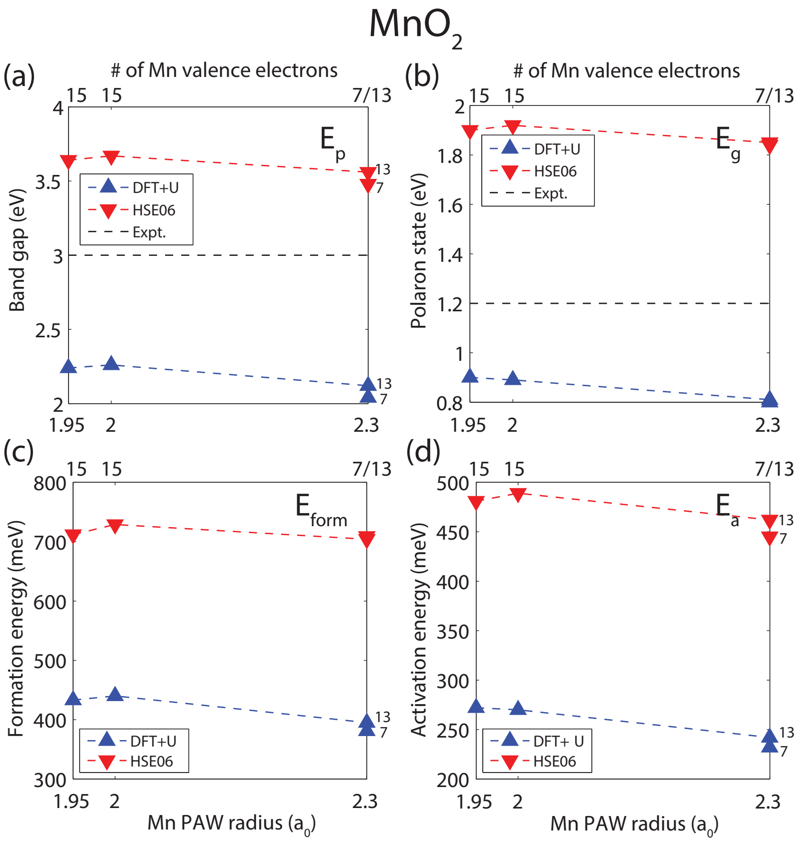

Figure 3.15: Calculated electronic properties of MnO$_2$ with DFT+U and HSE06 using different PAW potentials. (a) band gap E_g, (b) polaronic gap state E_p, (c) formation energy E_{form}, (d) polaronic hopping barrier E_a.

to slightly higher energies. However, the DFT+U results are in contrast to the other materials, showing little effect of $\mathrm{r}_{\mathrm{PAW}}$ and being qualitatively similar to the HSE06 results. The calculated activation energies E_a in Fig. 3.15d follow the same trend as the formation energies E_{form} and gap state energies E_p, showing relatively little dependence on r_{PAW}.

Thus, for spinel-type $\mathrm{MnO_2}$, DFT+U calculated properties depend very little on r_{PAW}. This is explained through two physical properties. Qualitatively, as shown in the projected DOS in Fig. 3.14, the $\mathrm{MnO_2}$ polaron state is strongly p-d hybridized and is therefore relatively insensitive to $\mathrm{r}_{\mathrm{PAW}}$ in DFT+U, as there will be little projection onto atomic-like d states regardless of projection radius. Also, we can look at the real space density in Fig. 3.14 which drops to almost zero at around 2.2 a_0. This means that if we vary the projection radius between 1.95 and 2.3 a_0, the integrated value would likely vary little even if the state were of pure atomic 3d character.

3.5 DFT+U projection analysis

To study the effects arising from changing the projection radius, we plot the real space charge distribution of a polaronic state centered radially on its transition metal site in Fig. 3.16, taking $\mathrm{Fe_2O_3}$ as our case material. Polaron charge densities in the other materials are very similar as seen in the insets of the separate DOS figures so our analysis here will be general, with the exception of $\mathrm{MnO_2}$ which is treated separately due to its hybridization. The two black dashed lines represent the projection radius of the smallest core ($r_{\mathrm{PAW}} = 1.9\ a_0$) and the largest core ($r_{\mathrm{PAW}} = 2.3\ a_0$) PAW potential. The integrated charge density with $r_{\mathrm{PAW}} = 1.9\ a_0$ is 0.6698 compared to 0.7145 for $r_{\mathrm{PAW}} = 2.3\ a_0$, leading to a difference in projection of approximately 0.05 electrons. We can see that both radii are approximate as they are both relatively far up the tail and neither projection encompasses even 90% of the electron density. For half an electron on a TM site in the $\mathrm{Fe_2O_3}$ "TS" state, these numbers are 0.3481 and 0.3749 respectively, a difference of approximately 0.025 electrons.

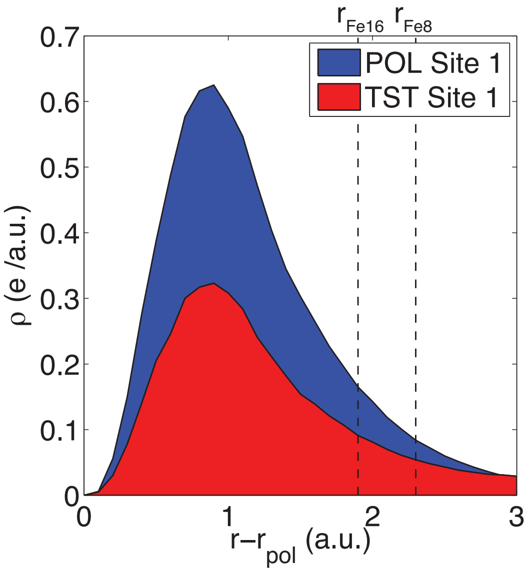

Figure 3.16: Real space radial charge distribution around a polaronic Fe site in Fe_2O_3. This particular calculation was done in DFT+U with the "Fe" potential. The blue curve and area corresponds to the polaronic ground state ("POL"). The red curve and area corresponds to the transition state ("TS"), where half of the electron density is centered on this site and the other half is centered on a neighboring site. The PAW radii shown correspond to the large ($r_{\mathrm{PAW}} = 2.3a_0$, 8 valence electrons) and small core Fe ($r_{\mathrm{PAW}} = 1.9a_0$, 16 valence electrons) potentials.

The magnitude of these differences directly influences the energy term of Eq. (2.2.14) and affects the *d*-*d* splitting as seen in the differences of the locations of the polaron gap states for all the materials studied including Fe_2O_3, as well as the CBM - VBM gap in $LiFePO_4$. For the formation and activation energies, the effect is more subtle as it relies on an energy difference between the U-term energy contributions. However, in both cases this can be traced back to the quadratic dependence on the occupancy of the U-term. We first rewrite Eq. (2.2.14) as a sum of on-site U-term energy contributions:

$$E_{\mathrm{DFT+U}} = E_{\mathrm{DFT}} + E^U \equiv E_{\mathrm{DFT}} + \sum_t E_t^U(N), \tag{3.5.1}$$

where the sum goes over all sites t, and N is the (projected) occupancy of local electrons at site t. The activation energy $E_a = E_{\mathrm{TS}} - E_{\mathrm{POL}}$ is defined as the total energy difference between the transition state configuration (“TS”) where the electron is shared between two neighboring sites (labeled t^A and t^B) and the polaronic ground state configuration (“POL”) where the electron is localized on one site (labeled t^A) only. Focusing on the projection-dependent U-term contributions and separating out the other terms (that we assume depend negligibly on the projection), we rewrite E_a as:

$$E_a = E_{\mathrm{TS}} - E_{\mathrm{POL}} = E_{\mathrm{TS}}^U - E_{\mathrm{POL}}^U + \Delta E_{\mathrm{other}}, \tag{3.5.2}$$

$$E_{\mathrm{POL}}^U = E_{t^A}^U(N+1) + \sum_{t \neq t^A} E_t^U(N), \tag{3.5.3}$$

$$E_{\mathrm{TS}}^U = E_{t^A}^U(N+1/2) + E_{t^B}^U(N+1/2) + \sum_{t \neq t^A, t^B} E_t^U(N). \tag{3.5.4}$$

To first order $E_{t^A}^U(N+1/2) = E_{t^B}^U(N+1/2) = E_t^U(N+1/2)$ and assuming that, in a linear approximation, we can write $E_t^U(N+x) \approx E_t^U(N) + E_t^U(x)$, the relevant U-term energy difference becomes

$$E_a^U \approx 2E_t^U(1e/2) - E_t^U(1e), \tag{3.5.5}$$

as all other on-site differences within $E^U_{t,\mathrm{TS}}(N) - E^U_{t,\mathrm{POL}}(N)$ are approximately zero. Fundamentally, this is the difference between the on-site energy of two half polarons and one whole polaron. As the energy terms are quadratically dependent on the projected charge (see Eq. (2.2.14)), changing this projection will lead to a change in this energy difference, as seen in our calculations. The argument for the formation energy follows in a similar fashion, with the higher energy configuration in this case being the intrinsic, delocalized solution which has the relevant energy difference of

$$E^U_{\mathrm{form}} = nE^U_t(e/n) - E^U_t(1e), \tag{3.5.6}$$

where n is the number of polaronic sites (which is equal to the number of TM sites) in a supercell calculation. When the projection radius changes, the amount of charge ascribed to $+U$ interactions varies from the idealized fractions presented in the above equations. Since the $+U$ is correction is quadratic with the total number of projected electrons, this often leads to a particularly acute polaronic energy dependence on the projection radius that is manifest in nearly all polaronic properties (the major exception being MnO_2, which projects far less onto d-states, as discussed in the previous section).

3.6 Discussion

We have calculated four different electronic properties in five different materials. Not only have we calculated the band gap, we have also studied the three additional polaronic properties of these materials. From these results, we can establish a few trends as well as understand cases where these trends do not seem to hold. First of all, from our HSE06 calculations, we can see that in almost all cases, including semicore electrons leads to a band gap widening of up to 0.3 eV, and an increase in the activation energy of up to 30 meV. Formation energies can increase by up to 0.1 eV in $LiFePO_4$, but are relatively flat in the other cases. The polaron state is similarly unchanged in HSE06 calculations. We can then eliminate the variable of semicore electrons by comparing these results with our DFT+U calculations. Assuming that these effects are similar for both HSE06 and DFT+U calculations, we can begin to understand the effects of changing r_{PAW} on our DFT+U results. The general trend seems to be that all investigated polaron properties (E_p, E_{form}, and E_a) for sufficiently atomic-like polaron states (this excludes Mn_2O_4) decrease in magnitude with decreasing r_{PAW} when the DFT+U method is employed (in a manner that is dependent on r_{PAW}). This trend is much less observable in the calculated band gaps, and using the band gap as sole criterion for fitting U therefore does not seem sufficient for calculations predicting polaronic properties.

The band gap (with the important exception of LiFePO_4 as shown in Fig. 3.12a) remains relatively flat when varying r_{PAW}, and our results indicate that this arises from a cancellation of errors. Adding semicore electrons will increase the gap, but the simultaneous decrease of r_{PAW} leads to less projected on-site charge and therefore a smaller d-d separation. The decrease in the band gap is not as dramatic as one would expect from the projection onto r_{PAW}, as the occupied d states are typically far below E_F leading to an O 2p dominated valence band which is more CT-like in behavior. The important exception to this is LiFePO_4, whose VBM is strongly localized and d-like. In that case we can clearly see the effect of changing r_{PAW} on the d-d separation, as the HSE06 results remain flat here as well.

The three polaronic properties (E_p, E_{form}, and E_a) show remarkably similar behavior and trends, and unlike the band gap E_g, all depend strongly on the potential being used, with MnO_2 being the exception. The energy of the polaron state inside the band gap E_p is a better measure of the effects of changing r_{PAW}, as it is localized and strongly d-like, while relatively unaffected by semicore interactions. This is where we can see the clearest trends in all materials, except for MnO_2, with E_p depending monotonically on r_{PAW}. The polaron state in MnO_2 is much more hybridized with neighboring O 2p orbitals and is therefore largely unaffected by the projection onto pure $3d$ atomic orbitals as shown in Fig 3.15. This is an important property as polaron gap states can be experimentally measured, giving perhaps a better benchmark to fit the value of U on as the d-d character is more consistent with the spirit of DFT+U compared to the band gap which in many cases is more CT-like.

The formation and activation energies E_{form} and E_a are more direct indicators of polaron dynamics in a material. Here again, the DFT+U values are highly dependent on r_{PAW}, while the HSE06 results are much flatter. As energies calculated here have an exponential effect on the predicted dynamics, it raises a clear ambiguity for DFT+U results. Which potential is the one that we can trust? The best current comparison to experiment is hematite [48], where the activation energy calculated with the Fe potential with 8 valence electrons and $r_{\text{PAW}} = 2.3\ a_0$ comes closest to reproducing the measured value of 130-150 meV (see Fig. 3.7d). This is at variance with the traditional guidelines of smaller core and more electrons always leading to better results. Another example, related to the formation energy, is seen in LiFePO_4, where we were only able to localize a polaron with the large core Fe potential ($r_{\text{PAW}} = 2.3\ a_0$). Further analysis showed the reason behind this; the formation energy decreased sharply with decreasing r_{PAW} with the smallest core ($r_{\text{PAW}} = 1.9\ a_0$) having a formation energy of 20 meV. This not only lead to computational issues in finding such a shallow energy well, but, being lower than the activation energy, also lead to the qualitatively erroneous prediction that the hole polaron preferred delocalized band conduction over hopping.

The implementation of the on-site projection in Abinit [71] differs slightly from the implementation in VASP [50], and the Abinit results (see the appendix in Sec. A) appear to show less potential dependent variation. However, further potential database development is required to verify such improvements.

3.7 Conclusion

We have conducted an extensive study on the calculation of polaronic properties in several materials (rutile TiO_2, Fe_2O_3, $FePO_4$/$LiFePO_4$, and spinel MnO_2) with both DFT+U and HSE06 methods. We have studied the influence of both semicore electrons and projection radii on the calculated band gaps, polaron gap states, formation energies, and activation energies by varying the PAW potential for the transition metal, and have shown that the HSE06 method in almost all cases is more robust and more consistent (when the DFT+U PAW implementation depends on r_{PAW}). However, HSE06 does not give universally better results compared to the DFT+U method. While being more consistent, the drawback of hybrid functionals is the one to two orders of magnitude higher computational expense, making DFT+U methods still a very advantageous approach to studying polaronic properties.

Our calculations have shown that semicore electrons have a small effect on polaronic properties, increasing the calculated band gap by up to 0.3 eV, and activation energies by up to 30 meV. The effects of different projection radii on DFT+U calculations are, apart from the band gap, dramatically more significant. This directly arises from the U-term energy contribution which is quadratically dependent on the locally projected density matrix, and we believe that, since the band gap remains often relatively unaffected due to reasons discussed in this work, the impact of the projection radius on other properties is not generally emphasized in the literature. In particular, when studying polaronic properties with the DFT+U method, extensive care must be taken to remain consistent with not only the band gap but also properties such as the gap state, while taking the projection radius into account as an additional variable apart from the value for U. In general, one may extend these insights to other Mott-Hubbard influenced properties as well, as they might also be impacted if the projection radius were inconsistent between comparative DFT+U calculations.

To further progress in the analysis of polaronic properties predicted, more experimental measurements of polaron activation energies and gap state positions are needed. As polaronic properties are one of the factors determining the performance of energy and catalytic materials, having consistency in first principles calculations allows us to better compare them with measured values, as well as make more confident predictions in novel materials. Future work should focus on coupling theory and experiment in this manner.

4

Adiabatic polaron dynamics in $FePO_4$

4.1 Introduction

In the rapidly evolving field of clean energy materials, many emerging and established materials exhibit polaronic behavior [9, 20, 40, 41, 42]. In particular, polaronic hopping conduction is understood to contribute to the low conductivity suffered by many of the transition metal (TM) oxides and phosphates typically utilized in batteries [30, 31, 32, 33, 34, 35] and artificial photosynthesis [5]. Low conductivity often hampers the ability of these materials to harvest, store, or deliver energy. This usually occurs because d-shell electrons open a gap that localizes conduction electrons into small polaronic states [13, 18]. In fact, there are many more materials with similar correlated mechanisms that produce localized carrier behavior, including ionic systems, π-conjugated polymers [20, 21], as well as electron transfer processes in ion-aqueous solutions [22]. In order to engineer and improve the electronic performance of this important class of materials, it is necessary to investigate and understand the fundamental mechanisms that determine their polaronic hopping behavior.

It is usually assumed that the primary factors contributing to the hopping activation energy (E_a) arise form the nuclear reorganization of bonds between neighboring atoms during a polaronic transition [32, 33, 34, 35]. For example, a TM oxide/phosphate atom possessing a small electron polaron will typically experience an expansion of bonds with neighboring oxygen atoms (sketched as a larger “expanded” red circle in Fig. 4.1) due to electron-electron repulsion, compared to those TM atoms lacking an extra electron (sketched as smaller "contracted" blue circle Fig. 4.1). Likewise, the intermediate transition state is represented by a midsize magenta circle in Fig. 4.1, due to the midway extension of nuclear coordinates in this state. In the case of a hole polaron localized at a TM site, the process is described in an analogous fashion but with the situation reversed (i.e., there will be a contraction of TM-O bonds at the site of the hole polaron).

Such nuclear reorganization is, understandably, associated with the stretching of bonds and the corresponding relaxation of valence electron states. So logically one might assume that core electrons (both deep-core and semi-core as sketched in Fig. 4.1) play a negligible role in determining the polaron hopping barrier (E_a) [32, 33, 34, 35]. From this follows the treatment of core electrons as "frozen", i.e., not relaxing during a hopping event. This would appear to be a fair approximation for well shielded deep-core levels [32, 33, 34, 35]. However, the delineation is not so clear for semi-core levels in transition metals (sketched in green in Fig. 4.1), even those situated many tens of eV below valence electrons [109]. Though core electrons do not participate in bonding, they can "electronically relax" during a hopping process and may contribute substantially to the overall hopping barrier (E_a).

The impact of core-level relaxation is a subtle and important question which goes back to the development of computational methods in quantum chemistry and condensed matter physics [109, 110]. The most famous of these is Koopmans' theorem [and its density functional theory (DFT) variants] [72, 111], which allows us to estimate the ionization and affinity energies of systems in terms of their single particle eigenstates (ε). This is accomplished by assuming the orbitals are "frozen" during the ionization process. While this would appear to be a fair approximation when a charge state change occurs very rapidly relative to the time scale of electrons (e.g., optical excitations) [109, 112]. When ionization occurs on adiabatic (slow) time scales from the perspective of electrons, it is not clear which orbitals may be assumed to be

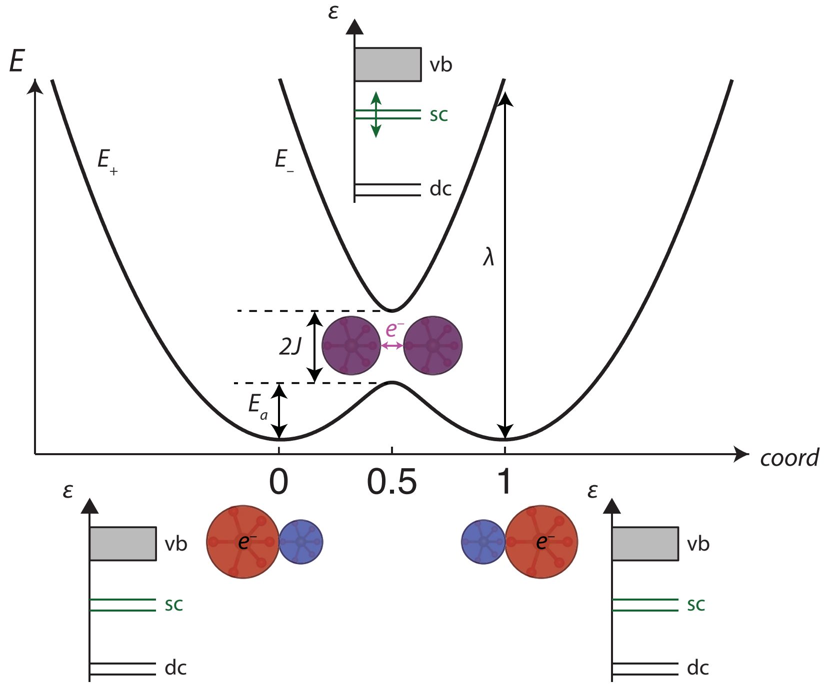

Figure 4.1: Two site electron polaron picture. Nuclear and electronic reorganization must occur to enable a polaron to reach the activation energy E_a, which represents the total energy (E) change that must be contributed by the system to move from a polaron localized on one atom (larger red circles) to another atom (smaller blue circles). At the intermediate transition state the electron is shared by both sites (equally sized purple circles). During this transition valence (vb), semi-core (sc, in green), and deep-core (dc) levels (ε) may electronically reorganize/relax and contribute to E. Electronic coupling between polaronic sites is represented by J.

"frozen" [109]. Small polarons provide an interesting framework to study the question of what orbitals can be viewed as "frozen", because hopping sites are often being ionized adiabatically/slowly (from the perspective of the much faster electrons) as an electron moves from one site to the next.

Due to computational limitations, in first-principles pseudopotential (PP) calculations on polaronic systems we often relax this "frozen orbital" assumption for valence electrons, but not for core electrons [27, 32, 33, 34, 35, 112, 113, 114]. To shed light on this more general "slow ionization" problem in first-principles electronic structure theory [72, 109, 110], we address the question: what is the impact of semi-core level relaxation upon the activation barrier of small polarons? As our model system we have chosen to study the delithiated form of $LiFePO_4$ ($FePO_4$, as shown in Fig. 4.2) [35],

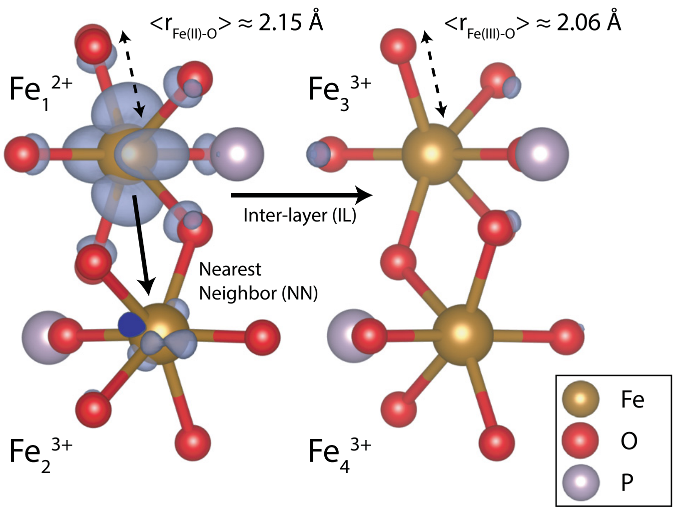

Figure 4.2: The atomic structure of $FePO_4$. A polaron located on one site (labeled Fe_1), with an isosurface of the real space charge density shown in grey. Its nearest neighbor is labeled Fe_2, and its neighbor in the out of plane direction is labeled Fe_3. Consequently, we study both the common in-plane nearest neighbor pathway (NN) as well as the closest inter-layer pathway (IL).

due to the known subtle interaction between the Fe *d*-shell and semi-core states and the immense practical importance of this material in Li-ion batteries [9, 27, 35]. In this system we show that semi-core level relaxation can alter the estimated polaronic hopping rate by an order of magnitude or more. While the focus of this study is on electron polarons in $FePO_4$, we find a similar effect for hole polarons in $LiFePO_4$ (see Appendix B). In general, it is expected that these results will have broad implications for first-principles polaronic hopping estimates in many TM compounds. The remainder of this chapter is organized as follows: in Sec. 4.2 we outline the relevant concepts in polaron theory (Sec. 4.2.1) followed by the computational details of this work (Sec. 4.2.2); then, we present the first-principles results in Sec. 4.3 in Secs. 4.3.1 and 4.3.2; lastly, we discuss the general implications of our results in Sec. 4.3.3 followed by a summary conclusion in Sec. 4.4.

4.2 Method

The physical properties of small polarons in solids closely resemble those of localized electrons on molecular sites, and as such polaronic theory borrows many concepts from molecular electron transfer (ET) theory (and vice versa) [13, 17, 23]. The reorganization energy (λ in Fig. 4.1) due to bond relaxation from the change in oxidation state can also be seen as similar to the molecular picture, where in this case it is the relaxation of TM-oxygen bond lengths on the TM site where the additional electron is localized. Small polaron hopping is therefore also analogous to ET theory, where the Franck-Condon principle requires that the electronic levels of the two sites are brought close enough together in order for hopping to occur, which can be accomplished by arranging the TM-oxygen shells to have the same bonding coordination (see Figs. 4.1 and 4.2). We refer to Sec. 2.3 for a comprehensive discussion on these fundamental concepts and theoretical considerations in polaronic hopping, and discuss the details of ab-initio core relaxation and polaron hopping approaches below in Sec. 4.2.1 and elaborate on the computational method that we have adopted in Sec. 4.2.2.

4.2.1 Ab-initio Approaches in Modeling Polaronic Hopping

Within DFT, the total energy expression (from which we extract polaron activation energies) may further divided into electronic and ionic terms:

$$E = \sum \varepsilon_i - \frac{1}{2} E_{\mathrm{H}} - \delta E_{\mathrm{xc}} + E_{\mathrm{ionic}}, \tag{4.2.1}$$

where the electronic contribution is composed of a summation over the electronic eigenstates (ε_i), less one-half the Hartree energy E_{H} and an exchange-correlation (XC) correction (δE_{xc}) [110]. Moreover, within the local spin density approximation (LSDA) and general gradient approximation (GGA) XC frameworks, the techniques of pseudopotentials [115] and more recently projector augmented wave (PAW) [27] potentials are amongst the most popular and widely used methods to approximate the all-electron (AE) scheme accurately for a wide variety of atoms and systems. The central idea of these methods is to separate the electrons into an inner core and an outer valence shell, with the assumption that outside a certain core radius the tightly bound core electrons have no significant overlap with the valence electrons and can therefore be frozen within the potential. For most applications this is an excellent approximation. However, there is no fundamental reason why core levels must always remain frozen and cannot provide significant corrections to the total energy as formulated by Eq. (4.2.1). For atoms such as transition metals where the valence d states are more strongly bound to the core, this approximation might not be sufficient and could result in significant discrepancies in energies (that is, core levels within $\sum \varepsilon_i$ and thereby E) [27, 113]. Moreover, the inclusion of spin polarization leads to localized spin densities that may have subtle interactions with the core electron density.

For PP and PAW methods, one can construct a potential which treats semi-core states as valence states [27, 114]. This allows for the adiabatic relaxation of semi-core states during hopping calculations at a slightly increased computational cost. For iron, in our model system of $FePO_4$, this means that we should place at least the $3p$ states and likely also $3s$ states in the "valence shell". Additionally, to fully capture polaron localization it is necessarily to incorporate onsite TM electron-electron interactions (see Fig. 4.2). In this work we have utilized the Hubbard DFT+U formalism [67], which leads to further localized d states and more spin interaction [30, 31, 116], further motivating the need to verify the accuracy of frozen core calculations by comparing them with the inclusion of semi-core valence states. From hereon, we label Fe $3d^6 4s^2$ results with $\mathrm{Fe_{fc}}$ and Fe $3s^2 3p^6 3d^6 4s^2$ results with $\mathrm{Fe_{sc}}$ during the course of our study on $FePO_4$.

To calculate activation barriers (E_a as shown in Fig. 4.1) between polaronic sites from first-principles, one usually assumes a nearest-neighbor (NN) pathway and interpolates coordinates between the two endpoints as a good initial estimate [30, 31, 116], and might apply the climbing image nudged elastic band (CI-NEB) [31, 49] method to further relax the pathway – hereafter simply abbreviated as the nudged elastic band (NEB) method. In most situations, this initial pathway estimate is well justified and results in a realistic barrier height, after relaxing this pathway using NEB. Additionally, it is assumed that hopping is adiabatic. In this work, we investigate in more detail where and why the adiabatic assumption is justified for our $FePO_4$ model system (as shown in Fig. 4.2). We do this by not only looking at the typical in-plane, nearest neighbor (nn) pathway, but also by considering a hypothetical pathway between layers (inter-layer). In this manner, we are able to study the validity of the adiabatic approximation on both pathways using a simple two-site polaronic transfer model [76, 77] within the context of the general criteria given by Eqs. (2.3.12) and (2.3.14) [23]; and the impact of semi-core level relaxation on the NEB computed polaron hopping barriers.

However, NEB calculations do not provide any information regarding attempt frequency $\omega/2\pi$ (as expressed by Eq. (2.3.14)). Molecular dynamics (MD) calculations, both analytical and quantum mechanical (ab-initio, AIMD), are typically used to study dynamic processes such as surface diffusion [117, 118] and more specifically ionic diffusion through battery materials [119, 120]. In our model $FePO_4$ system, we use AIMD to study polaron dynamics, as polarons diffuse through the collective motion of its nearby atoms. The advantage of MD calculations is that it allows us to treat the system in a dynamic fashion while including the effects of thermal fluctuations, as well as extract both the activation energy and the hopping attempt frequency ($\omega/2\pi$) simultaneously through the Arrhenius relation,

$$\Gamma = \nu_0 \exp\left(-E_a/kT\right), \tag{4.2.2}$$

which repeats Eq. (2.3.15). Here, $\nu_0 = \omega/2\pi$ is the frequency prefactor (hopping attempt frequency) and E_a is the activation energy. Similar work has been done previously on TiO_2 [40]. We can then relate these results to the barriers obtained from static (NEB) calculations, to both verify the static results and provide more detailed information on the hopping physics.

4.2.2 Computational Approach

Calculations were done utilizing the GGA functional by Perdew, Burke, and Ernzerhof (PBE) [96, 97] using projector augmented wave (PAW) [27] potentials as implemented in the Vienna ab-initio simulation package (VASP) [92, 93, 94, 95]. The on-site Hubbard term (U) was added to the functional (GGA+U) to incorporate the strong electron correlation in the Fe 3d orbitals and has been set to $U_{\text{eff}} = 4.3$ eV according to previous calculations [30]. Static calculations were done using $1 \times 2 \times 2$ supercells with an energy cutoff of 500 eV and a k-point grid such that energies were converged to within 1 meV per unit cell. The ionic positions and supercell dimensions are fully relaxed, with interatomic forces lower than 0.01 eV/Å. Ferromagnetic ordering was assumed throughout. An electron polaron localized in $FePO_4$ turns an Fe^{3+} site into Fe^{2+}. The orbital and spin configuration thus changes from $d^5(t_{2g}^3 e_g^2)$ to $d^6(t_{2g}^4 e_g^2)$ as both oxidation states of Fe are in high spin (HS) configurations. These HS configurations are maintained throughout this chapter.

The Fe PAW potentials Fe_{fc} and Fe_{sc} used in this study have 8 and 16 valence electrons, respectively. Additionally, the potentials have different core radii (2.3 a.u. and 1.9 a.u., respectively). A smaller core radius leads to a potential that is “harder”, i.e., it leads to more accurate results at the expense of requiring a larger basis set [27]. However, the on-site Hubbard term applies to a projected on-site density matrix that is defined only inside the PAW sphere [50, 98]. A smaller core radius will therefore have a different on-site projection, and might lead to different results. To investigate this in more detail, we first note that the band gap in both $FePO_4$ and $LiFePO_4$ does not change significantly depending on which Fe potential was used (see Appendix B).

Additionally, we have performed all-electron (AE) calculations according to the

APW+lo method as implemented within the WIEN2K software package [121]. Very briefly, the APW method separates the wave function into spherical harmonics inside the muffin-tin (MT) spheres and plane waves outside, with full relaxation of all core states. Within this method, DFT+U is similarly defined only inside the MT spheres. If we then take the MT sphere radii to be the same as the respective PAW core radii, we can separate the contribution of semi-core states from possible artifacts arising from DFT+U implementation specifics, especially in the case of our $\mathrm{Fe_{fc}}$ results. That is, we can use an MT sphere radius of 2.3 a.u., and yet allow full relaxation of semi-core states within the APL+lo method in a straightforward fashion without having to construct a specific PAW potential. We label AE results as $\mathrm{AE}_{2.3}$ and $\mathrm{AE}_{1.9}$, respectively, with the subscript number corresponding to the Fe MT sphere radius used (atomic units). Details of the WIEN2K calculations are provided in Appendix B.

MD calculations were performed with an energy cutoff of 500 eV and Γ-point sampling. The Nosé-Hoover thermostat [85] was used to control the temperature in an NVT-ensemble. Multiple calculations were run at various temperatures for 20 ps per run with a time step of 1 fs. Initial conditions were set by adding a random velocity to each atom in an intrinsic supercell, distributed according to Maxwell-Boltzmann statistics corresponding to the required temperature.

For our MD analysis we record individual hopping times Δt_i for all such events, after which the average temperature-dependent hopping rate is calculated as the mean of the individual rates. We then plot these averaged rates as function of temperature, and extract the hopping barrier according to the Arrhenius equation of Eq. (2.3.15). This way, we can obtain both the activation energy and the prefactor (hopping attempt rate) from the same set of MD calculations. It should be noted that this method of hopping statistics is different from classical methods [117, 118], where it is more common to calculate diffusivities from mean square displacements of the system at the end of the run, for many runs. The current method takes each hopping event individually and thus exhibits a larger statistical variance, however this is unavoidable due to the significant computational cost of running long ab-initio MD simulations.

4.3 Results

Before delving into detailed activation barrier (E_a) and rate (ω) calculations, let us start from the outset by addressing the question: is there any noticeable relaxation amongst semi-core levels during the polaronic hopping process? To address this we have fully relaxed the transition state barrier for a polaron hopping between two NN sites as sketched in Figs. 4.1 and 4.2, utilizing the NEB method with the inclusion of Fe $3s$ and $3p$ semi-core sates ($\mathrm{Fe_{sc}}$). Comparative transition state activation energies will be presented shortly, but let us first turn our attention to Fig. 4.3a which shows the projected density of states (PDOS) of the $\mathrm{Fe_{sc}}$ atomic orbitals in the intrinsic $FePO_4$ configuration (i.e., without a polaron present). As expected due to symmetry, all the Fe $3s$ states have the same energy. Similarly, there are three peaks for the identical $3p_x$, $3p_y$, and $3p_z$ states. They lie deep below E_F and therefore do not influence the bonding properties of the system. This is further elucidated by their real space distribution (inset of Fig. 4.3a), showing that these semi-core states are spatially confined to their respective Fe centers. The $3d$ states are part of the valence and conduction bands, and the band gap is 1.9 eV which is in good agreement with earlier calculations [56].

Adding an electron in Fig. 4.3b leads to the formation and occupation of a polaronic state as shown by the sharp $3d$ peak at the Fermi energy. However, this also breaks the symmetry and lifts the degeneracy of the Fe $3s$ and $3p$ semi-core states between different ions, separating them in energy. In other words, there is significant polaron induced electronic relaxation of the deeper lying states, an effect that would not be present if those states were kept frozen. Moreover, electronic relaxation of the semi-core states is pronounced when we move from the polaronic ground state configuration "POL" in Fig. 4.3b to the polaronic transition state "TST" in Fig. 4.3c

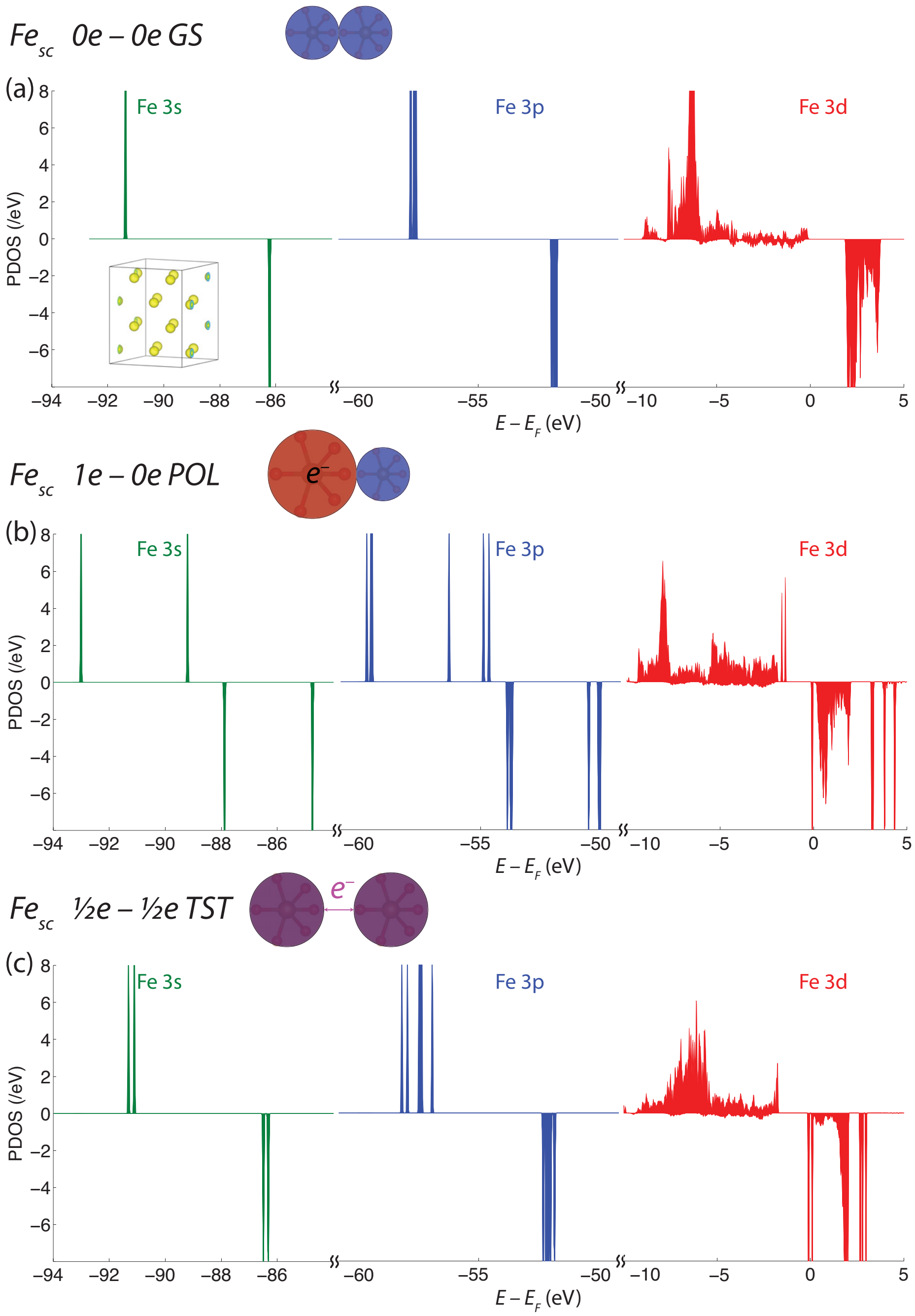

Figure 4.3: Projected density of states (PDOS) for the two Fe atoms taking part in the electron transfer process for three relevant configurations represented by the schematic images of FeO_6 coordinations as introduced in Fig. 4.1. The PDOS for majority and minority spin are plotted on the positive and negative vertical-axis, respectively. The semi-core 3*s* (green peaks, left) and 3*p* (blue peaks, center) states lie deep below the Fermi energy, while the 3*d* (red curves, right) valence states contribute to the chemistry of the system. (a) PDOS of the intrinsic ground state configuration ("GS") without additional electrons introduced. (a, inset) Real space distribution of the Fe 3*s* semi-core states. (b) PDOS of the polaronic ground state ("POL"), i.e., the electron is fully localized on one Fe site. (c) PDOS of the transition state ("TST"), where both Fe sites have similar coordination and share the additional electron.

(e.g., coordinates 0 and 1 in Fig. 4.1, respectively), where the electronic levels undergo a non-trivial shift and splitting between their relative energies. While the bonding chemistry is accurately described by the polaronic state at E_F and surrounding 3d states (red in Fig. 4.3), the electronic relaxation of semi-core states between the "POL" and "TST" configurations can lead to different total energies (and thereby activation energies E_a) depending on whether a semi-core ($\mathrm{Fe_{sc}}$) or frozen-core ($\mathrm{Fe_{fc}}$) potential is used in the calculation as expressed by Eq. (4.2.1). A similar relaxation of semi-core states was calculated in $LiFePO_4$ (provided in the Appendix B).

In the subsequent sections we investigate the effects of semi-core relaxation by comparing results with a $\mathrm{Fe_{fc}}$ potential which keeps the $3s$ and $3p$ states frozen and a $\mathrm{Fe_{sc}}$ potential which allows these semi-core states to fully relax. It follows that there is a significant difference in polaron activation energies and dynamics depending on which potential is used. Our results show similar trends in both cases, that dynamic barriers obtained from MD are comparable to static (NEB) barriers, and that non-NN hopping is significant. Using a basic two-site hopping model, we then show that only the NN pathway is within the adiabatic regime, validating both assumptions in the case of $FePO_4$. We argue that it is necessary to verify these conditions when modeling similar polaronic materials.

4.3.1 Calculating transition states

Fig. 4.4 shows our calculated hopping barrier (E_a) for electron polarons in $FePO_4$, whose NN value in Fig. 4.4a for the $\mathrm{Fe_{fc}}$ case (blue triangles) is comparable to previously calculated results (see also Fig. 4.2) [30, 31]. Fig. 4.4b shows the calculated barrier for the non-NN inter-layer (IL) pathway (see also Fig. 4.2). The energies for the $\mathrm{Fe_{sc}}$ study are shown as red squares.

Overall, in Fig. 4.4 we can clearly observe the energetic differences between the two potentials: using the $\mathrm{Fe_{sc}}$ potential leads to barriers that are roughly 100 meV

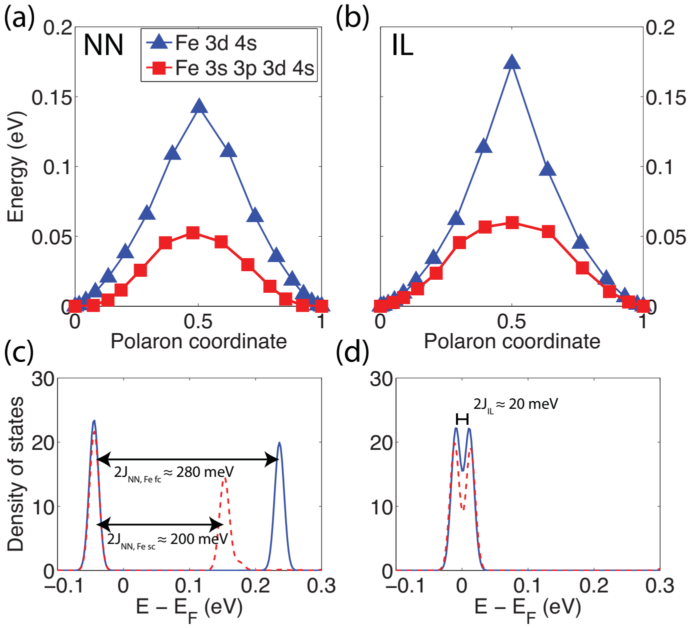

Figure 4.4: Activation energies (a) and (b) calculated with the CI-NEB method using both 8-valence $3d^6 4s^2$ ($\mathrm{Fe_{fc}}$ blue upright triangles) and 16-valence $3s^2 3p^6 3d^6 4s^2$ ($\mathrm{Fe_{sc}}$ red squares) Fe potentials, together with the level splitting at the transition state arising from the site coupling in (c) and (d), respectively. (a) and (c) nearest neighbor (NN) barrier. (b) and (d) inter-layer (IL) barrier.

lower than the barriers obtained with the $\mathrm{Fe_{fc}}$ potential.

We attribute this discrepancy to the localized electron inducing additional electronic relaxation and spin interactions with lower lying semi-core states on the Fe sites (as illustrated in Fig. 4.3). Moreover, we can compare the results with those obtained from AE calculations (Appendix B). For the $\mathrm{Fe_{fc}}$ potential, the barrier is 142 meV compared to a barrier of 77 meV for the $\mathrm{AE_{2.3}}$ calculation. The barrier for the $\mathrm{Fe_{sc}}$ potential is 52 meV, compared to the $\mathrm{AE_{1.9}}$ barrier of 46 meV. The significant difference between the $\mathrm{Fe_{fc}}$ and the $\mathrm{AE_{2.3}}$ barrier, combined with the smaller difference between $\mathrm{Fe_{sc}}$ and $\mathrm{AE_{1.9}}$, underscores that semi-core relaxation is the main cause of the lowering of the barrier. It is known that having semi-core valence electrons leads to more accurate results for magnetic transition metals such as iron [27]. In the case of polaronic hopping barriers in $\mathrm{FePO_4}$, this leads to a significant lowering of the barrier, and predicted room temperature mobilities that are one or even two orders of magnitudes above that when using the more common $\mathrm{Fe_{fc}}$ potential (as outlined in

Table 4.1 and to be discussed shortly). A similar trend was computed in $LiFePO_4$, with the Fe_{fc} barrier at 257 meV and the Fe_{sc} barrier at 79 meV (see Appendix B). We argue that this might affect hopping barriers in other transition metal polaronic materials such as hematite and titanium dioxide in a similar fashion and recommend that energy calculations be done using potentials that incorporate semi-core electrons in the valence states.

Furthermore, it is commonly understood [30, 31] that electronic transport in $FePO_4$/$LiFePO_4$ is primarily two-dimensional, staying within the plane due to Fe sites being separated by just O atoms in between (e.g., hopping between Fe_1 and Fe_2 in Fig. 4.1). The inter-layer pathway has phosphate groups isolating the Fe sites, obstructing conductivity in the third dimension (e.g., hopping between Fe_1 and Fe_3 in Fig. 4.1). However, our calculations in Fig. 4.4b show that this IL pathway is energetically higher, but still within the range where hopping events could theoretically still be observed, in particular, for the low E_a estimate provided by the Fe_{sc} potential. To verify how realistic this predicted pathway is, we have conducted a more in-depth study of adiabaticity and the validity of the adiabatic approximation for both pathways.

Figs. 4.4c and 4.4d show the Fe_{sc} and Fe_{fc} PDOS close to the Fermi energy E_F at the charge transfer transition state (polaron coordinate 0.5 in Figs. 4.1 and 4.4). In this state there is an equal probability of finding the electron on either site, and therefore a twofold degenerate polaronic state at E_F. Electronic coupling (J) then lifts this degeneracy and splits the two states into a “bonding” and “antibonding” state. We take this separation between the bonding and antibonding state to be our approximation to the site coupling term J as $2J = E_{\mathrm{AB}} - E_{\mathrm{bonding}}$ as sketched in Fig. 4.1 and discussed in Sec. 2.3 [45].

For the NN transition state $2J \simeq 200$ meV for Fe_{sc} and $2J \simeq 280$ meV for Fe_{fc}. This indicates that there is sufficient electronic coupling through the Fe-O-Fe bonds such that the NN transition may be regarded as adiabatic, as we shall evaluate shortly.

For the inter-layer transition state however, there is a much weaker electronic coupling $2J_{\text{inter}} \simeq 20$ meV between the two sites regardless of the potential utilized, and both states remain at E_F. This can be attributed to the phosphate groups isolating the sites electronically (as shown in Fig. 4.2). Since the adiabaticity parameter η_2 as given by Eq. (2.3.12) depends strongly on J, we predict the inter-layer transition to be highly diabatic and thus very unlikely to occur. It also implies that our results for the non-NN transition are unrealistic, as DFT is a ground state theory and therefore inherently adiabatic – although time dependent (TD) DFT should be able to capture such diabatic transitions.

To compute η_2 using Eq. (2.3.12) and fully evaluate adiabaticity, a frequency factor ω is required. As discussed back in section 2.3, this is usually taken as the optical phonon frequency of the system. Our approximation is to use the frequency prefactor of Eq. (2.3.15) obtained from MD calculations to estimate $\omega = 2\pi v_0$ as described in the next section [see also the discussion around Eqs. (2.3.14) and (2.3.15)]. Before detailing our MD results, let us briefly state the impact of the obtained frequencies on the adiabaticity parameter (η_2). For the nearest-neighbor pathway, we obtained $\eta_2 \simeq 0.35$ for Fe_{fc} and $\eta_2 \simeq 2.6$ for Fe_{sc}, concluding that the NN electron transfer process can be seen as reasonably adiabatic ($\eta_2 > 1$). However, for the inter-layer pathway $\eta_2 \simeq 0.002$ and $\eta_2 \simeq 0.01$, respectively, indicating that this is a highly diabatic process. Therefore, we argue that the nearest-neighbor pathway can be well approximated with the adiabatic relation of Eq. (2.3.15), but that we must use the non-adiabatic approach [Eq. (2.3.16)] for the inter-layer pathway instead.

4.3.2 Polaron hopping dynamics

To compute the frequency prefactor $v_0 = \omega/2\pi$ and further verify the NEB computed activation barriers (E_a), the hopping of electron polarons in FePO_4 was calculated in the temperature range of 300 K – 500 K for Fe_{fc}, and 143 K – 300 K for Fe_{sc} calculations, with more hopping occurring at higher temperatures. Fig. 4.5 shows a few

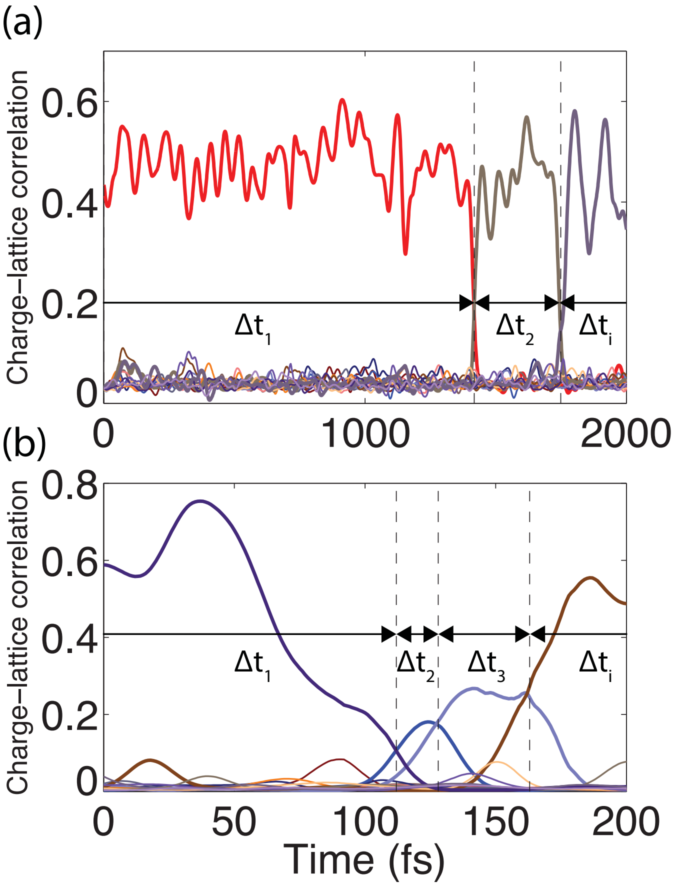

Figure 4.5: Correlation analysis on a sample MD run. We calculate the average Fe-O_6 bond lengths of all 16 Fe sites scaled to unity, and multiply these values with their respective projected $3d$ electron occupations (also scaled to unity). The resulting charge-lattice correlation statistic should give a reasonable indication of the current polaron location.

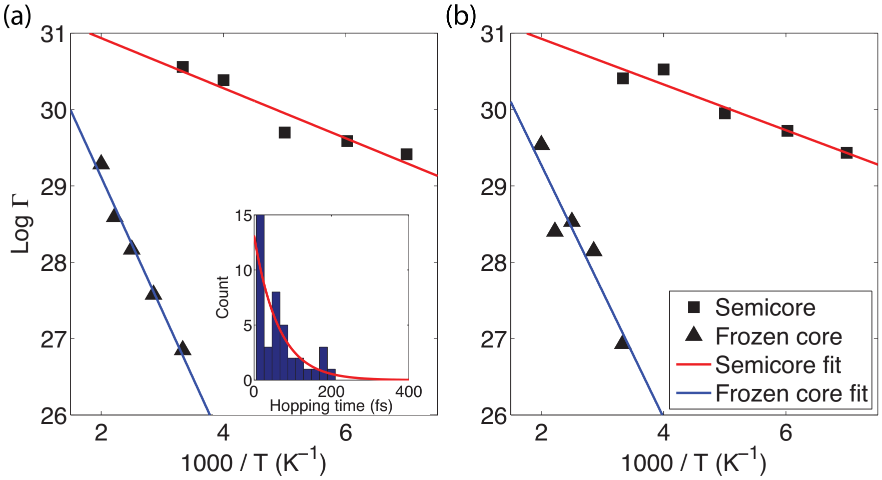

Figure 4.6: Polaron AIMD hopping statistics. $\log \Gamma$ is defined as the natural logarithm of Γ, where Γ is given in units of s^{-1}. Left: (a) nearest-neighbor hopping. Right: (b) nearest inter-layer hopping. Red line: linear fit of semi-core calculations at T = 143 K, 166 K, 200 K, 250 K, and 300 K. Blue line: linear fit of frozen core calculations at T = 300 K, 350 K, 400 K, 450 K, and 500 K. Inset: exponential Poisson distribution of hopping times shown for one temperature point. The mean of this distribution was taken to be the mean hopping rate at that particular temperature. Similar statistics were done for each temperature point on these Arrhenius plots.

characteristics of this hopping process (using the correlation methodology discussed in Sec. 4.2.2). While most of the iron sites and their oxygen bond lengths are in the Fe^{3+} ionic state $[\Delta\rho(t)\Delta r(t) \sim 0]$, there is one site with high correlation, indicating that the polaron is currently located at that specific site. We can thus say that hopping occurs whenever another site takes over as the site with the highest polaron correlation.

As shown in Fig. 4.5, polaron transitions between sites are well distinguishable as transitions between curves with the highest charge-lattice correlation $[\Delta\rho(t)\Delta r(t)]$. The oscillations over time show the effects of adding thermal fluctuations, and hopping will take place whenever the random fluctuations align to push the polaron over the energetic barrier, allowing both the distortion configuration and the extra charge to migrate to another location. We record the times of each such transition, and take the time between each transition Δt_i as their respective hopping time.

Theory [77] suggests that small polaron hopping exhibits Markovian behavior, i.e., hopping events occur independently from each other at a constant average rate determined by the system temperature. We therefore expect our hopping events to be exponentially distributed (see inset of Fig. 4.6), and take the calculated average time between hopping events $\overline{\tau(T)}$ to be our typical rate $\overline{\nu(T)} = 1/\overline{\tau(T)}$. Calculating rates at different temperatures then allows us to view the relationship between temperature and average hopping rates, as shown in the Arrhenius plots of Fig. 4.6.

The numerical results are summarized in Table 4.1. Diffusivities and mobilities were obtained from the typical relations [122]:

$$D = \frac{l^2}{2d}\Gamma, \qquad \mu = \frac{e}{kT}D, \tag{4.3.1}$$

where $d = 2$ is the dimensionality of the system, e is the elementary charge, and $l \simeq 3.86$ Å is the nearest neighbor distance between polaron sites (i.e., Fe atoms). Here we can see very clearly the impact of including semi-core states. Not only does it change the barriers drastically, it also raises the hopping frequency accordingly due to these lower barriers. Whereas we can simulate T = 500 K within reasonable accuracy for $\mathrm{Fe_{fc}}$, the average frequencies for $\mathrm{Fe_{sc}}$ are already nearing the numerical resolution of the 1 fs timestep at T = 300 K. Our MD results are consistent with the predictions from our NEB calculations for the $\mathrm{Fe_{fc}}$ case, although the values for the $\mathrm{Fe_{sc}}$ MD results are consistently off by roughly 20 meV. This result casts into doubt the validity of the Markovian assumption, as hopping rates are so high (Fig. 4.5b) that the system might not have enough time to relax into its new polaron ground state before attempting another hop [77]. This might result in hops that are slightly correlated with each other inducing a slight memory effect, resulting in the lower calculated activation barrier. However, overall transition state theory (NEB) and the MD results agree fairly well.

Nevertheless, one could argue that there might be room to further improve the variance in the computed MD results, as exhibited within the inset of Fig. 4.6. However,

	Frozen core	**Semi-core**
Nearest Neighbor		
$E_{a,\text{NEB}}$ (meV)	142	52
$E_{a,\text{MD}}$ (meV)	151	28
ν_0 (10^{13} Hz)	14.75	5.26
D (cm^2/s)	6.41×10^{-4}	2.66×10^{-2}
μ (cm^2/V s)	0.03	1.03
Inter-layer		
$E_{a,\text{NEB}}$ (meV)	174	59
$E_{a,\text{MD}}$ (meV)	143	26
ν_0 (10^{13} Hz)	14.19	4.92

Table 4.1: Barrier and frequency prefactors obtained from AIMD calculations. The advantage of using AIMD is that it enables us to calculate both barriers and prefactors simultaneously. Using these results, the diffusivities and mobilities were calculated at a temperature of 300 K. There is a $\sim$20 meV discrepancy between MD and NEB computed barriers for both Fe_{sc} and Fe_{fc} potentials.

we maintain that our results are statistically significant by noting that the barrier is exponentially related to these statistics. For example, a 20 meV increase in the MD computed barrier (in line with the NEB results in Fig. 4.4) would lead to a doubling of the mean and width of the distribution (in the inset of Fig. 4.6). Such a drastic change would not be achievable by sampling more points to reduce the variance.

4.3.3 Discussion

It is important to note that this analysis was done without considering the significant effects of DFT+U projection as I have detailed in Chapter 3. This does not change the assertion that semi-core states have a significant effect on polaron dynamics in FePO_4 (as was partially shown in Chapter 3). However, the present analysis would be greatly improved by an additional study which does incorporate the effects of projection, e.g., by constructing additional PAW potentials with $r_{\text{PAW}} = 1.9\ a_0$ and $Z_{\text{val}} = 8$ on one hand, and $r_{\text{PAW}} = 2.3\ a_0$ and $Z_{\text{val}} = 16$ on the other hand and including additional comparisons using these potentials, as only then could we comprehensively eliminate projection as a second variable. Including additional HSE06 calculations would be another approach, although the additional computational costs associated with hybrid functionals combined with the long simulation times of MD calculations could prove to be practically infeasible.

Overall, the results of our combined NEB and MD study (summarized in Table 4.1) indicate a sizeable ~100 meV energy difference between Fe_{sc} and Fe_{fc} calculations of the polaronic hopping barrier (E_a). We attribute this to the electronic relaxation of semi-core states, including spin interactions, that are hard to capture within the frozen core approximation [as summarized by Eq. (4.2.1) and displayed in Fig. 4.3]. The activation barriers obtained with all-electron calculations further emphasize the effect of semi-core relaxation in this material. A 100 meV discrepancy may be tolerable in some instances, however in $FePO_4$ it leads to drastically different barriers and therefore a qualitative difference in diffusion analysis (as shown in Table 4.1). With our lower barriers, the calculated diffusion constant and mobility are two orders of magnitude higher than what was previously predicted. More practically, this opens up an interesting avenue of theoretical investigation in polaronic hopping during the charging and discharging of $LiFePO_4$ [9, 35]. In particular, it indicates that the exceptionally low conductivity observed during $LiFePO_4$ intercalation might be due to correlated motion between polarons and Li-ions. It also supports the notion that the rate-limiting factor in $LiFePO_4$ intercalation is the diffusion of Li^+ ions.

More generally, we argue that within the scope of polaronic materials and transition metal redox-type cathodes with strong spin-polarized d orbital correlation effects, the p (and perhaps also s) semi-core states should always be included in the "valence" shell to capture and explore electronic relaxation and spin interactions. These interactions might even be significant for mid-to-late transition metals, which have larger d shells.

Furthermore, to evaluate adiabatic assumptions common in transition state theory based polaron hopping calculations: we have done an extensive molecular dynamics study on free polaron hopping in $FePO_4$ to sample the available diffusion pathways in a dynamic fashion, incorporating both the typical nearest-neighbor pathway as well as the most likely nearest inter-layer transition adiabatically. Our results show reasonable agreement within 10 meV compared with the NEB results for both the frozen core and semi-core calculations. This remains within the precision of both NEB and MD methods. Though our adiabatic DFT calculations show a similarity in activation energies between the nearest-neighbor and nearest inter-layer pathways, however by looking at the interaction parameter J we have demonstrated that only the nearest-neighbor transition can be treated realistically within the adiabatic approximation typically inherent in Born-Oppenheimer based DFT. For the nearest inter-layer transition there is a phosphate group between the sites which lowers this J coupling to almost 0, indicating that such transitions are highly non-adiabatic and as such are far less likely to occur in reality. With this part of our study, we conclude that the nearest-neighbor assumption is well justified for $FePO_4$, but we argue that this condition should be verified for electronic transitions in all polaronic materials.

4.4 Summary & Conclusion

In this chapter, we have looked at a few important concepts and ab-initio specifics of polaronic behavior in TMOs using $FePO_4$ as our model system. Our ab-initio computations were performed within the Hubbard DFT+U formalism, utilizing U-ramping [84], applied to the conventional GGA DFT functional. In this model system, it was determined that interactions between spin-polarized d-electrons and the semi-core p- and s-electrons might significantly lower small polaronic hopping barrier estimates by up to ~100 meV. While semi-core levels do not participate in bonding, they can affect small polaron activation energies through electronic relaxation and spin interactions. As such, TMOs are interesting systems to study these effects due to the significant interaction between polaronic states and on-site core electrons. We argue that semi-core relaxation might generally influence the properties of similar polaronic materials, and the impact of deep core-level interactions should thus be examined for these materials as well.

Furthermore, we have evaluated the adiabaticity of polaronic barriers in $FePO_4$.

We have considered additional diffusion pathways, as well as sampled the stochastic nature of this system in a thermally fluctuating environment by means of AIMD. Our results have shown that, while there are indications of multiple pathways utilized by the system, only the nearest neighbor pathway lies well within the adiabatic regime. Therefore, our adiabatic transition state theory is insufficient in treating the other, non-adiabatic pathways accurately. Since polaronic hopping can be described as electron transfer events, we argue that the assumption of adiabaticity should always be verified in similar polaronic materials. Moreover, we have shown that AIMD could be a useful tool in sampling pathways without prior assumptions, as well as obtaining the frequency prefactor without needing to resort to phonon calculations.

Lastly, on a more practical note, based on these lower polaron activation barrier results: we expect the rate-limiting factor in $LiFePO_4$ intercalation to be the hopping of Li^+ ions, having activation energies of more than four times that of free polarons [30, 31, 32, 33, 34, 35]. Exploring correlated polaronic and Li^+ ion diffusion, in the context of semi-core level relaxation, would be an interesting topic of future investigation.

5

Crystal structure and adiabatic polaron transfer

5.1 Introduction

The previous chapters have focused on applying first principles methods to study polaronic properties in a selection of novel energy materials (Li_xFePO_4 in Chapter 4, and TiO_2, Fe_2O_3, and $Li_xMn_2O_4$ in Chapter 3), as well as the impact of different DFT+U projection schemes on calculating these polaronic properties (Chapter 3). In this chapter, we will focus on fundamental properties of polaron transport in TM oxide crystals in a more qualitative fashion. While small polaron transport in a crystal lattice occurs mostly between nearest neighbours, the specific crystal structure and its associated symmetries greatly influence the polaron transfer characteristics, in particular within the adiabatic regime. A particular example is when one attempts to calculate the polaronic transition state between two TM sites in $SrTiO_3$ compared to that in $LaMnO_3$. Both materials have the (distorted) perovskite structure, but we can calculate an adiabatic TS in $LaMnO_3$ (d^5 polaron) while we cannot do the same in $SrTiO_3$ (d^1 polaron). This arises from qualitative differences between a t_{2g} polaron in $SrTiO_3$ and an e_g polaron in $LaMnO_3$ within the perovskite structure. Another example is the relatively high inter-site coupling ($J = 0.42$ eV) for a polaron in spinel-type $MgFe_2O_4$ compared to that in MnO_2 with the same structure ($J = 0.08$ eV), where this difference arises again from t_{2g} and e_g polarons having different properties. More generally, we will argue that a qualitative trend exists where the specific nature of the orbital (t_{2g} or e_g) [80, 81] occupied by the polaron combined with specific properties of the crystal structure determines both the existence of an adiabatic transition state as well as the relative degree (J) of its adiabaticity.

In this chapter, focusing on structures with octahedral coordinated metal cations (MO_6), we first describe a fundamental difference between crystal structures where the MO_6 octahedra are connected through shared edges (rutiles, spinels, and other structures), and structures where they share common vertices (most commonly perovskites). We then highlight certain elements of exchange theory [79, 123, 124, 125, 126, 127, 128], and more specifically the dependence of the inter-site coupling term J on the inter-site orbital overlap [79, 81, 129]. As electronically, a TM-centered polaron can be seen as an extra electron occupying a TM site, we can apply the same principles to this extra electron when studying the polaronic TS in a similar fashion while treating the polaronic structural distortions in an indirect way through the requirement of energy level alignment according to the Franck-Condon principle. We are then in a position to elaborate on the aforementioned trends after combining these exchange principles with the crystal structure connection properties, and we demonstrate these trends by calculating the exchange properties (J) in several example materials. The results of these calculations are in line with our hypothesis that the crystal structure can strongly determine the degree of adiabatic polaron hopping transport.

5.2 *Structure dependent orbital exchange*

Fig. 5.1 shows three important families of crystal structures, namely the rutiles (Fig. 5.1a), spinels (Fig. 5.1b), and perovskites (Fig. 5.1c). All three structures have important applications in novel energy materials [37, 38, 130, 131, 132, 133, 134]. Many TM oxides with these structures exhibit polaronic behaviour [43, 44, 46], and as such we can use them both for practical calculations as well as models for qualitative investigations.

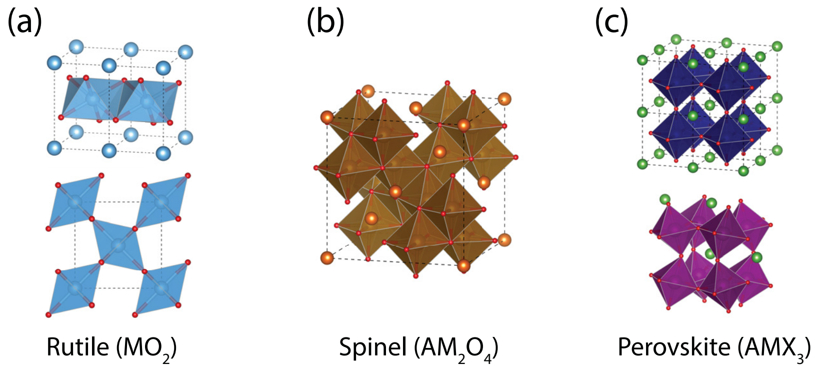

Figure 5.1: (a) Rutile, (b) spinel, and (c) perovskite structures. The rutile structure is adopted by many binary TM dioxides. The spinel and perovskite structures are both ternary compounds, with the A atom typically a large alkali (A), alkaline earth (AE), or rare earth (RE) metal, and the B atom a smaller transition metal ion.

For electron (and polaron) transfers between nearest neighbours, there is one fundamental property of these (and other) structures, i.e. how the MO_6 octahedral complexes are connected to each other. This is typically through either a shared (O) ligand, which we will call a single ligand ("1L") connection, a shared edge (two ligand connection, "2L"), or a shared face ("3L") which is more rare. Most structures are connected through octahedral edges (2L) including the rutile (Fig. 5.1a, down the c-axis) and spinel (Fig. 5.1b) structures. Perovskites (Fig. 5.1c) are different in that the octahedra are 1L-connected. This fundamental difference becomes apparent in Fig. 5.2 where we have plotted example transition states for both configurations.

In the 1L case (Fig. 5.2a) there is a shared O atom between the TM sites, and electron transfer must therefore also involve this shared O atom. This particular process falls under the double exchange mechanism [79, 123], and has been studied extensively in literature [79, 81, 123, 124, 135, 136, 137]. In contrast, the TM sites are closer together in the 2L case (Fig. 5.2b) and direct cation-cation interaction can occur [124]. 3L cases are rare but direct transfer can occur in these cases through linear combinations of t_{2g} orbitals.

As we are describing exchange interactions [81] between sites, the importance of the exchange parameter J becomes apparent. Mentioned before in Chapter 2 through

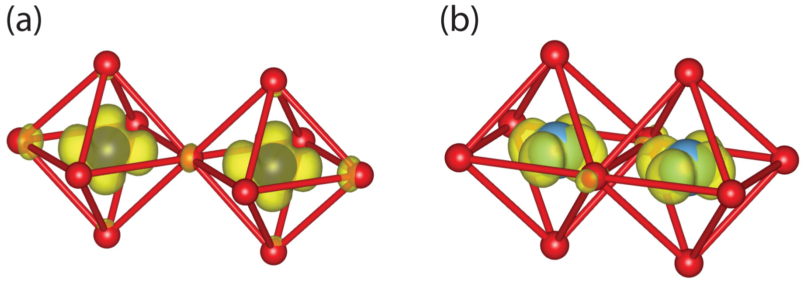

M–O–M (~180˚)

M– –M
M–O–M (~90˚)

Figure 5.2: Showing the difference between (a) octahedra connected through shared corners, also labelled as "1L", and (b) octahedra connected through shared edges, also labelled as "2L". The TM-TM distance in (a) is large, and the resulting interaction between TM sites needs to go through the shared O atom (M-O-M). In contrast, the TM-TM distance in the 2L is much smaller, and interaction can take place directly between the TM sites. Here, an additional indirect interaction is possible through the two M-O-M bonds that are angled at close to 90°, although this interaction is typically much smaller in magnitude.

Eqns. (2.3.9) and (2.3.10), as well as from the two-site model described in Sec. 2.3, we have established a relation for J as a measure for adiabaticity of the transfer process. As Eq. (2.3.9) describes J as an overlap between the two states, the strength of J will be determined in both cases in Fig. 5.2 by the amount of overlap between the two local orbitals. In our case of neighbouring d orbitals (and similarly for f orbitals), the overlap is greatest when the lobes of the d (f) orbitals face each other. If there is little to no overlap–i.e. if the lobes are not facing each other, or if the interatomic distance is too large for direct interaction, then J will be very small and adiabatic transfer is not likely to occur for this process. Small polarons form a convenient tool with which to study such exchange interactions as they are inherently localized to specific sites.

As a result for the 1L case (Fig. 5.2a), the orbital overlap will be greatest when both orbitals are of d_{z^2} form and face the $2p$ orbitals of the shared O atom (M-O-M interaction, see Ref. [79, 123]), and could lead to stronger hybridization with these $2p$ orbitals. Facing $d_{x^2-y^2}$ orbitals will achieve a similar situation with slightly less overlap [81, 129]. Both cases correspond to e_g orbitals that face the O ligands [47], and combined with the observation that the lobes of t_{2g} orbitals do not face each other and and therefore will have very little overlap (also from the large cation-cation distance), we can conclude that adiabatic TM-TM polaron transfer in 1L systems can only occur for e_g polaron configurations–e.g. a d^4 HS polaron can couple adiabatically to another site whereas a d^1 or d^4 LS polaron cannot. The 1L case corresponds largely to the perovskite structure as well as certain directions in structures with both 1L and 2L connections. These observations suggest that we can calculate adiabatic TS for polarons in $LaCrO_3$ (d^4 polaron) and $LaMnO_3$ (d^5 polaron) as well as $KNiF_3$ and $KCuF_3$ (d^9 and d^{10} minority spin polarons, respectively), but not for other materials such as $SrTiO_3$ (d^1 polaron), or for directions other than the c-axis in rutile TiO_2.

The 2L case is different as the octahedra in these systems share edges. This means that the lobes of t_{2g} orbitals can now face each other and contribute to the coupling strength J. Additionally, the metal cations are much closer to each other (~ 3 Å) compared to 1L materials (> 4 Å) which can lead to much stronger direct orbital interactions [124]. In some cases (see Fig. 5.8 for our calculation in $MgFe_2O_4$) when the orbitals closely resemble true atomic orbitals, we can see Slater-Koster tight-binding behaviour [138] of the polaron TS, where the coupling term J varies as $1/d^5_{M-M}$ [81, 129]. As most TM oxides are of the 2L kind, this is the most prevalent situation. In this configuration, apart from such direct M- -M interactions (adopting the nomenclature used by Goodenough [124]), there can also be M-O-M interactions where the M-O-M angle is approximately 90° (see Fig. 5.2b). This explains that, while the TS and J in rutile TiO_2 (d^1 polaron) and spinel $MgFe_2O_4$ (d^6 minority spin polaron) suggest high adiabaticity, it is also possible to calculate an adiabatic TS in spinel MnO_2 despite the polaronic configuration in this material being d^4. In this particular case, the TS shows (Fig. 5.9) two $d_{x^2-y^2}$ orbitals that do not face each other, but the lobes point towards the two shared O atoms. As shown in Ref. [124], this 90° M-O-M interaction is relatively small, and the corresponding J should therefore be significantly smaller.

Crystal orbital			**Coupling**	**Example materials**
Single ligand (1L)				Perovskites
t_{2g}	d^{1-3}	(HS)	$J \ll 1$ meV	$SrTiO_3$, $LaVO_3$
	d^{6-8}	(HS)		$LaFeO_3$
	d^{4-6}	(LS)		$LaMoO_3$ (LS)
e_g	d^{4-5}	(HS)	$J > 100$ meV	$LaCrO_3$, $LaMnO_3$
	d^{9-10}	(HS)		$KNiF_3$, $KCuF_3$
	d^{7-8}	(LS)		$LaMoO_3$ (HS), $LaRhO_3$
Double ligand (2L)				Rutiles, spinels
t_{2g}	d^{1-3}	(HS)	$J > 100$ meV	TiO_2
	d^{6-8}	(HS)		Fe_2O_3, $MgFe_2O_4$
	d^{4-6}	(LS)		$MgMo_2O_4$ (LS)
e_g	d^{4-5}	(HS)	$J \sim 10$ meV	MnO_2 (spinel), $MgCr_2O_4$, $MgMo_2O_4$ (HS)
	d^{9-10}	(HS)		
	d^{7-8}	(LS)		

Table 5.1: Summary of the qualitative predictions based on exchange interactions in 1L and 2L structures. Approximate energy scales for the coupling strength J are shown for each configuration, with $J \ll 1$ meV, $J > 100$ meV, and $J \sim 10$ meV indicating zero effective coupling, strong coupling, and weaker coupling through unfavourable angles, respectively. Also listed are a few examples of typical materials per orbital configuration. Note: the orbital configurations shown in this table assume that the polaron has already been added. For example, $SrTiO_3$ has a d^1 polaron configuration, which is one more electron than its Ti^{4+} intrinsic electron configuration (d^0).

Another qualitative difference that we can expect to see is a stronger degree of hybridization for e_g polarons with the $2p$ orbitals of the O ligands compared to t_{2g} polarons whose orbitals are pushed away from these O ligands. We have seen this already in our MnO_2 spinel calculations in Chapter 3, while here it is apparent in the case of $LaMnO_3$ as well. Whether this is a more general trend or more specific to Mn-O bonds [89] is beyond the scope of this work, but could be interesting to investigate in future studies.

A summary of our predictions is shown in Table 5.1. We will verify these predictions on a selected set of materials with these three structures in the following section. Our results will show that, while our calculations are consistent with the general trends predicted here, the assumptions we have made are elementary and do not include the plethora of complex interactions (including orbital ordering, geometrical distortions, and many more) that are invariably different for each individual material. However, we can now offer first order qualitative predictions on the relative coupling strength and adiabaticity (J) of polaron transport with just the crystal structure and the orbital configuration as input information.

5.3 Method

Calculation details for TiO_2 and Mn_2O_4 are as mentioned in Chapter 3. For $MgFe_2O_4$, we used $U_{\text{Fe}} = 4.5$ eV. This same value for U was also chosen for the model materials $MgMo_2O_4$ and $LaMoO_3$, as well as the perovskites $LaMnO_3$ and $LaCrO_3$. For $KCuF_3$ and $KNiF_3$, a higher value of $U = 6.6$ eV was used [139]. We used a $2 \times 2 \times 2$ k-point grid for the $2 \times 2 \times 3$ supercell of TiO_2 (24 Ti sites), a $3 \times 3 \times 3$ grid for the cubic or orthorhombic spinel unit cells (16 TM sites), and a $2 \times 2 \times 2$ grid for the $2 \times 2 \times 1$ supercell of orthorhombic perovskites (16 TM sites). Relaxation of the polaron ground state and transition state and calculation of the relevant properties E_a and $(2)J$ was done according to our previously stated techniques 2.5.

TiO_2 is nonmagnetic as it has zero available spin-polarizable electrons. The octahedral sites in spinels are typically antiferromagnetic with spin alignment along the 1D chains (each octahedral site has two same-spin and four opposite-spin neighbours). For the G-type AFM configuration in perovskites (see Fig. 5.10) it is not possible to calculate an adiabatic TS as the spins between neighbouring sites are opposite in sign. For these configurations we have used an approximate magnetic configuration which is detailed in the perovskite section below.

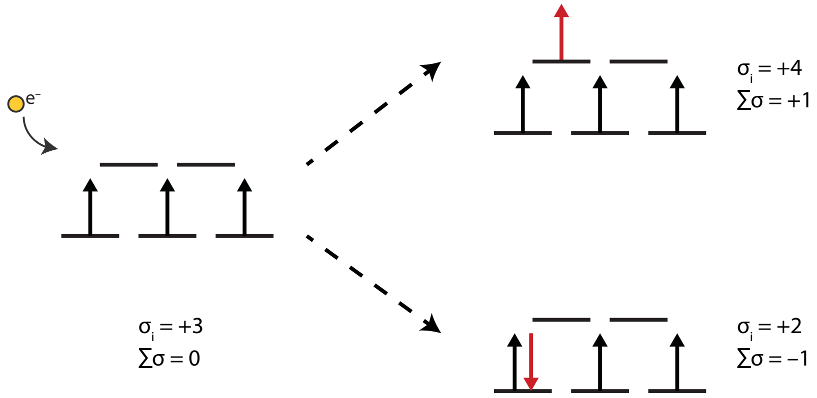

Figure 5.3: Local on-site (σ_i) spin configurations vs. net magnetic moment ($\sum \sigma$) in an example system consisting of sites arranged in antiferromagnetic t_{2g}^3 configurations. We only show the site where we plan to localize an additional electron on, which has an initial local magnetic moment of $+3$ (μ_B). After adding the extra electron on this site, it can either go to the spin up, e_g orbital to create a HS configuration, or it can go to the spin down t_{2g} orbital resulting in a LS configuration. If we constrain the net magnetic moment to either $+1$ or -1, and the difference in energy between the HS and LS configurations is not too large, we can force the electron into a particular spin configuration.

5.4 Results

5.4.1 $MgMo_2O_4$ and $LaMoO_3$: models for HS and LS polarons

We first start with two materials, spinel $MgMo_2O_4$ and perovskite $LaMoO_3$ that are somewhat hypothetical as there is little experimental evidence for their existence. The motivation behind investigating these two materials is that both have the same Mo^{3+} cations in the t_{2g}^3 configuration, but the way that their MoO_6 octahedra are connected are different (1L in $LaMoO_3$ vs. 2L in $MgMo_2O_4$). Adding an electron polaron then results in a d^4 configuration on the polaronic site. While molybdenum is a 4d TM and favours low spin configurations due to the higher crystal field splitting, the energy difference is such that it is still possible to force metastable HS states by carefully imposing certain constraints, and as such these materials can function as model materials to illustrate our theory by comparing different spin configurations in the same materials.

The high spin d^4 configuration is $t_{2g}^3 e_g^1$ with a net local magnetic moment of 4, while the low spin configuration is t_{2g}^4 with a net moment of 2. The procedure to force a higher energy spin state is thus to constrain the net spin to the desired value. For example, as illustrated in Fig. 5.3, if the polaronic site in an AFM system (net intrinsic spin of zero) is spin up (t_{2g}^3 in our case), the net spin when adding the electron will be $+1$ for a HS configuration and -1 for a LS configuration. Constraining the net spin to $+1$ will then force the extra electron to the e_g^1 state as long as the electron still prefers to localize on the same site. When this is successful, we can additionally induce JT distortions to make the electron go into either the d_{z^2} or $d_{x^2-y^2}$ orbital if they are not too far apart in energy.

Fig. 5.4 illustrates this procedure in $MgMo_2O_4$. The polaronic ground state is in a t_{2g} configuration where the extra electron goes to the first spin down channel in a LS configuration. By constraining the net spin, we can force this electron to go into either the d_{z^2} orbital (which is 0.22 eV higher in energy) or the $d_{x^2-y^2}$ orbital (0.36 eV higher in energy). Calculating the low spin t_{2g} TS gives us an activation energy of 97 meV and a relatively large coupling energy $J = 0.6$ eV. We can also calculate the TS for a polaron in the d_{z^2} state although we cannot further relax the initial linearly interpolated state. This TS has a much higher activation energy of 0.55 eV, as well as a much lower $J \approx 30$ meV. It is straightforward to explain the much lower coupling as the plotted charge density shows the d_{z^2} orbitals parallel to each other leading to little orbital overlap (Fig. 5.4).

For the $LaMoO_3$ perovskite in Fig. 5.5, the situation is very different. As outlined above, this is a 1L system where significant overlap can only be achieved by pointing the lobes of the d orbitals towards the shared O atom. The lowest energy polaronic state is again a t_{2g} state, but because there is little overlap ($J \approx 0$) between neighbouring t_{2g} states, we cannot calculate a clear transition state in DFT for this configuration. However, we can constrain the spin again and calculate a d_{z^2} HS polaronic state which is significantly higher in energy ($\Delta E = 0.5$ eV) but which does allow us to calculate a (linearly approximated) TS with an activation energy of E_a'

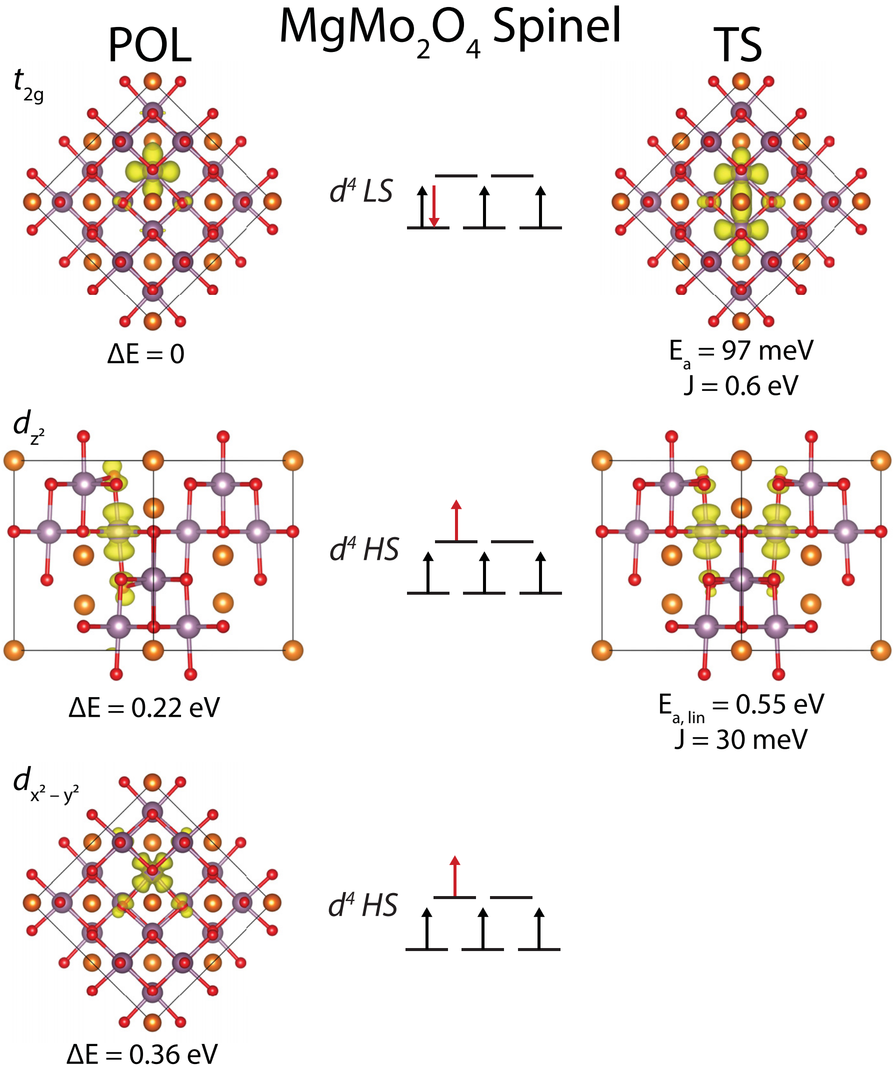

Figure 5.4: MgMo$_2$O$_4$ used as a model material to study both low spin (LS) and high spin (HS) orbital configurations in a 2L material. The top row shows the lowest energy configuration, which is low spin t_{2g}^4. However, it is possible to constrain the magnetic moment and obtain HS configurations that are higher in energy, as shown in the middle row (d_{z^2} orbitals) and bottom row ($d_{x^2-y^2}$). The t_{2g} and d_{z^2} transition states show remarkable differences in both their activation energies (E_a) and their adiabatic coupling (J).

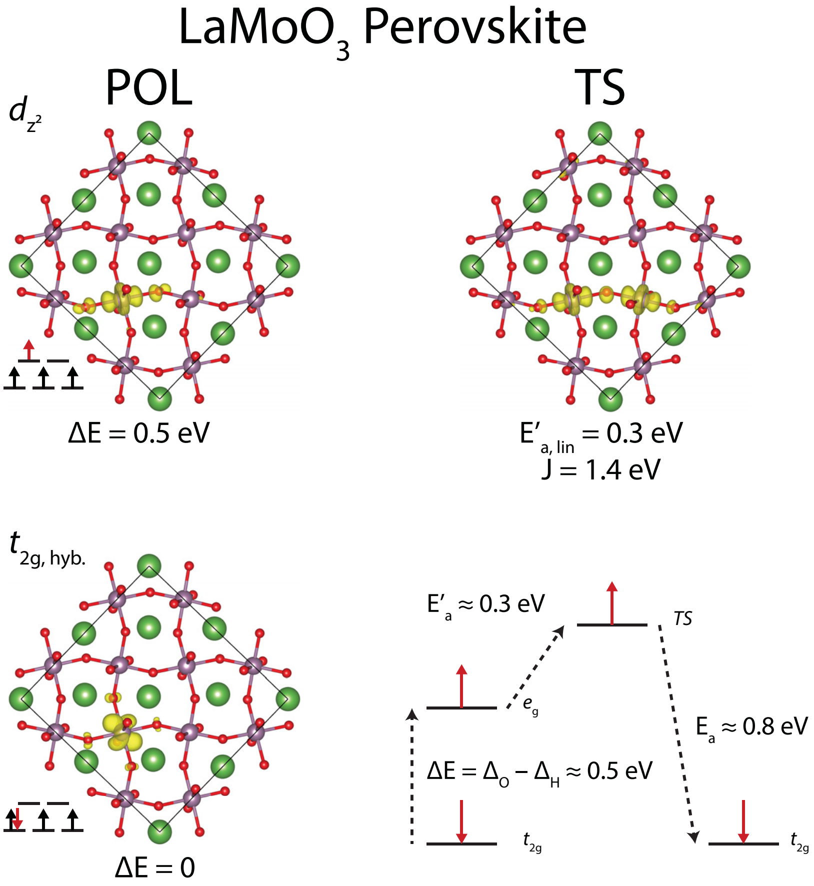

Figure 5.5: $LaMoO_3$, comparing the lowest energy (LS t_{2g}^4) configuration to the higher energy, d_{z^2} configuration. In contrast to $MgMo_2O_4$, we can only calculate an adiabatic TS with the higher energy d_{z^2} configuration, as the alignment of the d_{z^2} orbitals is required for electronic coupling between the sites ($J > 0$). However, an additional energy needs to be overcome to promote the polaron from the LS t_{2g} orbital to the HS e_g orbital in a LS material, as shown in the bottom right energy diagram, where Δ_O corresponds to the crystal field splitting and Δ_H is the Hund intrasite exchange energy.

= 0.3 eV and a high coupling energy of 1.4 eV. We argue that in order for adiabatic polaron transfer to occur in this material the polaron needs to be excited to the HS state first before it can overcome the HS adiabatic barrier E'_a, resulting in a total activation energy $E_a = E'_a + \Delta_E = 0.8$ eV. In general, we suspect that polarons in t_{2g} perovskites (and other materials in 1L directions) might have to overcome this Δ_E on top of E'_a before they can adiabatically transfer from one site to another. For perovskites this could be the case in any direction, whereas for other crystal structures it could lead to a strong anisotropy for polaronic hopping. As the calculated energies in $MgMo_2O_4$ and $LaMoO_3$ are not all from relaxed structures, we do not include these results in the final analysis but leave them here to outline the ideas discussed in this chapter.

5.4.2 *Rutile: TiO_2*

The rutile structure (Fig 5.1a) is a common structure for MX_2 (X = O or F) materials. The most common material with this structure is TiO_2 which is a wide bandgap semiconductor, while most other rutile compounds (VO_2, CrO_2, RuO_2) are either metallic [140] or have a metal-insulator transition at relatively low temperatures [141]. Focusing on the two types of octahedral connections, the rutile structure is characterized by MO_6 octahedra sharing edges (2L) along the c-axis and connect through the corners (1L) in other directions. Within this picture, we can understand qualitatively how TiO_2 is a semiconductor as the valence shell of Ti^{4+} cations is completely empty resulting in a distinct separation between the O $2p$ valence band and the Ti $3d$ conduction band. When we introduce electrons in the $3d$ orbitals as in VO_2, they will start interacting through their strong overlap along the c-axis.

Fig. 5.6 shows the POL and TS state in rutile TiO_2, in which the polaron assumes a d^1 (t^1_{2g}) occupancy. We have previously already done extensive calculations on polaronic properties in TiO_2, for which we refer to Chapter 3. Specific to this chapter, we note that the 2L connected c-direction is also the only direction in which we can

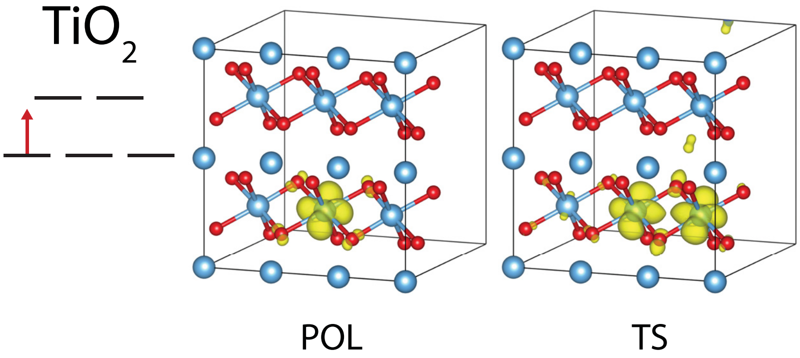

Figure 5.6: The polaron ground state (POL) and transition state (TS) in rutile TiO_2, and a diagram of the orbital configuration of its polaron (t_{2g}^1).

calculate an adiabatic TS for a t_{2g} polaron. This is in line with our predictions as the other directions are 1L connected. The calculated coupling energy in TiO_2 is 0.39 eV.

5.4.3 Spinels: $MgFe_2O_4$ and Mn_2O_4

Spinels (Fig 5.1b), generally formulated as AB_2X_4, are common structures for ternary oxides characterized by a cubic unit cell (there can be slight orthogonal distortions in practice) in which the X anions are in an FCC configuration, and the A (typically a large, alkali or alkaline earth element) and B (typically a transition metal) cations fill a fraction of the tetrahedral and octahedral holes, respectively. Typical applications for spinels include magnetic oxides (e.g. Fe_3O_4 [142]), catalysts (e.g. Co_3O_4 [39, 143]), and secondary batteries [36, 88, 107, 131, 144], one of which ($Li_xMn_2O_4$) we have investigated in Chapter 3.

Similar to rutile, the octahedra in spinels connect through common edges (2L). The specific tetrahedral arrangement of these octahedra lead to frustration in orbital ordering for partially filled t_{2g} configurations [145, 146] for which the details are beyond the scope of this work. As a result, we focus on either empty or half-full t_{2g} configurations in our two materials to simplify our calculations. $MgFe_2O_4$ [130] has Fe in its +3 oxidation state, i.e. it is in a $t_{2g}^3e_g^2$ configuration. Mn_2O_4, which does not have cations on the A site, has Mn^{4+} ions that are in a t_{2g}^3 configuration. As a

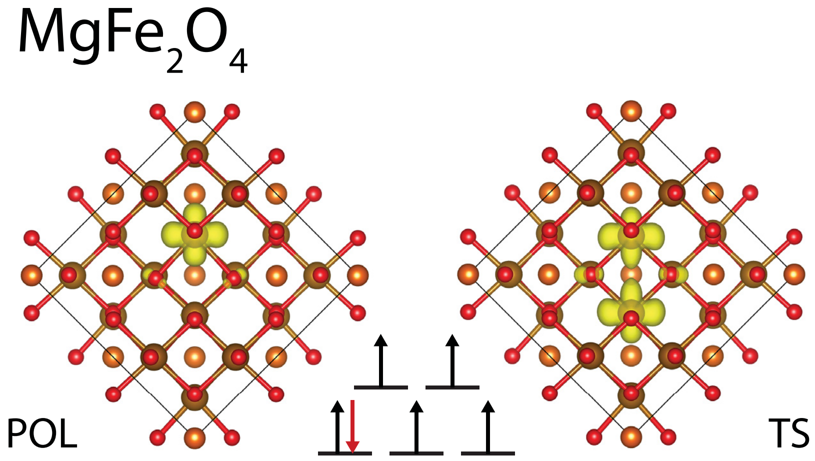

Figure 5.7: The polaron ground state (POL) and transition state (TS) in spinel $MgFe_2O_4$, and a diagram of the orbital configuration of its polaron ($t_{2g}^4 e_g^2$).

2L structure, we expect strong inter-site coupling between t_{2g} polarons. However, in the case of e_g polarons, there is still an adiabatic pathway through the M-O-M bonds angled at approximately 90°. We conduct a qualitative analysis on one example material for each of these situations.

Fig. 5.7 shows the POL and TS states for spinel $MgFe_2O_4$ (formal oxidation Fe^{3+}, $t_{2g}^3 e_g^2$) as well as the polaronic configuration ($t_{2g}^4 e_g^2$). Calculated energies are $E_a = 0.18$ eV, $J = 0.42$ eV. This is a prime example of a 2L t_{2g} adiabatic connection where the polaronic states are very atomic-like in nature. Furthermore, if we change the Fe-Fe distance by applying a uniform strain on the unit cell we can calculate the coupling parameter J to vary linearly with respect to the fifth power of the inverse Fe-Fe distance as shown in Fig. 5.8. This is a specific relation arising from the Slater-Koster two-center overlap integrals [81, 129] of atomic orbitals whose d atomic overlap should scale as $1/d_{M-M}^5$. This relation only applies to atomic orbitals, and thus we can conclude that the electronic state of the $MgFe_2O_4$ polaron is nearly atomic-like. In contrast, we could not calculate this relation in other investigated materials suggesting that polaronic states in most materials either deviate somewhat from pure atomic-like states, or they can hybridize with neighbouring p states and lose their atomic character. In general, increasing J by reducing the metal ion distances

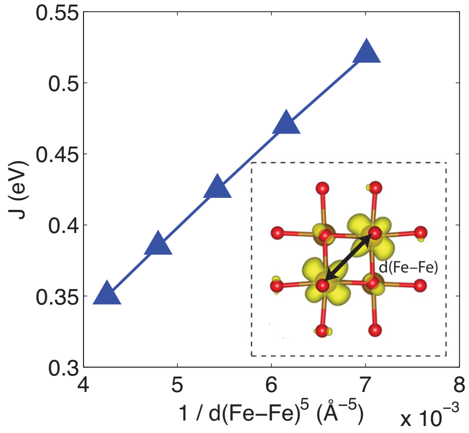

Figure 5.8: Linear behaviour of the coupling energy J with respect to the inverse Fe-Fe distance to the fifth power, shown in the inset. When the relevant orbitals are sufficiently atomic-like in nature, then their overlap can be described by the Slater-Koster tight binding two-center overlap integrals, which scale as $1/d^5_{Fe-Fe}$ for two overlapping d-orbitals.

through compressive strain could be an additional mechanism to engineer and improve polaron mobility, on top of the existing effect of strain on phonon modes which has also been shown to increase polaron mobilities [147].

In contrast, Fig. 5.9 shows the situation in spinel MnO_2 which is also extensively studied in Chapter 3. In this material (formal oxidation Mn^{4+}, t^3_{2g}), the polaronic state is in a $d_{x^2-y^2}$ configuration and shows strong hybridization with the $2p$ orbitals of the four planar O atoms. Already illustrated using its electronic structure in Chapter 3, here we show it more explicitly using the real space density. The transition state is also of $d_{x^2-y^2}$ character, with the overlap interaction along the two shared O atoms in a double TM-O-TM 90°-angled configuration. This overlap is considerable smaller compared to if the lobes were facing each other directly as in the $MgFe_2O_4$ case and shows up in the PDOS as $J = 80$ meV.

5.4.4 Perovskites: $LaMnO_3$, $LaCrO_3$, $KCuF_3$, and $KNiF_3$

Perovskites (Fig 5.1c) are a large family of ternary oxides with the general formula ABX_3 where A are typically large cations such as alkali/alkaline earth metals (Ca^{2+},

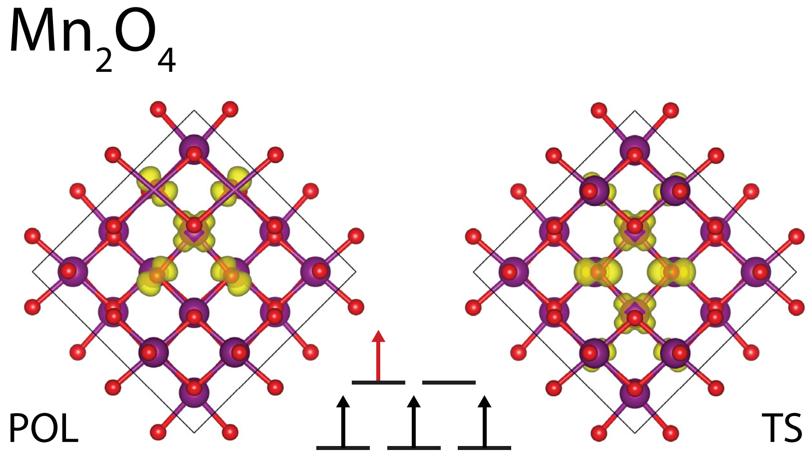

Figure 5.9: The polaron ground state (POL) and transition state (TS) in spinel $MgMn_2O_4$, and a diagram of the orbital configuration of its polaron ($t_{2g}^3e_g^1$).

Sr^{2+}, Ba^{2+}, etc.) or rare earth metals (La^{3+}, Gd^{3+}, etc.), B are typically transition metals, and X are anions such as O or F. The unit cell consists of an FCC lattice of X atoms forming an octahedron, the B cation in the center of the X octahedron, and the A cations at the corners. Amongst the many applications [132] of perovskite structured materials are solar cells [37, 133], fuel cells [134], and ferroelectrics [148].

The stereotypical perovskite unit cell is cubic although in many cases this will be distorted due to different ratios of the ionic radii [149], $GdFeO_3$ (GFO)-like tilting [150], and electronic JT-like distortions of the octahedra. All of these effects together can be found in lanthanum manganite ($LaMnO_3$), which as a result is one of the most extensively studied perovskites [123, 135, 136, 151, 152, 153] and has seen to exhibit remarkable properties such as giant magnetoresistance [154]. The magnetic structure is equally diverse, with orbital ordering [155, 156, 157, 158] and exchange interactions [79, 81, 123, 124, 135, 136, 137] determining [126, 127, 128] the magnetic structure of a particular perovskite material. The main antiferromagnetic (AFM) configurations resulting from these interactions are shown in Fig. 5.10. In order to calculate polaron transitions in G-type AFM configurations, we have assumed an approximate magnetic structure where the spins of 2×2 blocks are aligned but opposite to adjacent 2×2 blocks (labelled "2×2"-AFM in Fig. 5.10). This satisfies the Zener

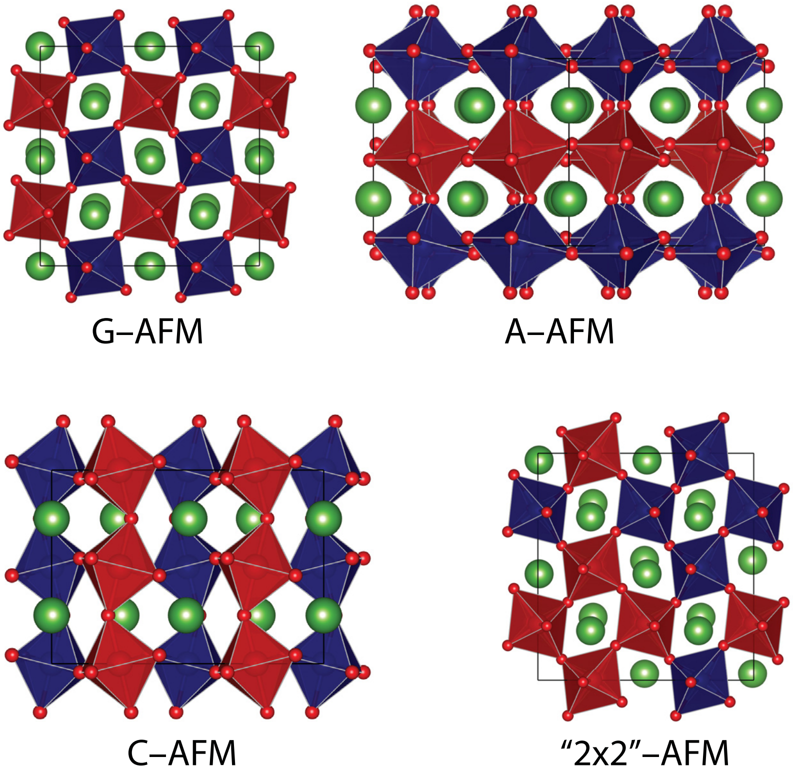

Figure 5.10: Different antiferromagnetic configurations in perovskites. The G-type structure (all six neighbours are of opposite spin) is the most common one, but certain orbital exchange interactions can result in the A-type (layered AFM, the four in-plane neighbours have the same spin while the two out-of-plane neighbours are of opposite spin) or C-type (column-like AFM, two same spin out-of-plane neighbours and four opposite spin in-plane neighbours) structures. The “2x2” AFM structure is an approximation used to calculate polaron transitions in G-type structures. As adiabatic transition requires spin alignment, this approximation aligns the neighbouring spins while trying to preserve a part of the symmetries of the G-type structure.

requirement [79] for double exchange while maintaining most of the symmetry and AFM character of the system.

In this study, we focus mainly on the effects of orbital interactions [81, 151, 159] and the 1L connected octahedra [79, 123] on polaron transitions [43, 137]. From the perspective of this chapter, the key property of the perovskite structure is that the octahedra are connected by the corners (1L), leading to cation-anion-cation exchange being the foremost interaction mechanism and restricting our conditions for adiabatic transfer. More specifically, this implies that occupancy of the higher energy e_g orbital

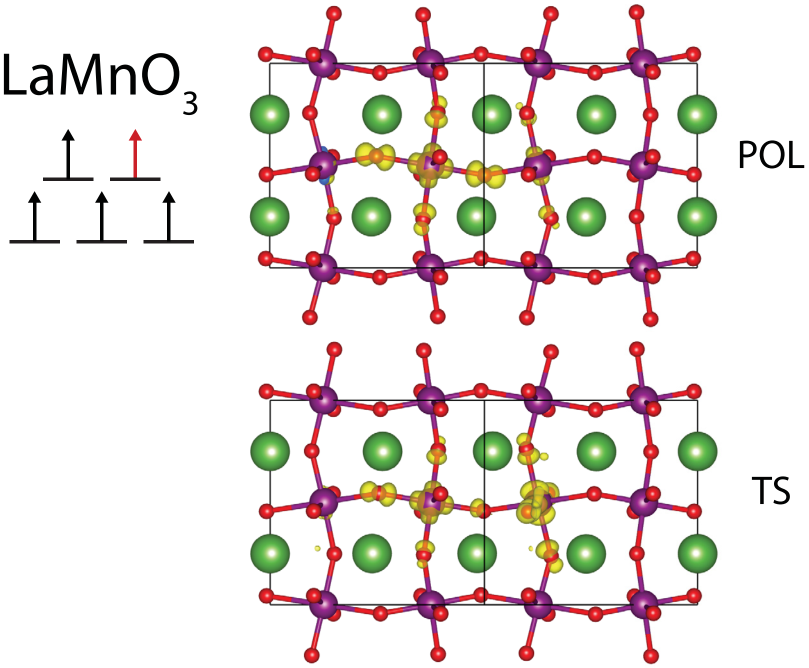

Figure 5.11: The polaron ground state (POL) and transition state (TS) in perovskite LaMnO$_3$, and a diagram of the orbital configuration of its polaron ($t_{2g}^3 e_g^2$).

configurations is required for adiabatic transfer as they point towards the shared O atom. Furthermore, the GFO-like octahedral tilting and other structural symmetry-reducing factors might also impact on polaronic transfer. We investigate these effects on polaronic transfer using a select few important perovskites (LaMnO$_3$ [135, 136, 151, 152, 153], LaCrO$_3$ [152, 153], KCuF$_3$ [139, 159, 160, 161], and KNiF$_3$ [162, 163]) and focus on the resulting trends in these materials.

LaMnO$_3$ and LaCrO$_3$

The intrinsic occupancy of the Mn^{3+} ion in LaMnO$_3$ leads to a HS d^4 configuration ($t_{2g}^3 e_g^1$) which is JT-active. Together with the collective GFO-tilting of the octahedra, this leads to a highly distorted structure with rotated octahedra that are elongated from the d^4 electron in the d_{z^2} orbital. A polaron (Fig. 5.11) will occupy the $d_{x^2-y^2}$ orbital on one site and increase its occupancy to d^5 ($t_{2g}^3 e_g^2$), effectively reducing the distortion of the octahedron. Because the octahedra are rotated with respect to each

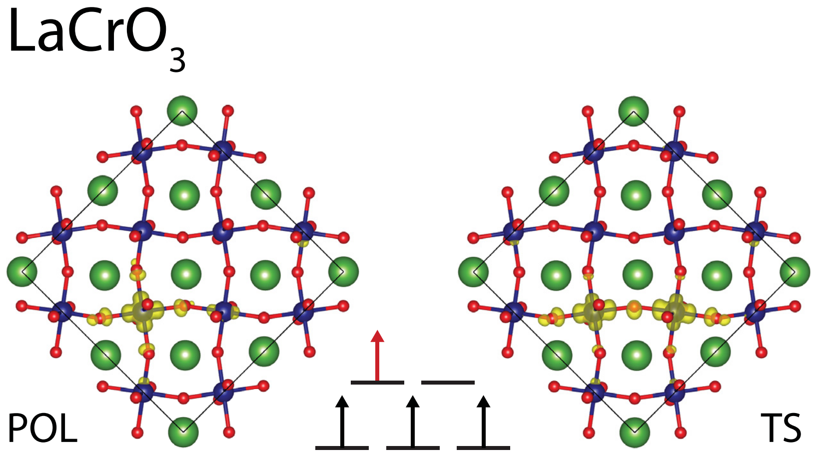

Figure 5.12: The polaron ground state (POL) and transition state (TS) in perovskite $LaCrO_3$, and a diagram of the orbital configuration of its polaron ($t_{2g}^3 e_g^1$).

other, the e_g orbitals of one site do not face those of its neighbouring site (Fig. 5.11), and this can be seen in the calculated TS where the $d_{x^2-y^2}$ orbitals are facing different directions. The resulting coupling energy is thus relatively low at $J = 0.16$ eV. The calculated activation energy E_a is 57 meV.

As with all lanthanum perovskites, $LaCrO_3$ has its Cr cations in the +3 oxidation state resulting in a half-filled t_{2g}^3 shell. It therefore exhibits little JT distortion although a slight GFO distortion remains. Adding a polaron introduces an electron to the $d_{x^2-y^2}$ orbital as shown in Fig. 5.12. Due to the smaller GFO distortion and lack of e_g^1 orbital ordering compared to $LaMnO_3$, the TS can assume a configuration with two d_{z^2} orbitals facing the shared O atom and increasing the coupling strength. $LaCrO_3$ is intrinsically a G-type AFM, so to calculate a transition state we have assumed the “2x2”-AFM magnetic structure instead. Calculated energies are $E_a = 66$ meV, $J = 0.40$ eV. As expected from the TS configuration, the coupling in $LaCrO_3$ is larger compared to the one calculated in $LaMnO_3$.

The chemical difference between $KCuF_3$ (Fig. 5.13) and $KNiF_3$ (Fig. 5.14) and perovskite oxides is that F^- anions replace the O^{2-} anions and the A cation is an alkali metal. This results in a formal oxidation state of +2 on the TM site as opposed to the +3 state in lanthanum and other rare earth perovskites and the +4 state in Sr

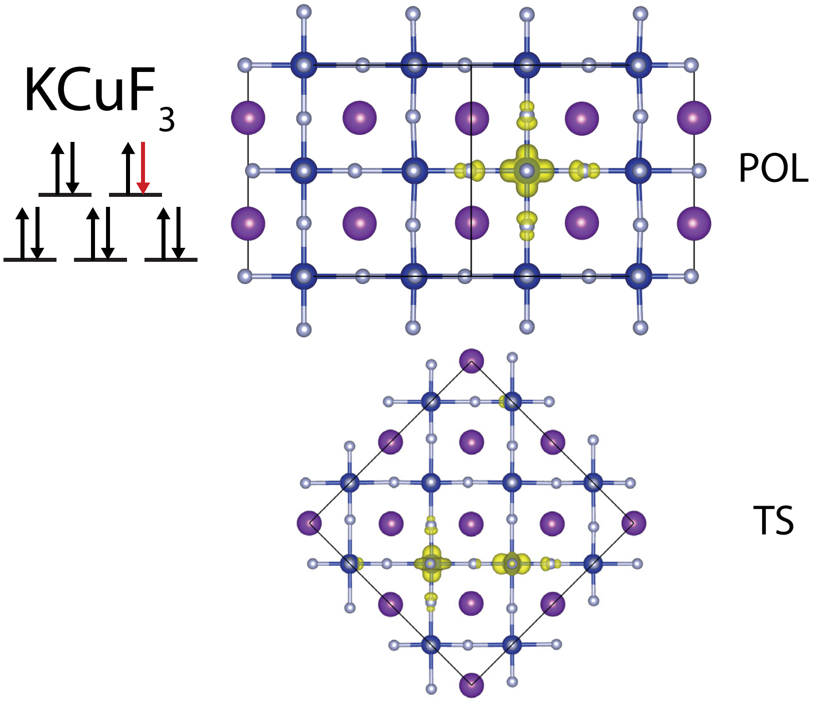

Figure 5.13: The polaron ground state (POL) and transition state (TS) in perovskite KCuF$_3$, and a diagram of the orbital configuration of its polaron ($t_{2g}^6 e_g^4$).

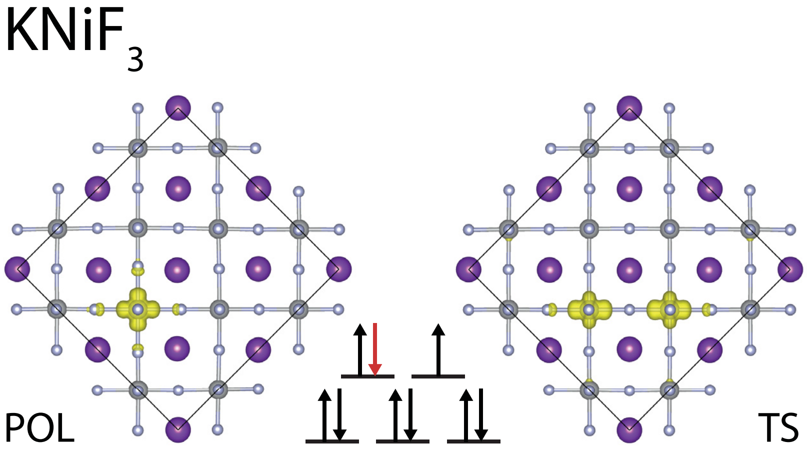

Figure 5.14: The polaron ground state (POL) and transition state (TS) in perovskite KNiF$_3$, and a diagram of the orbital configuration of its polaron ($t_{2g}^6 e_g^3$).

	Rutile	**Spinel**		**Perovskite**			
	TiO_2	$MgFe_2O_4$	Mn_2O_4	$LaMnO_3$	$LaCrO_3$	$KCuF_3$	$KNiF_3$
TM ox. state	Ti^{4+}	Fe^{3+}	Mn^{4+}	Mn^{3+}	Cr^{3+}	Cu^{2+}	Ni^{2+}
POL conf.	t_{2g}^1	$t_{2g}^4e_g^2$	$t_{2g}^3e_g^1$	$t_{2g}^3e_g^2$	$t_{2g}^3e_g^1$	$t_{2g}^6e_g^4$	$t_{2g}^6e_g^3$
TS conf.	t_{2g}	t_{2g}	$d_{x^2-y^2}$ (90°)	$d_{x^2-y^2}$ (A.S.)	d_{z^2}	d_{z^2} (A.S.)	d_{z^2}
E_a (meV)	225	176	250	57	66	152	212
J (eV)	0.39	0.42	0.08	0.16	0.40	0.12	0.22

Table 5.2: Summary of the polaron orbital configurations in the materials under investigation. Adding a polaron to a TM site acts as a reduction reaction and lowers its intrinsic oxidation state by 1. Also listed are the calculated properties of the polaronic TS, the activation energy E_a and the coupling energy J.

and other alkaline earth perovskites. Analogous to $LaMnO_3$, the single hole in the e_g shell of $KCuF_3$ leads to a JT distortion and an orbitally ordered ground state [159] with skewed octahedra. The structure of $KCuF_3$ however does not exhibit GFO-like distortions and is tetragonal. As the electron configuration of $KCuF_3$ is analogous to that of $LaMnO_3$, the electron configuration of $KNiF_3$ can be compared to that of $LaCrO_3$ although with a cubic structure in the case of $KNiF_3$.

Adding an electron polaron reduces the oxidation state by one. As shown in Figs. 5.13 and 5.14, the Cu polaronic site will have a completely filled d shell while the Ni site will have nine electrons in a $t_{2g}^6e_g^3$ configuration. Similar to $LaMnO_3$, the orbital ordering in $KCuF_3$ results in a TS with d_{z^2} orbitals that are not facing each other. This leads to an activation energy E_a of 0.15 eV and a coupling J of 0.12 eV. In contrast, the E_a of $KNiF_3$ is 0.21 eV but its J is higher at 0.22 eV, again likely due to the TS having d_{z^2} orbitals that face each other.

5.5 Summary

In this chapter, we have attempted to develop a set of qualitative guidelines for predicting adiabatic polaron transport properties based on principles from exchange interaction, requiring only the TM orbital occupancy and crystal structure as input.

The framework of exchange interaction discussed here has been developed in the 50's and is already widely applied to the materials that we have studied. Adding an additional TM-localized electron is therefore a simple extension of these ideas applied to our particular case of TM-centered polarons. Incidentally, the addition of this small polaron provides a convenient tool to study exchange interaction as all the physics happens at the Fermi energy and such polarons are inherently localized to specific sites.

Our calculations were qualitatively in line with these predictions despite deviations arising from effects such as orbital ordering in $LaMnO_3$ and $KCuF_3$ that affected the quantitative results but not the general picture. We therefore conclude that this model can predict qualitatively whether it is possible to calculate an adiabatic, $J > 0$, transition state, and what the relative magnitude of J should be. This exchange parameter J plays an important role as it connects the initially spatially degenerate polaronic ground states to a single, adiabatic transition state (see Ch. 2). Without this single state, any perturbation (even numerical inaccuracies) will lift this degeneracy and lead to the system to favour filling one site over another, in contrast to the $\left(\frac{1}{2}, \frac{1}{2}\right)$ density distribution that one would expect from such a transition state. This is the main cause for not being able to calculate the adiabatic TS in systems that have $J \approx 0$ in DFT.

However, we must emphasize the limits under which these predictions hold. Most importantly, we only consider ideal, or close to ideal structures where the M-O-M bonds are close to either 90° or 180° and where the exchange happens under close to ideal circumstances. In practice, there are many other structures that are far from these ideal 1L/2L connections, and the predicted properties in those cases will likely fall somewhere in between the two extreme cases that we have considered. An example is the olivine structure on which we have performed our (Li)$FePO_4$ calculations. The octahedra in this structure are 1L connected, but it is possible to calculate an adiabatic TS for Fe^{2+} ($t_{2g}^4 e_g^2$) polarons with a significant calculated J of $\sim$0.2 eV in this material. Looking closer at the olivine structure, we can see that the octahedra are tilted in such a way that allows both t_{2g} and e_g polarons to exhibit overlap. Additionally, the only process considered here is polaron transport through TM centers. There are invariably many other conduction processes, such as hole polaron transport through O $2p$ centers [42, 47, 57], that will also exist in these materials. Thus even if $J \approx 0$ for TM-TM polaron hopping it is not straightforward to apply these predictions to measured conductivities.

6

Conclusion

I have performed systematic first principles studies of polaronic behaviour in a selection of transition metal oxides relevant to applications in renewable energy technologies. The technologically relevant materials that I have studied include the battery cathode materials $LiFePO_4$ and $LiMn_2O_4$ and the photovoltaic materials TiO_2 and Fe_2O_3. While I have studied the perovskite materials $LaMnO_3$, $LaCrO_3$, $KCuF_3$, and $KNiF_3$ more as model materials to investigate specific trends, the materials are relevant on their own. In particular, $MgFe_2O_4$ and $LaCrO_3$ are catalytic materials, and $LaMnO_3$ and $KCuF_3$ exhibit complex interplay between the various orbital ordering, correlation, and magnetoresistive effects and are thus amongst the most widely studied strongly correlated materials in the field.

My calculations were performed using methods from well established density functional theory, and I have investigated these methods more in-depth when applying them to calculations of polaronic properties. More specifically, I have shown that DFT+U projection strongly affects the calculated polaronic properties, in effect adding a second, mathematical, parameter alongside the single physical U-parameter. This might have implications on not only polaronic properties in particular, but also other Mott-Hubbard influenced properties in general. As DFT+U is a widely used technique to incorporate strong on-site correlation in a computationally efficient manner, it behooves us to maintain a consistent DFT+U projection when comparing calculation results. Furthermore, I have shown the benefits of the NEB method to relax adiabatic transition states, often resulting in a better approximation to the activation energy. Using ab initio molecular dynamics, I was able to simulate the dynamics of polaron hopping in a way that is consistent with the static barrier calculations from NEB. Therefore, it seems plausible to extend the use of AIMD to study other polaronic properties such as polaron formation dynamics.

I introduced a two-site hopping model to better connect our DFT results to the polaron hopping picture, especially with regards to adiabaticity and the importance of the coupling parameter J. Together with considerations from crystal symmetry and elements from exchange theory, this has allowed me to understand qualitatively under what conditions an adiabatic TS is likely to form, and how strong its coupling energy J should be. The concept of adiabaticity aligns with the principles of DFT, which is inherently a ground state, adiabatic theory, and combining the ideas has enabled me to understand situations where we were unable to calculate a transition state in DFT even though the ionic positions were perfectly interpolated. Lastly, I have applied these concepts to form a qualitative framework with which we can predict adiabatic polaron transport properties based on just the orbital configurations and the crystal structure of the material, and I have used several model materials from three structural families to verify these predicted trends.

The limits of the theory and its approximations that I have used are as follows. First of all, there are no explicit electron-phonon terms in the Hamiltonian after the Born-Oppenheimer approximation while they must be taken into account for a full description of polaronic behaviour. There are efforts beyond the BO approximation that can calculate these electron-phonon terms [33], and this is one potential avenue for future studies. Another limit of DFT that I will reiterate here is that it is a ground state, adiabatic theory, and any properties calculated from unoccupied energy levels (the band gap, polaron state, and coupling term) lack a true physical meaning even if they can be very close to experimental values. One method that can explicitly treat such excited states is time dependent DFT (TD-DFT) [164], and could be another opportunity for future extensions.

The next step after having gained sufficient understanding of the problem would be to find ways, within the same model, to engineer and improve the properties of the system. In my case of polaronic hopping, an important goal would be to find ways to improve the conductivity in polaronic materials. This is beyond the scope of this thesis, but I will outline some successful avenues that have taken into account the limitations of polaronic materials. Specifically, the fundamental differences between band-like semiconductors and polaronic materials limit the benefits of classic semiconductor engineering techniques such as charge doping and band gap engineering. When charge doping a polaronic material, the result is an increase in polarons in the material which contribute far less to the conductivity, and very high doping is required to achieve a significant increase in conductivity [154]. Similarly, reducing the band gap releases a large number of free charge carriers from the Fermi distribution, however these will also fall into polaronic states. Therefore, we need to look in different directions if we were to engineer the conductivity in a polaronic material. One such way is to strain the material, which lowers the energy of the local structural distortion and therefore lowers the activation energy [147]. Another idea would be to add dopants that act to lower the activation energy.

My approach is based on a computational materials design framework, in which we first choose a model (DFT+U, Hybrid DFT) that can accurately and consistently reproduce the properties that we are investigating (polarons). Then, we can use this model to investigate and predict the properties of novel materials from a "materials by design" philosophy. If we have a good predictive model, we can use it to point out trends and directions for experimental research, and the eventual goal would be to save considerable experimental effort in the process. I remark here that my calculations are quantitatively comparable to experimentally measured values, in particular for the activation energy in Fe_2O_3 and the gap state eigenenergies in TiO_2 and Fe_2O_3. This suggests that this model could be suitable for quantitative predictions in other materials with similar electronic behaviour.

A

Full DFT+U projection results

For additional comparison, we performed polaron hopping barrier (E_a) calculations with the plane-wave DFT code Abinit [100, 101]. The parameters for total energy calculations in Abinit were chosen to match VASP settings as closely as possible: the GGA-PBE functional was used, and the smearing temperature, supercells, k-points, and U_{eff} values were identical to those used in our VASP calculations. Additionaly, the ionic positions for both the transition states and ground states are the same as those relaxed using VASP. PAW potentials for non-transition metal elements were taken from Abinit's JTH-1.0 library [165]. For the transition metals (Fe, Mn, Ti), we tested multiple PAW potentials, each having different r_{PAW} and different numbers of electrons in the valence. We tested PAW potentials from the Abinit JTH-1.0 library as well as PAW potentials from the <2013 library on the Atompaw website [166]. Atompaw [167] is a popular PAW generation code and the pseudopotentials published with it are expected to be trustworthy. The atompaw potentials were rebuilt using Atompaw version 4 for compatibility with Abinit. For Fe, we tested one additional PAW potential from an older version of Abinit's JTH library (JTH-0.1) that has only 8 electrons in the valence. This PAW potential was also rebuilt with Atompaw version 4.

The implementation of the +U on-site projection in Abinit [71] differs slightly from the implementation in VASP [50], and the Abinit results appear to show less potential dependent variation. However, further potential database development is required to verify such improvements.

	Z_{val}	r_{PAW} (a.u.)
Ti	4	2.8
Ti_pv	10	2.5
Ti_sv	12	2.3
Ti_sv_GW	12	2.0
Ti_h	12	1.9
Abinit_JTH-1.0_PAW Ti	12	2.3
Atompaw_PAW Ti	12	2.3
Mn	7	2.3
Mn_pv	13	2.3
Mn_sv_GW	15	2.0
Mn_sv	15	1.95
Abinit_JTH-1.0_PAW Mn	15	2.1
Atompaw_PAW Mn	15	1.9
Fe	8	2.3
Fe_pv	14	2.2
Fe_sv_GW	16	2.0
Fe_sv	16	1.9
Abinit-2009-v8_PAW Fe	8	2.3
Abinit_JTH-1.0_PAW Fe	16	2.1
Atompaw_PAW Fe	16	2.1

Table A.1: List of the potentials used in this study with their different valencies and PAW augmentation radii. Additional potentials used in our Abinit calculations are also listed here.

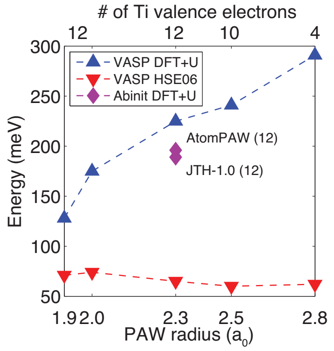

Figure A.1: Comparison of TiO_2 activation energies (E_a) calculated with VASP (red and blue) and Abinit (magenta). The Abinit potentials and their valences are labeled next to their energies.

TiO_2	DFT+U					
	Z_{val}	r_{PAW} (a.u.)	E_g (eV)	E_p (eV)	E_{form} (meV)	E_a (meV)
Ti	4	2.8	2.31	1.51	460	291
Ti_pv	10	2.5	2.41	1.29	389	241
Ti_sv	12	2.3	2.43	1.20	359	225
Ti_sv_GW	12	2.0	2.39	0.94	248	175
Ti_h	12	1.9	2.35	0.74	138	128
Abinit_JTH-1.0_PAW Ti	12	2.3				189
Atompaw_PAW Ti	12	2.3				196
	HSE06					
Ti	4	2.8	3.46	1.04	207	62
Ti_pv	10	2.5	3.66	1.02	215	60
Ti_sv	12	2.3	3.72	1.04	222	65
Ti_sv_GW	12	2.0	3.74	1.07	239	74
Ti_h	12	1.9	3.74	1.06	232	71
	Experiment		3 [102]	0.7 ± 0.1 [40]		

Table A.2: List of calculated energies in TiO_2.

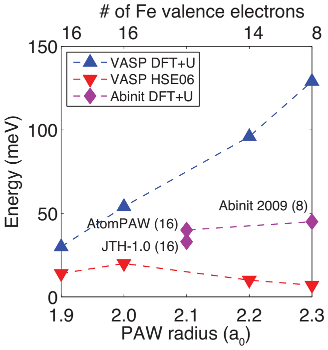

Figure A.2: Comparison of Fe_2O_3 activation energies (E_a) calculated with VASP (red and blue) and Abinit (magenta). The Abinit potentials and their valences are labeled next to their energies.

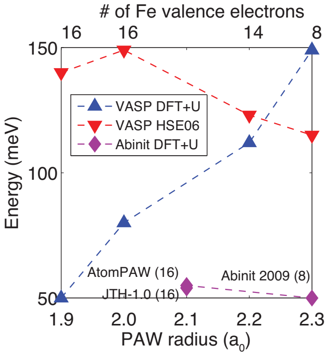

Figure A.3: Comparison of $FePO_4$ activation energies (E_a) calculated with VASP (red and blue) and Abinit (magenta). The Abinit potentials and their valences are labeled next to their energies.

Fe_2O_3	DFT+U					
	Z_{val}	r_{PAW} (a.u.)	E_g (eV)	E_p (eV)	E_{form} (meV)	E_a (meV)
Fe	8	2.3	2.36	1.07	460	129
Fe_pv	14	2.2	2.36	0.93	388	96
Fe_sv_GW	16	2.0	2.39	0.75	296	54
Fe_sv	16	1.9	2.33	0.62	240	30
Abinit-2009-v8_PAW Fe	8	2.3				45
Abinit_JTH-1.0_PAW Fe	16	2.1				33
Atompaw_PAW Fe	16	2.1				40
	HSE06 $\alpha = 25\%$					
Fe	8	2.3	3.50	1.30	381	75
Fe_pv	14	2.2	3.55	1.33	409	10
Fe_sv_GW	16	2.0	3.61	1.38	408	20
Fe_sv	16	1.9	3.62	1.35	423	14
	HSE06 $\alpha = 12\%$					
Fe	8	2.3	2.04			
Fe_pv	14	2.2	2.06			
Fe_sv_GW	16	2.0	2.11			
Fe_sv	16	1.9	2.11			
	Experiment		2 [104]	0.7 [48]		120 [48]

Table A.3: List of calculated energies in Fe_2O_3.

$FePO_4$	DFT+U					
	Z_{val}	r_{PAW} (a.u.)	E_g (eV)	E_p (eV)	E_{form} (meV)	E_a (meV)
Fe	8	2.3	1.85	0.61	506	149
Fe_pv	14	2.2	1.86	0.46	481	112
Fe_sv_GW	16	2.0	1.92	0.30	557	80
Fe_sv	16	1.9	1.87	0.25	486	50
Abinit-2009-v8_PAW Fe	8	2.3				50
Abinit_JTH-1.0_PAW Fe	16	2.1				54
Atompaw_PAW Fe	16	2.1				55
	HSE06					
Fe	8	2.3	3.32	0.66	262	115
Fe_pv	14	2.2	3.38	0.69	268	123
Fe_sv_GW	16	2.0	3.47	0.76	301	149
Fe_sv	16	1.9	3.47	0.73	279	140

Table A.4: List of calculated energies in $FePO_4$.

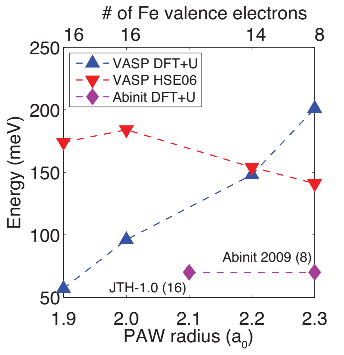

Figure A.4: Comparison of $LiFePO_4$ activation energies (E_a) calculated with VASP (red and blue) and Abinit (magenta). The Abinit potentials and their valences are labeled next to their energies.

$LiFePO_4$	DFT+U						
	Z_{val}	r_{PAW} (a.u.)	E_{C-2+} (eV)	E_{C-V} (eV)	E_p (eV)	E_{form} (meV)	E_a (meV)
Fe	8	2.3	3.74	4.13	2.74	309	201
Fe_pv	14	2.2	3.59	4.14	2.76	185	148
Fe_sv_GW	16	2.0	3.29	4.07	2.64	72	96
Fe_sv	16	1.9	3.17	4.04	2.66	19	57
Abinit-2009-v8_PAW Fe	8	2.3					70
Abinit_JTH-1.0_PAW Fe	16	2.1					70
	HSE06						
Fe	8	2.3	4.15	5.41	3.12	219	141
Fe_pv	14	2.2	4.13	5.41	3.08	283	154
Fe_sv_GW	16	2.0	4.18	5.44	3.02	354	184
Fe_sv	16	1.9	4.14	5.44	3.02	341	174
	Experiment		4 [56]				

Table A.5: List of calculated energies in $LiFePO_4$.

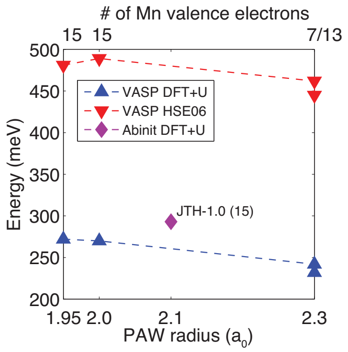

Figure A.5: Comparison of MnO_2 activation energies (E_a) calculated with VASP (red and blue) and Abinit (magenta). The Abinit potentials and their valences are labeled next to their energies.

MnO$_2$	DFT+U					
	Z_{val}	r_{PAW} (a.u.)	E_g (eV)	E_p (eV)	E_{form} (meV)	E_a (meV)
Mn	7	2.3	2.04	0.80	381	232
Mn_pv	13	2.3	2.12	0.81	395	242
Mn_sv_GW	15	2.0	2.26	0.89	440	270
Mn_sv	15	1.95	2.24	0.90	433	272
Abinit_JTH-1.0_PAW Mn	15	2.1				293
	HSE06					
Mn	7	2.3	3.48	1.84	709	445
Mn_pv	13	2.3	3.56	1.85	704	462
Mn_sv_GW	15	2.0	3.67	1.92	729	489
Mn_sv	15	1.95	3.64	1.90	712	481
	Experiment		3 [108]	1.2 [107], 1.63/2.00 [108]		

Table A.6: List of calculated energies in MnO$_2$.

B

Calculation details of semi-core states in $LiFePO_4$

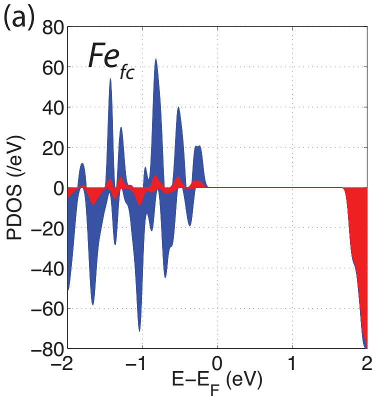

Figure B.1: Density of states for Fe_{fc} vs. Fe_{sc} potentials. Projected O 2*p* (blue) and Fe 3*d* (red) density of states around the band gap (1.9 eV) in $FePO_4$ calculated with (a) Fe_{fc} and (b) Fe_{sc} PAW potentials. There is a difference of 10 meV between the two band gaps.

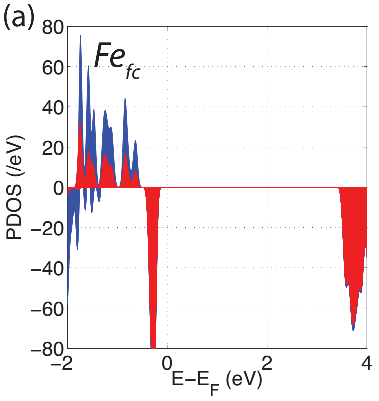

Figure B.2: Density of states for Fe_{fc} vs. Fe_{sc} potentials. Projected O 2*p* (blue) and Fe 3*d* (red) density of states around the band gap (4.1 eV) in $LiFePO_4$ calculated with (a) Fe_{fc} and (b) Fe_{sc} PAW potentials. While the polaronic state has moved up within the band gap, the difference of 50 meV between the band gaps is again small.

B.1 WIEN2k All-electron calculation details

Calculations in WIEN2k were matched as close as possible to the calculations done in VASP, using polaronic ground state (POL) and transition state (TS) structures taken from VASP calculations, a PBE+U functional with $U = 4.3$ eV, and R_{MT} for Fe set to 2.3 a_0 for comparisons with the $\mathrm{Fe}_{\mathrm{fc}}$ PAW potential, and $R_{\mathrm{MT}} = 1.9\ a_0$ for comparisons with the $\mathrm{Fe}_{\mathrm{sc}}$ PAW potential. The basis set size was chosen according to $R_{\mathrm{MT}} \times K_{\mathrm{max}} = 6.0$.

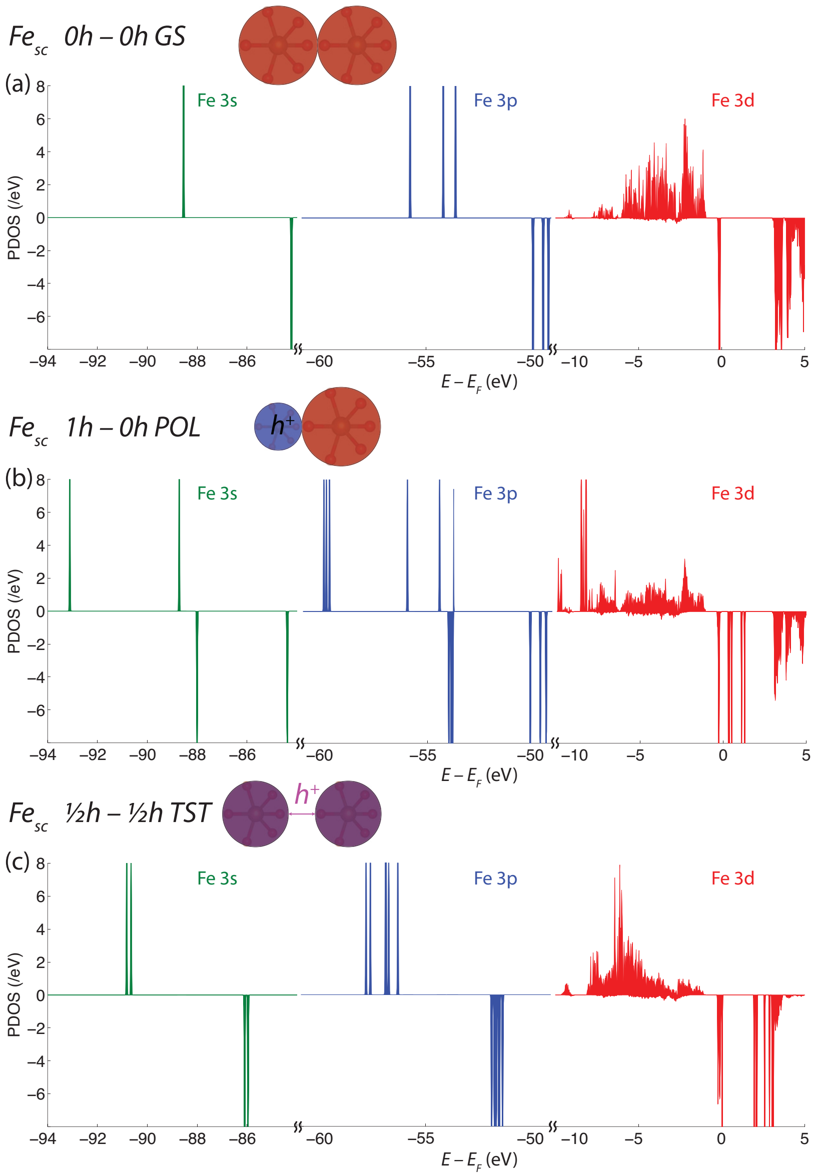

Figure B.3: Relaxation of semi-core states in $LiFePO_4$. Projected density of states (PDOS) for the two Fe atoms taking part in the $LiFePO_4$ hole transfer process for (a) the intrinsic ground state configuration ("GS"), (b) the polaronic ground state configuration ("POL"), and (c) the transition state ("TST").

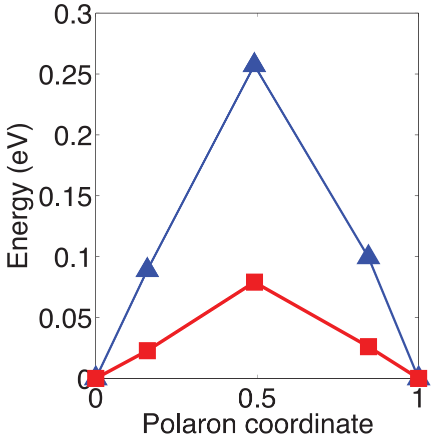

Figure B.4: Activation energy for nearest-neighbor hole polaron hopping in $LiFePO_4$ calculated with both 8-valence $3d^6 4s^2$ (Fe_{fc} blue upright triangles) and 16-valence $3s^2 3p^6 3d^6 4s^2$ (Fe_{sc} red squares) Fe potentials. Barrier for Fe_{fc}: 257 meV. Barrier for Fe_{sc}: 79 meV.

BIBLIOGRAPHY

[1] Zi Wang, Casey Brock, Amina Matt, and Kirk H Bevan. Implications of the DFT+U method on polaron properties in energy materials. Phys. Rev. B, 96(12):125150, 2017.

[2] Zi Wang and Kirk H Bevan. Exploring the impact of semicore level electronic relaxation on polaron dynamics: An adiabatic ab initiostudy of FePO4. Phys. Rev. B, 93(2):024303–10, January 2016.

[3] Michael R. Wasielewski. Photoinduced electron transfer in supramolecular systems for artificial photosynthesis. Chem. Rev., 92(3):435–461, 1992.

[4] Devens Gust, Thomas A. Moore, and Ana L. Moore. Solar Fuels via Artificial Photosynthesis. Acc. Chem. Res., 42(12):1890–1898, 2009.

[5] Yasuhiro Tachibana, Lionel Vayssieres, and James R Durrant. Artificial photosynthesis for solar water-splitting. Nature Photon., 6(8):511–518, 2012.

[6] Scott C Warren, Kislon Voïtchovsky, Hen Dotan, Celine M Leroy, Maurin Cornuz, Francesco Stellacci, Cécile Hébert, Avner Rothschild, and Michael Grätzel. Identifying champion nanostructures for solar water-splitting. Nature Mater., 12(9):842–849, 2013.

[7] K Mizushima, PC Jones, PJ Wiseman, and John B Goodenough. LixCoO2 (0 $< x \leq 1$): A new cathode material for batteries of high energy density. Mater. Res. Bull., 15(6):783–789, 1980.

[8] Akshaya K Padhi, KS Nanjundaswamy, and John B Goodenough. Phospho-olivines as positive-electrode materials for rechargeable lithium batteries. J. Electrochem. Soc, 144(4):1188–1194, 1997.

[9] John B Goodenough and Arumugam Manthiram. A perspective on electrical energy storage. MRS Commun., 4(04):135–142, December 2014.

[10] Eric W McFarland and Horia Metiu. Catalysis by doped oxides. Chem. Rev., 113(6):4391–4427, 2013.

[11] Nevill F Mott. The basis of the electron theory of metals, with special reference to the transition metals. Proc. Phys. Soc. Sect. A, 62(7):416, 1949.

[12] John Hubbard. Electron correlations in narrow energy bands. Proc. R. Soc. Lond. A, 276(1365):238–257, 1963.

[13] I G Austin and N F Mott. Polarons in crystalline and non-crystalline materials. Advances in Physics, 18(71):41–102, January 1969.

[14] LD Landau. Uber die bewegung der elektronen in kristalgitter. Phys. Z. Sowjetunion, 3:644–645, 1933.

[15] Th Holstein. Studies of polaron motion: Part I. The molecular-crystal model. Ann. Phys., 8(3):325–342, 1959.

[16] Th Holstein. Studies of polaron motion: Part II. The “small” polaron. Ann. Phys., 8(3):343–389, 1959.

[17] A L Shluger and A M Stoneham. Small Polarons in Real Crystals - Concepts and Problems. J. Phys. Condens. Matter, 5(19):3049–3086, 1993.

[18] A M Stoneham, J Gavartin, A L Shluger, A V Kimmel, D Muñoz Ramo, H M Rønnow, G Aeppli, and C Renner. Trapping, self-trapping and the polaron family. J. Phys. Condens. Matter, 19(25):255208–23, May 2007.

[19] Alan J Heeger, S Kivelson, JR Schrieffer, and W-P Su. Solitons in conducting polymers. Rev. Mod. Phys., 60(3):781, 1988.

[20] C Deibel, A Baumann, and V Dyakonov. Polaron recombination in pristine and annealed bulk heterojunction solar cells. Appl. Phys. Lett., 93(16):163303–4, 2008.

[21] F X Morrissey, J G Mance, A D Van Pelt, and S L Dexheimer. Femtosecond dynamics of exciton localization: self-trapping from the small to the large polaron limit. J. Phys. Condens. Matter, 25(14):144204–12, March 2013.

[22] P. H.-L. Sit, Matteo Cococcioni, and Nicola Marzari. Realistic Quantitative Descriptions of Electron Transfer Reactions: Diabatic Free-Energy Surfaces from First-Principles Molecular Dynamics. Phys. Rev. Lett., 97:028303, Jul 2006.

[23] R A Marcus. On the Theory of Oxidation-Reduction Reactions Involving Electron Transfer. I. J. Chem. Phys., 24(5):966–14, 1956.

[24] Marshall D Newton, Hitoshi Sumi, Spiros S Skourtis, David N Beratan, Daniël Vanmaekelbergh, Sharon Hammes-Schiffer, Piotr Piotrowiak, John F Endicott, Marye Anne Fox, Ann-Margret Andersson, et al. Electron transfer in chemistry. 2001.

[25] Herbert Fröhlich. Electrons in lattice fields. Adv. Phys., 3(11):325–361, 1954.

[26] P E Blöchl. Projector augmented-wave method. Phys. Rev. B, 50(24):17953–17979, December 1994.

[27] G. Kresse and D. Joubert. From ultrasoft pseudopotentials to the projector augmented-wave method. Phys. Rev. B, 59:1758–1775, Jan 1999.

[28] V I Anisimov, F Aryasetiawan, and A I Lichtenstein. First-principles calculations of the electronic structure and spectra of strongly correlated systems: the LDA+U method. J. Phys. Condens. Matter, 9(4):767–808, 1997.

[29] Carlo Adamo and Vincenzo Barone. Toward reliable density functional methods without adjustable parameters: The PBE0 model. J. Chem. Phys., 110(13):6158–6170, 1999.

[30] Thomas Maxisch, Fei Zhou, and Gerbrand Ceder. Ab initio study of the migration of small polarons in olivine LixFePO4 and their association with lithium ions and vacancies. Phys. Rev. B, 73(10):104301, March 2006.

[31] Gopi Krishna Phani Dathar, Daniel Sheppard, Keith J Stevenson, and Graeme Henkelman. Calculations of Li-Ion Diffusion in Olivine Phosphates. Chem. Mater., 23(17):4032–4037, September 2011.

[32] Vladimir Timoshevskii, Zimin Feng, Kirk H. Bevan, John Goodenough, and Karim Zaghib. Improving Li2O2 conductivity via polaron preemption: An ab initio study of Si doping. Appl. Phys. Lett., 103(7):073801, 2013.

[33] Zimin Feng, Vladimir Timoshevskii, Alain Mauger, Christian M. Julien, Kirk H. Bevan, and Karim Zaghib. Dynamics of polaron formation in Li_2O_2 from density functional perturbation theory. Phys. Rev. B, 88:184302, 2013.

[34] Zimin Feng, Chisu Kim, Ashok Vijh, Michel Armand, Kirk H. Bevan, and Karim Zaghib. Unravelling the role of Li2S2 in lithium-sulfur batteries: A first principles study of its energetic and electronic properties. J. Power Sources, 272:518 – 521, 2014.

[35] Vladimir Timoshevskii, Zimin Feng, Kirk H. Bevan, and Karim Zaghib. Emergence of Metallic Properties at LiFePO4 Surfaces and LiFePO4/Li2S Interfaces: An Ab Initio Study. ACS Appl. Mater. Interfaces, 7(33):18362–18368, 2015.

[36] Miao Liu, Ziqin Rong, Rahul Malik, Pieremanuele Canepa, Anubhav Jain, Gerbrand Ceder, and Kristin A Persson. Spinel compounds as multivalent battery cathodes: a systematic evaluation based on ab initio calculations. Energy Environ. Sci, 8:964–974, March 2015.

[37] Guangda Niu, Xudong Guo, and Liduo Wang. Review of recent progress in chemical stability of perovskite solar cells. J. Mater. Chem. A, 3(17):8970–8980, 2015.

[38] Meng Ni, Michael KH Leung, Dennis YC Leung, and K Sumathy. A review and recent developments in photocatalytic water-splitting using TiO2 for hydrogen production. Renew. Sustainable Energy Rev., 11(3):401–425, 2007.

[39] M Hamdani, R N Singh, and P Chartier. Co3O4 and Co-based spinel oxides bifunctional oxygen electrodes. Int. J. Electrochem. Sci, 2010.

[40] Martin Setvin, Cesare Franchini, Xianfeng Hao, Michael Schmid, Anderson Janotti, Merzuk Kaltak, Chris G Van de Walle, Georg Kresse, and Ulrike Diebold. Direct View at Excess Electrons in TiO2Rutile and Anatase. Phys. Rev. Lett., 113(8):086402–5, August 2014.

[41] Jordan E Katz, Xiaoyi Zhang, Klaus Attenkofer, Karena W Chapman, Cathrine Frandsen, Piotr Zarzycki, Kevin M Rosso, Roger W Falcone, Glenn A Waychunas, and Benjamin Gilbert. Electron Small Polarons and Their Mobility in Iron (Oxyhydr)oxide Nanoparticles. Science, 337(6099):1200–1203, 2012.

[42] Paul Erhart, Andreas Klein, Daniel Åberg, and Babak Sadigh. Efficacy of the DFT + U formalism for modeling hole polarons in perovskite oxides. Phys. Rev. B, 90(3):035204, July 2014.

[43] JM De Teresa, MR Ibarra, PA Algarabel, C Ritter, et al. Evidence for magnetic polarons in the magnetoresistive perovskites. Nature, 386(6622):256, 1997.

[44] Benjamin J Morgan and Graeme W Watson. A Density Functional Theory +U Study of Oxygen Vacancy Formation at the (110), (100), (101), and (001) Surfaces of Rutile TiO2. J. Phys. Chem. C, 113(17):7322–7328, April 2009.

[45] Nicole Adelstein, Jeffrey B Neaton, Mark Asta, and Lutgard C De Jonghe. Density functional theory based calculation of small-polaron mobility in hematite. Phys. Rev. B, 89(24):245115–9, June 2014.

[46] Chuying Ouyang, Yanlan Du, Siqi Shi, and Minsheng Lei. Small polaron migration in LixMn2O4: From first principles calculations. Phys. Lett. A, 373(31):2796–2799, July 2009.

[47] Stephan Lany. Semiconducting transition metal oxides. J. Phys. Condens. Matter, 27(28):283203, 2015.

[48] Shawn Chatman, Carolyn I Pearce, and Kevin M Rosso. Charge Transport at Ti-Doped Hematite (001)/Aqueous Interfaces. Chem. Mater., 27(5):1665–1673, March 2015.

[49] Graeme Henkelman, Blas P Uberuaga, and Hannes Jónsson. A climbing image nudged elastic band method for finding saddle points and minimum energy paths. J. Chem. Phys, 113(22):9901–5, 2000.

[50] O Bengone, M Alouani, P Blöchl, and J Hugel. Implementation of the projector augmented-wave LDA+U method: Application to the electronic structure of NiO. Phys. Rev. B, 62(24):16392–16401, 2000.

[51] Matteo Cococcioni and Stefano de Gironcoli. Linear response approach to the calculation of the effective interaction parameters in the LDA+U method. Phys. Rev. B, 71(3):035105, January 2005.

[52] Christoph Loschen, Javier Carrasco, Konstantin M Neyman, and Francesc Illas. First-principles LDA+U and GGA+U study of cerium oxides: Dependence on the effective U parameter. Phys. Rev. B, 75(3):035115–8, January 2007.

[53] Stefano Fabris, Stefano de Gironcoli, Stefano Baroni, Gianpaolo Vicario, and Gabriele Balducci. Taming multiple valency with density functionals: A case study of defective ceria. Phys. Rev. B, 71(4):041102–4, January 2005.

[54] W E Pickett, S C Erwin, and E C Ethridge. Reformulation of the LDA+U method for a local-orbital basis. Phys. Rev. B, 58(3):1201–1209, July 1998.

[55] A K McMahan, Richard M Martin, and S Satpathy. Calculated effective Hamiltonian for La2CuO4 and solution in the impurity Anderson approximation. Phys. Rev. B, 38(10):6650–6666, October 1988.

[56] Fei Zhou, Kisuk Kang, Thomas Maxisch, Gerbrand Ceder, and Dane Morgan. The electronic structure and band gap of LiFePO4 and LiMnPO4. Solid State Commun., 132(3-4):181–186, October 2004.

[57] Benjamin J Morgan and Graeme W Watson. Polaronic trapping of electrons and holes by native defects in anatase TiO2. Phys. Rev. B, 80(23):233102, 2009.

[58] Pierre Hohenberg and Walter Kohn. Inhomogeneous electron gas. Phys. Rev., 136(3B):B864, 1964.

[59] Walter Kohn and Lu Jeu Sham. Self-consistent equations including exchange and correlation effects. Phys. Rev., 140(4A):A1133, 1965.

[60] Robert G Parr. Density functional theory of atoms and molecules. In Horizons of Quantum Chemistry, pages 5–15. Springer, 1980.

[61] John P Perdew and Mel Levy. Physical content of the exact Kohn-Sham orbital energies: band gaps and derivative discontinuities. Phys. Rev. Lett., 51(20):1884, 1983.

[62] Ulf von Barth and Lars Hedin. A local exchange-correlation potential for the spin polarized case. i. J. Phys. C, 5(13):1629, 1972.

[63] David M Ceperley and BJ Alder. Ground state of the electron gas by a stochastic method. Phys. Rev. Lett., 45(7):566, 1980.

[64] Kieron Burke, John P Perdew, and Yue Wang. Derivation of a generalized gradient approximation: The PW91 density functional. In Electronic Density Functional Theory, pages 81–111. Springer, 1998.

[65] John P Perdew, Kieron Burke, and Matthias Ernzerhof. Generalized gradient approximation made simple. Phys. Rev. Lett., 77(18):3865, 1996.

[66] VI Anisimov and O Gunnarsson. Density-functional calculation of effective Coulomb interactions in metals. Phys. Rev. B, 43(10):7570–7574, April 1991.

[67] VI Anisimov, J Zaanen, and OK Andersen. Band theory and Mott insulators: Hubbard U instead of Stoner I. Phys. Rev. B, 44(3):943–954, July 1991.

[68] AI Liechtenstein, VI Anisimov, and J Zaanen. Density-functional theory and strong interactions: Orbital ordering in Mott-Hubbard insulators. Phys. Rev. B, 52(8):R5467–R5470, August 1995.

[69] S L Dudarev, G A Botton, S Y Savrasov, C J Humphreys, and A P Sutton. Electron-energy-loss spectra and the structural stability of nickel oxide: An LSDA+U study. Phys. Rev. B, 57(3):1505–1509, January 1998.

[70] A B Shick, A I Liechtenstein, and W E Pickett. Implementation of the LDA+U method using the full-potential linearized augmented plane-wave basis. Phys. Rev. B, 60(15):10763–10769, October 1999.

[71] B Amadon, F Jollet, and M Torrent. γ and β cerium: LDA+U calculations of ground-state parameters. Phys. Rev. B, 77(15):155104, apr 2008.

[72] Attila Szabo and Neil S. Ostlund. Modern Quantum Chemistry: Introduction to Advanced Electronic Structure Theory. Dover Publications, 1996.

[73] Aliaksandr V Krukau, Oleg A Vydrov, Artur F Izmaylov, and Gustavo E Scuseria. Influence of the exchange screening parameter on the performance of screened hybrid functionals. J. Chem. Phys., 125(22):224106–6, December 2006.

[74] John P Perdew, Matthias Ernzerhof, and Kieron Burke. Rationale for mixing exact exchange with density functional approximations. J. Chem. Phys., 105(22):9982–9985, 1996.

[75] Viktor Ivády, Rickard Armiento, Krisztián Szász, Erik Janzén, Adam Gali, and Igor A Abrikosov. Theoretical unification of hybrid-DFT and DFT+U methods for the treatment of localized orbitals. Phys. Rev. B, 90(3):035146–13, July 2014.

[76] I G Lang and Yu A Firsov. Calculation of the Activation Probability for a Jump of a Small-radius Polaron. Sov. Phys. - JETP, 27(3), 1968.

[77] Harald Böttger and Valerij V. Bryksin. Hopping conduction in solids. Berlin: Akademie-Verlag, 1985.

[78] Max Born and Vladimir Fock. Beweis des adiabatensatzes. Z. Phys. A, 51(3):165–180, 1928.

[79] Clarence Zener. Interaction between the *d*-Shells in the Transition Metals. II. Ferromagnetic Compounds of Manganese with Perovskite Structure. Phys. Rev., 82:403–405, May 1951.

[80] JH Van Vleck. Theory of the variations in paramagnetic anisotropy among different salts of the iron group. Phys. Rev., 41(2):208, 1932.

[81] Eva Pavarini, Erik Koch, Frithjof Anders, and Mark (Eds.) Jarrell. Correlated electrons: from models to materials, volume 2 of Schriften des Forschungszentrums Jülich. Reihe Modeling and simulation. 2012.

[82] Hermann Arthur Jahn and Edward Teller. Stability of polyatomic molecules in degenerate electronic states. I. Orbital degeneracy. In Proc. Royal Soc. A, volume 161, pages 220–235. The Royal Society, 1937.

[83] K. I. Kugel and D. I. Khomskii. The Jahn-Teller effect and magnetism: transition metal compounds. Phys. Usp, 25(4):231–256, 1982.

[84] B Meredig, A Thompson, H A Hansen, C Wolverton, and A van de Walle. Method for locating low-energy solutions within DFT+U. Phys. Rev. B, 82(19):195128–5, November 2010.

[85] Shuichi Nosé. A unified formulation of the constant temperature molecular dynamics methods. J. Chem. Phys, 81(1):511–519, 1984.

[86] GKH Madsen and P Novák. Charge order in magnetite. An LDA+U study. Europhys. Lett., 2005.

[87] Joachim Paier, Robin Hirschl, Martijn Marsman, and Georg Kresse. The Perdew–Burke–Ernzerhof exchange-correlation functional applied to the G2-1 test set using a plane-wave basis set. J. Chem. Phys., 122(23):234102, 2005.

[88] LA Charette, JB Adams, MJ Gaffey, TB McCord, et al. Cells with LiMn2O4 and V02 (B) as electrodes and 5 M LiNO3 in water as the electrolyte. J. Geophys. Res, 89:6899, 1984.

[89] Shyue Ping Ong, Vincent L Chevrier, and Gerbrand Ceder. Comparison of small polaron migration and phase separation in olivine LiMnPO4 and LiFePO4 using hybrid density functional theory. Phys. Rev. B, 83(7):075112, February 2011.

[90] Taizo Shibuya, Kenji Yasuoka, Susanne Mirbt, and Biplab Sanyal. A systematic study of polarons due to oxygen vacancy formation at the rutile TiO2(110) surface by GGA + U and HSE06 methods. J. Phys. Condens. Matter, 24(43):435504, October 2012.

[91] Zachary D Pozun and Graeme Henkelman. Hybrid density functional theory band structure engineering in hematite. J. Chem. Phys., 134(22):224706–10, 2011.

[92] G. Kresse and J. Hafner. Ab initio molecular dynamics for liquid metals. Phys. Rev. B, 47:558–561, Jan 1993.

[93] G. Kresse and J. Hafner. Ab initio molecular-dynamics simulation of the liquid-metal-amorphous-semiconductor transition in germanium. Phys. Rev. B, 49:14251–14269, May 1994.

[94] G. Kresse and J. Furthmüller. Efficiency of ab-initio total energy calculations for metals and semiconductors using a plane-wave basis set. Comput. Mater. Sci., 6(1):15–50, 1996.

[95] G. Kresse and J. Furthmüller. Efficient iterative schemes for ab initio total-energy calculations using a plane-wave basis set. Phys. Rev. B, 54:11169–11186, Oct 1996.

[96] John P. Perdew, Kieron Burke, and Matthias Ernzerhof. Generalized Gradient Approximation Made Simple. Phys. Rev. Lett., 77:3865–3868, Oct 1996.

[97] John P. Perdew, Kieron Burke, and Matthias Ernzerhof. Generalized Gradient Approximation Made Simple [Phys. Rev. Lett. 77, 3865 (1996)]. Phys. Rev. Lett., 78:1396–1396, Feb 1997.

[98] A Rohrbach, J Hafner, and G Kresse. Electronic correlation effects in transition-metal sulfides. J. Phys. Condens. Matter, 15(6):979–996, 2003.

[99] Kurt Lejaeghere et al. Reproducibility in density functional theory calculations of solids. Science, 351(6280):aad3000, 2016.

[100] Xavier Gonze et al. ABINIT: First-principles approach to material and nanosystem properties. Comput. Phys. Commun., 180(12):2582 – 2615, 2009.

[101] Marc Torrent, François Jollet, François Bottin, Gilles Zérah, and Xavier Gonze. Implementation of the projector augmented-wave method in the ABINIT code: Application to the study of iron under pressure. Comput. Mater. Sci, 42(2):337–351, 2008.

[102] D. C. Cronemeyer. Electrical and Optical Properties of Rutile Single Crystals. Phys. Rev., 87:876–886, Sep 1952.

[103] N Deskins and Michel Dupuis. Electron transport via polaron hopping in bulk TiO2: A density functional theory characterization. Phys. Rev. B, 75(19):195212, May 2007.

[104] S Mochizuki. Electrical conductivity of α-Fe2O3. Phys. Status Solidi (a), 41(2):591–594, June 1977.

[105] Brian Ellis, Laura K Perry, Dominic H Ryan, and LF Nazar. Small polaron hopping in LixFePO4 solid solutions: coupled lithium-ion and electron mobility. J. Am. Chem. Soc, 128(35):11416–11422, 2006.

[106] Aaron Mascaro, Zi Wang, Pierre Hovington, Yoichi Miyahara, Andrea Paolella, Vincent Gariepy, Zimin Feng, Tyler Enright, Connor Aiken, Karim Zaghib, et al. Measuring spatially resolved collective ionic transport on lithium battery cathodes using atomic force microscopy. Nano Lett., 17(7):4489–4496, 2017.

[107] Chuying Ouyang, Haidong Deng, Zhiqing Ye, Minsheng Lei, and Liquan Chen. Pulsed laser deposition prepared LiMn2O4 thin film. Thin Solid Films, 503(1-2):268–271, May 2006.

[108] K Kushida and K Kuriyama. Observation of the crystal-field splitting related to the Mn-3d bands in spinel-LiMn2O4 films by optical absorption. Appl. Phys. Lett., 77(25):4154–4156, December 2000.

[109] F. Bechstedt. Electronic Relaxation Effects in Core Level Spectra of Solids. Phys. Status Solidi B, 112(1):9–49, 1982.

[110] Richard M. Martin. Electronic Structure: Basic Theory and Practical Methods. Cambridge University Press, 2004.

[111] T Koopmans. Uber die Zuordnung von Wellenfunktionen und Eigenwerten zu den Einzelnen Elektronen Eines Atoms. Physica, 1(1-6):104–113, 1934.

[112] Chang-Guo Zhan, Jeffrey A. Nichols, and David A. Dixon. Ionization Potential, Electron Affinity, Electronegativity, Hardness, and Electron Excitation Energy - Molecular Properties from Density Functional Theory Orbital Energies. J. Phys. Chem. A, 107(20):4184–4195, 2003.

[113] J Zhu, XW Wang, and SG Louie. First-principles pseudopotential calculations of magnetic iron. Phys. Rev. B, 45(16):8887–8893, April 1992.

[114] Carlos L Reis, J M Pacheco, and José Luís Martins. First-principles norm-conserving pseudopotential with explicit incorporation of semicore states. Phys. Rev. B, 68(15):155111–6, October 2003.

[115] S G Louie, S Froyen, and M L Cohen. Nonlinear ionic pseudopotentials in spin-density-functional calculations. Phys. Rev. B, 26(4):1738–1742, 1982.

[116] Yang Sun, Xia Lu, Ruijuan Xiao, Hong Li, and Xuejie Huang. Kinetically Controlled Lithium-Staging in Delithiated LiFePO 4Driven by the Fe Center Mediated Interlayer Li–Li Interactions. Chem. Mater., 24(24):4693–4703, December 2012.

[117] John C Tully, George H Gilmer, and Mary Shugard. Molecular dynamics of surface diffusion. I. The motion of adatoms and clusters. J. Chem. Phys, 71(4):1630, 1979.

[118] Keh-Dong Shiang. Molecular dynamics simulation of adatom diffusion on metal surfaces. J. Chem. Phys, 99(12):9994, 1993.

[119] M Saiful Islam, Daniel J Driscoll, Craig A J Fisher, and Peter R Slater. Atomic-Scale Investigation of Defects, Dopants, and Lithium Transport in the LiFePO 4Olivine-Type Battery Material. Chem. Mater., 17(20):5085–5092, October 2005.

[120] Jianjun Yang and John S Tse. Li Ion Diffusion Mechanisms in LiFePO 4: An ab Initio Molecular Dynamics Study. J. Phys. Chem. A, 115(45):13045–13049, November 2011.

[121] P. Blaha, K. Schwarz, G. K. H. Madsen, D. Kvaniscka, and J. Luitz. WIEN2k, An Augmented Plane Wave Plus Local Orbitals Program for Calculating Crystal Properties. Technische Universität Wien, 2014.

[122] Grazyna Antczak and Gert Ehrlich. Surface diffusion: metals, metal atoms, and clusters. Cambridge University Press, 2010.

[123] P-G De Gennes. Effects of double exchange in magnetic crystals. Phys. Rev., 118(1):141, 1960.

[124] John B. Goodenough. Direct Cation- -Cation Interactions in Several Oxides. Phys. Rev., 117:1442–1451, Mar 1960.

[125] M. A. Ruderman and C. Kittel. Indirect Exchange Coupling of Nuclear Magnetic Moments by Conduction Electrons. Phys. Rev., 96:99–102, Oct 1954.

[126] John B. Goodenough. An interpretation of the magnetic properties of the perovskite-type mixed crystals La1-xSrxCoO3-λ. J. Phys. Chem. Solids, 6(2):287 – 297, 1958.

[127] Junjiro Kanamori. Superexchange interaction and symmetry properties of electron orbitals. J. Phys. Chem. Solids, 10(2):87 – 98, 1959.

[128] KI Kugel and DI Khomskii. Crystal-structure and magnetic properties of substances with orbital degeneracy. Zh. Eksp. Teor. Fiz, 64:1429–1439, 1973.

[129] Walter A Harrison. Electronic structure and the properties of solids: the physics of the chemical bond. Courier Corporation, 2012.

[130] Yang Hou, Fan Zuo, Alex Dagg, and Pingyun Feng. A Three-Dimensional Branched Cobalt-Doped α-Fe2O3 Nanorod/MgFe2O4 Heterojunction Array as a Flexible Photoanode for Efficient Photoelectrochemical Water Oxidation. Angewandte Chemie, 125(4):1286–1290, 2013.

[131] James C Knight, Soosairaj Therese, and Arumugam Manthiram. On the Utility of Spinel Oxide Hosts for Magnesium-Ion Batteries. ACS Appl. Mater. Interfaces, 7(41):22953–22961, October 2015.

[132] AS Bhalla, Ruyan Guo, and Rustum Roy. The perovskite structure-a review of its role in ceramic science and technology. Mater. Res. Innov., 4(1):3–26, 2000.

[133] Wan-Jian Yin, Ji-Hui Yang, Joongoo Kang, Yanfa Yan, and Su-Huai Wei. Halide perovskite materials for solar cells: a theoretical review. J. Mater. Chem. A, 3(17):8926–8942, 2015.

[134] San Ping Jiang. Development of lanthanum strontium manganite perovskite cathode materials of solid oxide fuel cells: a review. J. Mater. Sci., 43(21):6799–6833, 2008.

[135] A. J. Millis, P. B. Littlewood, and B. I. Shraiman. Double Exchange Alone Does Not Explain the Resistivity of $La_{1-x}Sr_xMnO_3$. Phys. Rev. Lett., 74:5144–5147, Jun 1995.

[136] A. J. Millis, R. Mueller, and Boris I. Shraiman. Fermi-liquid-to-polaron crossover. II. Double exchange and the physics of colossal magnetoresistance. Phys. Rev. B, 54:5405–5417, Aug 1996.

[137] J S Zhou and J B Goodenough. Phonon-Assisted Double Exchange in Perovskite Manganites. Phys. Rev. Lett., 80(12):2665–2668, March 1998.

[138] John C Slater and George F Koster. Simplified LCAO method for the periodic potential problem. Phys. Rev., 94(6):1498, 1954.

[139] N Binggeli and M Altarelli. Orbital ordering, Jahn-Teller distortion, and resonant x-ray scattering in KCuF3. Phys. Rev. B, 70(8):725–10, August 2004.

[140] BA Hamad. First-principle calculations of structural and electronic properties of rutile-phase dioxides (MO 2), M= Ti, V, Ru, Ir and Sn. Eur. Phys. J. B, 70(2):163–169, 2009.

[141] V Eyert. The metal-insulator transitions of VO2: A band theoretical approach. Annalen der Physik, 11(9):650–704, 2002.

[142] Shouheng Sun and Hao Zeng. Size-controlled synthesis of magnetite nanoparticles. J. Am. Chem. Soc, 124(28):8204–8205, 2002.

[143] Aron Walsh, Su-Huai Wei, Yanfa Yan, M M Al-Jassim, John A Turner, Michael Woodhouse, and B A Parkinson. Structural, magnetic, and electronic properties of the Co-Fe-Al oxide spinel system: Density-functional theory calculations. Phys. Rev. B, 76(16):165119–9, October 2007.

[144] Chen Ling and Fuminori Mizuno. Phase Stability of Post-spinel Compound AMn2O4 (A = Li, Na, or Mg) and Its Application as a Rechargeable Battery Cathode. Chem. Mater., 25(15):3062–3071, August 2013.

[145] J E Greedan, N P Raju, A S Wills, C Morin, S M Shaw, and J N Reimers. Structure and Magnetism in λ-MnO 2. Geometric Frustration in a Defect Spinel. Chem. Mater., 10(10):3058–3067, October 1998.

[146] Paolo G Radaelli. Orbital ordering in transition-metal spinels. New J. Phys., 7(1):53, 2005.

[147] Jaekwang Lee, Stephen J Pennycook, and Sokrates T Pantelides. Simultaneous enhancement of electronic and Li+ ion conductivity in LiFePO4. Appl. Phys. Lett., 101(3):033901–5, 2012.

[148] T Goto, T Kimura, G Lawes, AP Ramirez, and Y Tokura. Ferroelectricity and giant magnetocapacitance in perovskite rare-earth manganites. Phys. Rev. Lett., 92(25):257201, 2004.

[149] Victor Moritz Goldschmidt. Die gesetze der krystallochemie. Naturwissenschaften, 14(21):477–485, 1926.

[150] Patrick M Woodward. Octahedral tilting in perovskites. I. Geometrical considerations. Acta Crystallogr. B, 53(1):32–43, 1997.

[151] Eva Pavarini and Erik Koch. Origin of Jahn-Teller distortion and orbital order in LaMnO3. Phys. Rev. Lett., 104(8):086402, 2010.

[152] Jiangang He and Cesare Franchini. Screened hybrid functional applied to $3d^0 \rightarrow 3d^8$ transition-metal perovskites LaMO$_3$ (M = Sc–Cu): Influence of the

exchange mixing parameter on the structural, electronic, and magnetic properties. Phys. Rev. B, 86:235117, Dec 2012.

[153] Cesare Franchini. Hybrid functionals applied to perovskites. J. Phys. Condens. Matter, 26(25):253202, June 2014.

[154] A Urushibara, Y Moritomo, T Arima, A Asamitsu, Gt Kido, and Y Tokura. Insulator-metal transition and giant magnetoresistance in La 1-x Sr x MnO 3. Phys. Rev. B, 51(20):14103, 1995.

[155] R. Kilian and G. Khaliullin. Orbital polarons in the metal-insulator transition of manganites. Phys. Rev. B, 60:13458–13469, Nov 1999.

[156] Giniyat Khaliullin and Satoshi Okamoto. Theory of orbital state and spin interactions in ferromagnetic titanates. Phys. Rev. B, 68:205109, Nov 2003.

[157] Pablo Garcia-Fernandez, Jose Antonio Aramburu, and Miguel Moreno. Influence of magnetic ordering on structural instabilities in insulating perovskites. Phys. Rev. B, 83:174406, May 2011.

[158] T. Mizokawa, D. I. Khomskii, and G. A. Sawatzky. Orbital polarons and ferromagnetic insulators in manganites. Phys. Rev. B, 63:024403, Dec 2000.

[159] E Pavarini, E Koch, and A I Lichtenstein. Mechanism for Orbital Ordering in KCuF3. Phys. Rev. Lett., 101(26):1429–4, December 2008.

[160] Ibério de Pinho Ribeiro Moreira and Francesc Illas. Ab initio study of magnetic interactions in KCuF3 and K2CuF4 low-dimensional systems. Phys. Rev. B, 60:5179–5185, Aug 1999.

[161] R. Caciuffo, L. Paolasini, A. Sollier, P. Ghigna, E. Pavarini, J. van den Brink, and M. Altarelli. Resonant x-ray scattering study of magnetic and orbital order in $KCuF_3$. Phys. Rev. B, 65:174425, May 2002.

[162] J M Ricart, R Dovesi, C Roetti, and V R Saunders. Electronic and magnetic structure of KNiF3 perovskite. Phys. Rev. B, 52(4):2381–2389, July 1995.

[163] Richard L Martin and Francesc Illas. Antiferromagnetic Exchange Interactions from Hybrid Density Functional Theory. Phys. Rev. Lett., 79(8):1539–1542, August 1997.

[164] Miguel Marques. Time-dependent density functional theory, volume 706. Springer Science & Business Media, 2006.

[165] François Jollet, Marc Torrent, and Natalie Holzwarth. Generation of Projector Augmented-Wave atomic data: A 71 element validated table in the XML format. Comput. Phys. Commun., 185(4):1246–1254, April 2014.

[166] N.A.W. Holzwarth et al. Periodic Table of the Elements for PAW Functions (<2013).

[167] N.A.W. Holzwarth, A.R. Tackett, and G.E. Matthews. A Projector Augmented Wave (PAW) code for electronic structure calculations, Part I: atompaw for generating atom-centered functions. Comput. Phys. Commun., 135(3):329–347, April 2001.